Activated Carbon Fiber Filter Media For Proton Exchange Membrane Fuel Cell

by

Wei Liu

A dissertation submitted to the Graduate Faculty of
Auburn University
in partial fulfillment of the
requirements for the Degree of
Doctor of Philosophy

Auburn, Alabama
May 14, 2010

Keywords: Proton exchange membrane fuel cell, activated carbon fibers, sulfur dioxide removal

Approved by

Sabit Adanur, Chair, Professor of Polymer and Fiber Engineering
Bruce Tatarchuk, Professor of Chemical Engineering
Peter Schwartz, Professor of Polymer and Fiber Engineering
Ann B. Presley, Associate Professor of Consumer Affairs

Abstract

Sulfur dioxide, a major air pollutant, has been found to be poisonous to proton exchange membrane fuel cells and causes degradation of fuel cell systems. Currently used industrial desulfurization systems, such as wet scrubbing, cannot address this problem because they cannot completely clean sulfur dioxide and SO_2 with the concentration lower than 30 ppmv escapes. A fuel cell is more sensitive to poisoning than human's lung and even a trace of sulfur dioxide will cause the irreversible degradation of a fuel cell. Activated carbon fibers (ACFs), one of relatively new adsorbents, are considered to remove sulfur dioxide from air before it is fed into fuel cell systems since ACFs have advantages in adsorption rate in comparison with granular activated carbon due to easy access of adsorbate to adsorption sites in micropores in activated carbon fibers.

Activated carbon nanofibers were manufactured in the lab by electrospinning of polyacrylonitrile followed by chemical activation with potassium hydroxide. Micropores were shown to be dominant in the electrospun activated carbon nanofibers. However, their fragility and high manufacturing cost limit their applications in filtration.

Pore structures and capabilities of removing sulfur dioxide of novoloid-based and rayon-based activated carbon fibers were analyzed. Surface areas were found to have correlation with pore volume in fibers. The sulfur dioxide capacities of ACFs were found to be proportional to the percentage of micropores in fibers.

To improve sulfur dioxide removal efficiency of activated carbon fibers, alkali, metal and oxidants were applied onto ACFs as promoters. KOH (potassium hydroxide), K_2CO_3 (potassium carbonate), $KClO_3$ (potassium chlorate) and $KMnO_4$ (potassium permanganate) increased the desulfurization efficiency of ACFs greatly. Only $KMnO_4$ modified ACFs are suitable for the wet laying technique with which ACF paper was made for filter device in the current study since the other three promoters can be removed easily by exposure to water. The optimum potassium permanganate weight ratio in ACF15 was found to be in the range of 43~45 wt% which exhibited the maximum sulfur dioxide capacity. The effect of carrier gas on desulfurization was studied which showed that the co-presence of water and oxygen would be preferred. The advantage of $KMnO_4$ modified ACF15 is that the modification process does not need high temperature calcination in inert gas and thus is energy saving.

Activated carbon fiber paper (K-ACFP) was manufactured from $KMnO_4$ modified ACF15 and the binder fiber, copolyester (CoPET). The strongest K-ACFP was obtained when the ratio of $KMnO_4$/ACF15 to CoPET is 7:3. Sulfur dioxide breakthrough capacity of the resulting K-ACFP was found to be similar to $KMnO_4$/ACF15 fiber before the wet laying process. Produced K-ACFP can be used as the filter media for fuel cell protection from sulfur dioxide.

The desulfurization mechanisms of $KMnO_4$ modified ACFs with different carrier gases were studied. Considering the diffusion of adsorbate within packed bed and single activated carbon fiber and reaction over fiber surfaces, models were developed for different compositions of the challenge gas to predict breakthrough characteristics of $KMnO_4$/ACFs. The predicted curves agree with the experimental results reasonably well.

The dependency of sulfur dioxide removal efficiency of $KMnO_4$/ACFs on the location in the packed bed and the elapsed time are predicted with the developed models as well.

Acknowledgments

The author would like to express her special thanks to her advisor Dr. Sabit Adanur for his commitment to this project, technical advice and support through the duration of this study. It would have been impossible for me complete this work without his support. I also appreciate his support not only in academic work but also in my life. He is more than an advisor and like a friend in life.

The author wishes to thank Dr. Bruce Tatarchuk, Dr. Peter Schwartz and Dr. Ann B. Presley for serving on her committee. Special thanks are extended to Dr. Tatarchuk for his financial support and making his top quality labs and research group available for my studies, which is appreciated.

The author wishes to thank Dr. Roy Broughton for valuable suggestions and help for my research and thank the Department of Polymer and Fiber Engineering for providing support and a friendly environment.

Special acknowledgement and heartfelt gratitude must be given to my parents, husband and parents-in-law and friends whose love and vision for me continues to motivate, inspire and guide me.

Table of Contents

Abstract ii

Acknowledgments v

List of Tables x

List of Figures xii

List of Abbreviations xvii

Chapter 1 Introduction and Literature Review 1

1.1 Introduction to fuel cells 2

1.2 Working mechanism of proton exchange membrane fuel cell (PEMFC) 3

1.3 Poisoning sources and their effect on PEMFC 6

1.4 Effects of contaminants on PEMFC performance 8

1.4.1 Contaminants on proton exchange membranes 9

1.4.2 Contaminants for anode 9

1.4.3 Contaminants on cathode 10

1.5 Need of PEMFC cathode filter 16

1.6 Industry method for sulfur dioxide purification 16

1.7 Porous adsorbents in sulfur dioxide removal 17

1.8 Advantages of ACFs in comparison with GAC and PAC 18

1.9 Manufacturing of activated carbon fibers 22

1.10 Sulfur dioxide adsorption over activated carbon fibers 24

1.10.1 Sulfur dioxide removal on bare activated carbon fibers.....24
1.10.2 Treatment for promotion of sulfur dioxide removal.....25
1.11 Objectives of the research 29
References 30
Chapter 2 Manufacturing of Activated Carbon Fibers via Electrospinning 38
2.1 Introduction 38
2.2 Materials and experimental procedures.....40
2.3 Results and discussion.....41
2.3.1 Influence of electrospinning parameters on fiber diameters 41
2.3.2 Physical and mechanical properties of electrospun PAN membranes47
2.3.3 Properties of electrospun PAN based activated carbon nanofibers ...52
2.4 Conclusions 56
References 57
Chapter 3 Sulfur Dioxide Removal Over Activated Carbon Fibers and Modified
Activated Carbon Fibers.....60
3.1 Experimental 60
3.1.1 Materials.....60
3.1.2 Pore structures and element analysis.....62
3.1.3 Sulfur dioxide adsorption testing 63
3.1.4 Modification of activated carbon fibers 65
3.1.5 ACFs surface morphology analysis.....67
3.1.6 Thermogravimetric analysis (TGA) 67
3.1.7 X-Ray diffraction analysis.....67

3.1.8 Manufacturing of activated carbon fiber paper 67

3.2 Results and discussions 71

3.2.1 Pore structures and surface morphology of ACFs.....71

3.2.2 Element analysis.....76

3.2.3 Sulfur dioxide adsorption properties of activated carbon fibers and modified activated carbon fibers 76

3.3 SEM imaging analysis 96

3.4 Activated carbon fiber papers (ACFP) and their SO_2 adsorption capacities99

3.5 XRD analysis on $KMnO_4$/ACF15 105

3.6 Energy dispersive X-ray analysis 108

References 111

Chapter 4 Mechanism Analysis of Sulfur Dioxide Removal by ACFs and Model Development 113

4.1 Introduction 113

4.2 Mechanism one.....116

4.2.1 Mechanism study 116

4.2.2 Model development 121

4.2.3 Prediction of breakthrough curve with the developed model 132

4.3 Mechanism two 134

4.4 Mechanism three 139

4.4.1 Mechanism analysis 139

4.4.2 Model development 144

4.5 Mechanism four.....148

4.6 Model system 153

References 155

Chapter 5 Conclusions and Recommendations.....158

5.1 Conclusions 158

5.2 Recommendations 160

References 161

Appendix 1 Matlab® code for Yoon's model 162

Appendix 2 Matlab® code for prediction of breakthrough curves for mechanism one and two 163

Appendix 3 Matlab® code for prediction of breakthrough curves for mechanism three and four.....167

List of Tables

Table 1.1 Types of fuel cells and their major features 3

Table 1.2 Contaminants in the operation of PEM fuel cells 6

Table 1.3 National ambient air quality standards 8

Table 1.4 Contaminants and their concentrations in battlefield 8

Table 2.1 Physical properties of electrospun PAN membrane and stabilized PAN membrane 51

Table 2.2 Pore structures of electrospun PAN and activated carbon nanofibers.....55

Table 3.1 Compositions of activated carbon fiber papers.....70

Table 3.2 BET surface area, pore volume and pore size of ACFs and PAC 72

Table 3.3 Pore volume distribution of ACFs and PAC 74

Table 3.4 Number of adsorption sites of activated carbon fibers and PAC.....75

Table 3.5 Element components of activated carbon fibers 76

Table 3.6 Sulfur dioxide capacities of bare activated carbon fibers in the absence of water 79

Table 3.7 Sulfur dioxide capacities of bare activated carbon fibers with water present ..81

Table 3.8 Sulfur dioxide capacities of bare activated carbon fibers with initial SO_2 concentration of 50ppm and with humidified air as the carrier gas 83

Table 3.9 Sulfur dioxide capacities of metal/ACF20.....89

Table 3.10 Element contents of $KMnO_4$/ACF15 before and after adsorption of SO_2 in humidified air 109

Table 4.1 90% saturation capacities 119

Table 4.2 4% breakthrough capacities 144

Table 4.3 Parameters in the model system for mechanisms 1~4.....154

List of Figures

Figure 1.1 Schematic of a proton exchange membrane fuel cell structure 4

Figure 1.2 Polarization curves with different NO_x concentrations 12

Figure 1.3 Periodic test of the reversibility of cell performances 12

Figure 1.4 Cell current after exposure to 2.5 and 5 ppm SO_2 in air 14

Figure 1.5 Cyclic voltammetry spectra after cathode exposure to 2.5ppm SO_2 in air 15

Figure 1.6 Durability of PEMFC with exposure to 5ppm SO_2 in air.....15

Figure 1.7 Schematic of pore structures of a) ACF and b) GAC 21

Figure 1.8 Pore size distribution of ACF and GAC 21

Figure 2.1 SEM images of electrospun PAN from different concentrations 43

Figure 2.2 Fiber diameters with different PAN concentrations.....43

Figure 2.3 The frequency distribution of nanofiber diameters for different solution concentrations 44

Figure 2.4 Fiber diameters at different voltages.....45

Figure 2.5 Fiber diameters at different flow rates 46

Figure 2.6 Fiber diameters at different need-tip distances.....47

Figure 2.7 Variation of tensile strength with the change of electrospun PAN membrane thickness.....47

Figure 2.8 Variation of tear strength with the change of membrane thickness 49

Figure 2.9 Variation of burst strength with the change of membrane thickness 49

Figure 2.10 Air permeability as a function of membrane thickness.....50

Figure 2.11 Tensile strength variation of stabilized electrospun PAN with the increase in thickness 52

Figure 2.12 SEM images of (a) electrospun PAN membrane and (b) activated carbon nanofibers 53

Figure 2.13 FTIR spectrum for (a) electrospun PAN, (b) stabilized PAN, and (c) activated carbon nanofibers 54

Figure 2.14 DA pore size distribution.....56

Figure 2.15 Generalized Halsey V-t plot 56

Figure 3.1 Structure of Kynol^{TM} novoloid fibers.....61

Figure 3.2 Structure of carbonized novoloid fiber with 95% carbon 61

Figure 3.3 Schematic and picture of SO_2 adsorption test bench.....63

Figure 3.4 Correlation between surface area and pore volume 73

Figure 3.5 Pore size distributions of ACFs and ACP 74

Figure 3.6 Surface morphology of ACFs 1) ×9500, 2) ×250,000 75

Figure 3.7 Effect of surface area of ACFs on sulfur dioxide breakthrough capacity 79

Figure 3.8 Breakthrough profiles of ACFs with absence of water in gas stream 80

Figure 3.9 Breakthrough profiles of ACFs with the presence of water in the carrier gas 82

Figure 3.10 Mechanism of sulfur dioxide removal over activated carbon surface with the presence of oxygen and water 82

Figure 3.11 Breakthrough profiles of ACFs in SO_2/humidified air 84

Figure 3.12 Breakthrough curves of KOH/ACF20 exposed to 20ppm SO_2 carried by dry air.....86

Figure 3.13 SO_2 adsorption capacities and utilization of KOH/ACF20 and K_2CO_3/ACF20 87

Figure 3.14 SO_2 adsorption capacities of $KClO_3$/ACF15 before and after exposure to water 90

Figure 3.15 SO_2 breakthrough capacity of $KMnO_4$ loaded ACF10, ACF15, ACF20 and PAC 92

Figure 3.16 SO_2 breakthrough capacity of ACF15 loaded with different ratios of $KMnO_4$ 93

Figure 3.17 Breakthrough profiles of $KMnO_4$/ACF15 before and after exposure to water 93

Figure 3.18 Breakthrough profiles of $KMnO_4$/ACF15 after exposure to water under different adsorption conditions.....94

Figure 3.19 Breakthrough profiles of $KMnO_4$/ACF15 prepared from 2wt% $KMnO_4$ solutions.....95

Figure 3.20 Sulfur dioxide adsorption properties of humidified KMnO4/ACF15 in comparison with dried samples 96

Figure 3.21 Surface morphology of $KMnO_4$/ACF15: 1) 6.55wt% $KMnO_4$ 2) 23.16wt% $KMnO_4$, 3) 43.34wt% $KMnO_4$ and 4) 43.34wt% $KMnO_4$ after exposure to water 97

Figure 3.22 $KMnO_4$/ACF15 surface morphology after exposure to 1) SO_2+N_2, 2) SO_2+air, 3) SO_2+H_2O and 4) SO_2+air+H_2O 98

Figure 3.23 Thickness, tensile strength and coefficient of thickness variation (CV) of ACFP samples corresponding to Table 3.1 99

Figure 3.24 DSC analysis of CoPET 101

Figure 3.25 SEM images of ACFP composed of 70wt% ACF20 and 30wt% CoPET with a fusing temperature of 200°C for 20min (×500) 102

Figure 3.26 SEM images of K-ACFP: (1) before and (2) after sulfur dioxide adsorption tests (×2000) 104

Figure 3.27 Breakthrough profiles of ACFP in comparison with $KMnO_4$/ACF15 with 50 ppm SO_2 challenge gas carried by humidified air 105

Figure 3.28 XRD patterns of ACF15, $KMnO_4$/ACF15 and spent $KMnO_4$/ACF15 after exposure to sulfur dioxide carried by humidified air 106

Figure 3.29 XRD patterns of $KMnO_4$/ACF15 before and after adsorption of sulfur dioxide carried by humidified nitrogen 107

Figure 3.30 XRD patterns of $KMnO_4$/ACF15 before and after adsorption of sulfur dioxide carried by dry air 108

Figure 3.31 EDS element signals (1) before and (2) after adsorption in the challenge gas of SO_2+H_2O+air 110

Figure 4.1 Prediction of breakthrough curve of ACF20 according to Yoon's model 115

Figure 4.2 Prediction of breakthrough curve of $KMnO_4$/ACF15 according to Yoon's model.....115

Figure 4.3 TGA curves of $KMnO_4$/ACF15 before and after adsorption tests in 50ppm SO_2 carried by nitrogen 117

Figure 4.4 Breakthrough curves of ACF15, $KMnO_4$/ACF15 before exposed to water, $KMnO_4$/ACF15 and $KMnO_4$ in the challenge gas of SO_2+N_2 118

Figure 4.5 Breakthrough curve of $KMnO_4$/ACF15 exposed to 50ppm sulfur dioxide carried by nitrogen 133

Figure 4.6 Prediction of sulfur dioxide removal efficiency with the variation of location and time 133

Figure 4.7 Breakthrough profiles of $KMnO_4$/ACF15 with exposure to sulfur dioxide challenge gas carried by air and nitrogen 135

Figure 4.8 Weight change of $KMnO_4$/ACF15 before and after adsorption tests in the challenge gas of SO_2 carried by air with increasing temperatures 136

Figure 4.9 Prediction of breakthrough curve of $KMnO_4$/ACF15 with challenge gas of SO_2+air.....138

Figure 4.10 Prediction of sulfur dioxide removal efficiency at different locations and times with the challenge gas of SO_2+air 139

Figure 4.11 Weight changes of ACF15, $KMnO_4$/ACF15 before and after SO_2 adsorption test with the presence of water in the carrier gas with increasing temperatures 141

Figure 4.12 Effect of temperature on weight of ACF15 and $KMnO_4$/ACF15.....141

Figure 4.13 Breakthrough profiles of $KMnO_4$ with different challenge gases.....143

Figure 4.14 Breakthrough profiles of $KMnO_4$/ACF15 in comparison with $KMnO_4$ in the gas stream of sulfur dioxide and humidified nitrogen 143

Figure 4.15 Prediction of breakthrough profile of $KMnO_4$/ACF15 in humidified nitrogen 147

Figure 4.16 Dependence of sulfur dioxide removal efficiency on time and location in the packed bed with the carrier gas of humidified nitrogen 148

Figure 4.17 Breakthrough profile of $KMnO_4$/ACF15 with exposure to sulfur dioxide carried by humidified nitrogen and air 149

Figure 4.18 TGA curves of $KMnO_4$/ACF15before and after exposure to challenge gas of SO_2+H_2O+air and SO_2+H_2O+N_2.....151

Figure 4.19 Prediction of breakthrough profile of $KMnO_4$/ACF15 exposed to SO_2 +H_2O+air 152

Figure 4.20 SO_2 removal efficiency of $KMnO_4$/ACF15 at various times and locations with the challenge gas of SO_2 +H_2O+air 153

Figure 4.21 Prediction of breakthrough curve following Mechanism One with the power law model system 154

Figure 4.22 Prediction of breakthrough curve following Mechanism Two with the power law model system 155

List of Abbreviations

C	Sulfur dioxide concentration in the main gas stream (mol/m^3)
C_r	Gas phase sulfur dioxide concentration within the fiber (mol/m^3)
C_s^F	Solid phase sulfur dioxide concentration on fiber surface (mol/m^3)
C_s	Average sulfur dioxide concentration within fibers including gas phase and solid phase which is adsorbed on fiber surfaces (mol/m^3)
C_{rs}	Solid phase sulfur dioxide concentration adsorbed on fiber surface (mol/m^3)
$\overline{C}_r$	Average gas phase sulfur dioxide concentration within a fiber (mol/m^3)
$\overline{C}_{rs}$	Average of the solid phase adsorbed sulfur dioxide concentration on the fiber surface (mol/m^3)
D	Diffusivity (m^2/s)
D_e	Effective diffusivity (m^2/s)
d_f	Fiber diameter (m)
d_{re}	Diameter of the reactor
D_k	Knudsen diffusivity (m^2/s)
D_m	Molecular diffusivity (m2/s)
D_z	Axial diffusivity (m^2/s)
F	Gas phase sulfur dioxide concentration within the fiber used in the modeling code (mol/m^3)

FR Volumetric flow rate of gas stream (mL/min)

$$f = \frac{\varepsilon}{1-\varepsilon}$$

h Step size in z direction of the model

L Length of the packed ACFs bed (m)

k Step size of time direction in the model

k_B Boltzmann's constant.

k_g Mass transfer coefficient

M Number of segments of the packed bed for the model

M_g Molecular weight of gas (g/mol)

m Index of time direction in the model

N Number of the segments of time for the model

n Index of z direction in the model

r Radius of an infinitesimal unit from the central line of a fiber

R Ideal gas constant (8.3 $m^3 \cdot Pa/K \cdot mol$)

R_e Reynolds number

r_f Fiber radius (m)

r_p Pore radius (m)

S_c Schmidt number

t Time (s)

T Temperature (K)

u Face velocity of the main gas stream (m/s)

V_{carbon} Volume occupied by the solid carbon in an activated carbon fiber (mL)

$V_{modifier}$ Volume of the modification agents (such as potassium hydroxide and potassium permanganate)

V_{tpore} Total pore volume within the fiber (mL)

z Distance from the beginning of the packed ACFs bed (m)

r_f Fiber radius (m)

α Intrafiber void fraction or the intrafiber porosity

β Modifier load with respect to the total sample weight

ε Porosity of the packed ACFs bed

τ Tortuosity factor of pores in porous fibers

λ Mean free path

ρ_{carbon} Solid density of ACF (cm^3/g)

$\rho_{modifier}$ Density of the modification agent (cm^3/g)

ρ_g Density of fluid (cm^3/g)

μ Viscosity of the gas stream (cP·s)

σ_{AB} Collision diameter (angstrom)

ε_{AB} Maximum attractive energy between two molecules

ω_{AB} Collision integral, a function of k_BT/ε_{AB}

Chapter 1 Introduction and Literature Review

1.1 Introduction to fuel cells

Fuel cells are electrochemical devices that convert chemical energy into electrical energy directly [1]. They are considered to be a viable alternative to the internal combustion engines, since they have a higher efficiency. Combined with H_2, as the fuel, they enable CO_2 emission free power conversion [2].

Because the intermediate steps of producing heat and mechanical work of most conventional power generation methods are avoided, fuel cells are not limited by thermodynamic limitations of heat engines such as the Carnot efficiency. In addition, fuel cells produce power with minimal pollutant since combustion is avoided. However, unlike batteries the reductant and oxidant in fuel cells must be continuously replenished to allow continuous operation.

Fuel cell systems are assembled with fuel preparation, air supply, thermal management, water management and electric power conditioning equipment. Fuel cells can be classified by the type of electrolyte used in the cell as listed in Table 1.1[3]. The various fuel cell types offer the strengths in different ways. The proton exchange membrane fuel cell (PEMFC) capitalizes on the essential simplicity of the fuel cell. The electrolyte is solid polymer in which protons are mobile. The chemistry is the same as the acid electrolyte fuel cell. With a solid and immobile electrolyte, this type of fuel cell is

inherently very simple. These cells run at quite low temperatures, so the problem of slow reaction rates is addressed by sophisticated catalysts and electrodes. Platinum is the catalyst and the development in recent years allow a small amount to reduce the cost. However, the storage of hydrogen is not really addressed. Considering the difficulty in storing hydrogen fuel, methanol is used in direct methanol fuel cells. Even though these fuel cells have very low powers, they have many potential applications in the rapidly growing portable electronic equipment. Alkaline fuel cells have advantages in less activation overvoltage, higher operating voltages (as high as 0.875bV) and low costs whereas the main problem is that air and fuel supplies must be free of CO_2 and hydrogen must be used. The phosphoric acid fuel cell (PAFC) was first commercialized and enjoys widespread terrestrial use because of reliability and easy or free maintenance. The solid oxide fuel cell (SOFC) operates in the region of 600°C to 1000°C allowing a high reaction rate without expensive catalysts but the ceramic materials used to make SOFC are difficult to handle and manufacture and extra pre-heating and cooling equipment is required. Molten carbonate fuel cell needs carbon dioxide in air to work and the high reaction rate is achieved by high temperature and the relatively low cost catalyst, nickel.

Table 1.1 Types of fuel cells and their major features [3]

Fuel cell type	Mobile ion	Operating temperature	Applications and notes
Alkaline (AFC)	OH^-	50~200°C	Used in space vehicles, e.g. Apollo, Shuttle
Proton exchange membrane (PEMFC)	H^+	30~100°C	Vehicles and mobile applications
Direct methanol (DMFC)	H^+	20~90°C	Suitable for portable electronic systems of low power, running for long times
Phosphoric acid (PAFC)	H+	~200°C	Large number of 200 kW CHP systems
Molten carbonate (MCFC)	CO_3^{2-}	~650°C	Suitable for medium to large scale CHP systems, up to MW capacity
Solid oxide (SOFC)	O^{2-}	500~1000°C	Suitable for all sizes of CHP systems, 2 kW to multi-MW

*CHP refers to combined heat and power

1.2 Working mechanism of proton exchange membrane fuel cell (PEMFC)

The basic structure of a fuel cell consists of an electrolyte layer in contact with an anode and a cathode as shown in Figure 1.1. Fuel is fed continuously to the anode and an oxidant is fed to the cathode. The electrochemical reactions take place at the electrodes to produce an electric current through electrolytes, while driving a complementary electric current that performs work on the load.

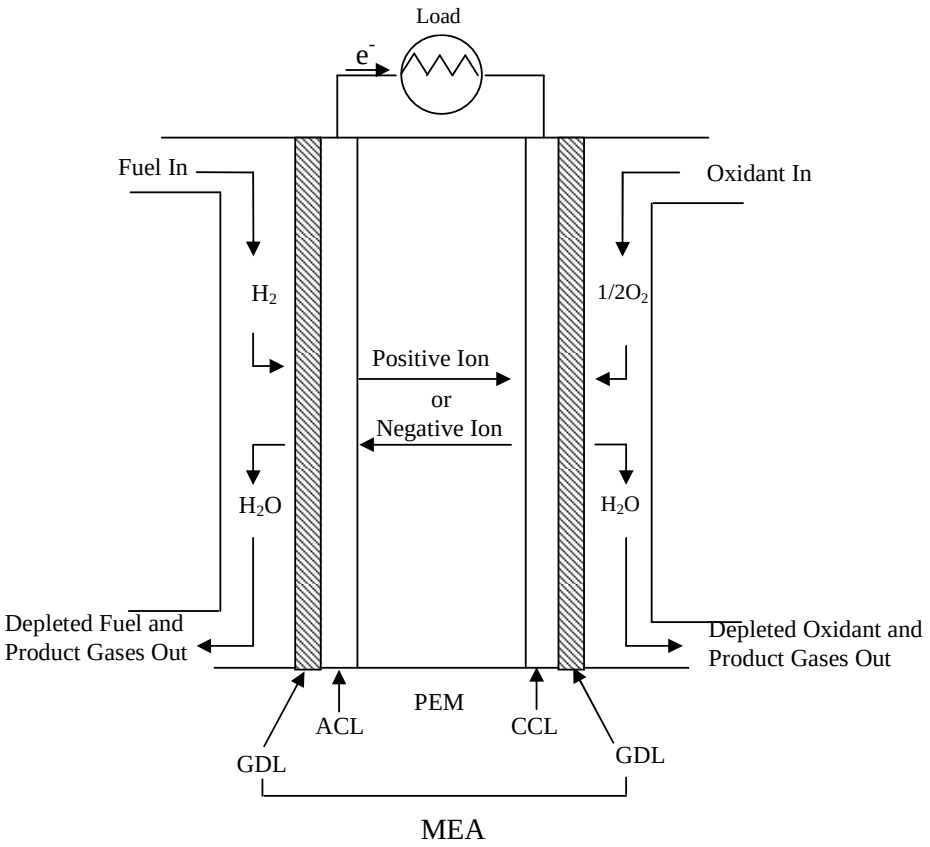

Figure 1.1 Schematic of a proton exchange membrane fuel cell structure. (GDL: gas diffusion layer, ACL: anode catalyst layer, PEM: proton exchange membrane, CCL: cathode catalyst layer and MEA: membrane electrode assembly) [3]

oxidants and polymer membrane as the electrolyte. On the anode, protons are produced and electrons are released (equation 1.1). In order to react with oxygen at the cathode (equation 1.2), protons penetrate electrolyte and electrons pass through an electrical circuit causing current.

$$2H_2 \rightarrow 4H^+ + 4e^- \tag{1.1}$$

$$O_2 + 4e^- + 4H^+ \rightarrow 2H_2O \tag{1.2}$$

The electrolyte of PEMFC is an ion exchange polymer membrane requiring proton conductivity. Typical electrodes for both anode and cathode are carbon loaded with platinum electrocatalysts [1].

PEMFC has a wide application potential in vehicles and stationary devices due to its advantages. PEMFC has excellent resistance to gas crossover due to a solid electrolyte. The low operating temperature allows rapid start-up. Corrosion problems of PEMFC are minimal since the only liquid is water so that the use of exotic materials required in other fuel cells is not needed. PEMFC is capable of high current density (over 2 kW/L). However, the applications of PEMFC are limited by certain disadvantages. The low thermal stability of polymer membranes limits their operating temperature so that a H_2-rich fuel gas with minimal or no CO, which is a catalyst poison at a low temperature, is preferred for anode. The hydrogen generation and storage is a barrier to commercialize PEMFC. The low and narrow operating temperatures also present challenge for thermal management especially at very high current densities. It is difficult to balance ensuring sufficient hydration of the electrolyte against flooding the electrolyte. Moreover, PEMFCs are sensitive to poisoning by trace levels of contaminants [1].

Although the use of oxygen rather than air will increase the power of a PEM fuel cell by about 30%, pure oxygen is mostly used in air-independent systems, such as submarines and spacecraft; otherwise, air is used since it is easy and cheap to get. However, contaminants in air may degrade the performance of PEM fuel cells.

1.3 Poisoning sources and their effect on PEMFC

Contaminants for PEM fuel cells originate from fuel for the anode, air for the cathode and other compounds from fuel cell structure components. Major contaminants identified in the operation of PEM fuel cells are listed in Table 1.2 [4].

Table 1.2 Contaminants in the operation of PEM fuel cells

Contamination sources	Typical contaminants
Air	N_2, NO, NO_2, SO_2, SO_3, NH_3 and O_3
Hydrogen fuel	CO, CO_2, H_2S, NH_3, CH_4
Bipolar metal plates	Fe^{3+}, Ni^{2+}, Cu^{2+}, Cr^{3+}
Membranes (Nafion®)	Na^{+}, Ca^{2+}, Fe^{3+}, Cu^{2+}, and Mg^{2+}
Sealing gasket	Si
Coolants	Si, Al, S, K, Fe, Cu, Cl, V, Cr
Battlefield pollutants	SO_2, NO_2, CO, propane, benzene, HCN, CNCl, Sarin, Sulfur mustard
Compressor	Oils

For the anode, hydrogen fuel is provided mainly from commercially available sources. The reformation of hydrocarbons and oxygenated hydrocarbons including methane from natural gases and methanol from biomass is the dominant method for hydrogen production. However, the reformation process results in impurities such as CO, H_2S, NH_3, organic sulfur-carbon and carbon-hydrogen compounds. Steam reforming and partial oxidation or autothermal reforming are usually used to produce hydrogen-rich gas

called “reformate” which contains 40 to 70% hydrogen, 15 to 25% CO_2, 1 to 2% CO and sulfur compounds [4].

In the cathode, air is the most practical material feed to fuel cell stack. A variety of air pollutants contaminate the fuel cell, degrading MEA by poisoning the catalysts. They include nitrogen oxides (NO and NO_2), sulfur oxides (SO_2 and SO_3), carbon oxides (CO and CO_2), ozone and other organic compounds. The major sources of these contaminants are automotive vehicle exhaust and industrial manufacturing processes. The U. S. Environmental Protection Agency (EPA) Office of Air Quality Planning and Standards (OAQPS) have set the National Ambient Air Quality Standards for CO, NO_2, O_3 and SO_2 as shown in Table 1.3 [5]. Pollutant type and level varies with working conditions. For instance, in the battlefield, there are usually more air pollutants with higher level concentrations resulting from burning fuels, volatile chemicals and generated compound during the operation of weapons.

Types of air pollutants in battlefield are included in Table 1.4 based on Moore et al. study [6]. CO, SO_2 and NO_2 are present more than the amount specified in air quality standards for public health. They are also suspected to degrade fuel cell performances.

Table 1.3 National Ambient Air Quality Standards [5]

Pollutant	Level	Averaging Time
Carbon Monoxide	9 ppm	8-hour
	35 ppm	1-hour
Nitrogen Dioxide	0.053 ppm	Annual
Ozone	0.075 ppm	8-hour
	0.12 ppm	1-hour
Sulfur Dioxide	0.03 ppm	Annual
	0.14 ppm	24-hour

***** This standard set limits to protect public health, including the health of "sensitive" populations such as asthmatics, children, and the elderly.

Table 1.4 Contaminants and their concentrations in battlefield [4]

Contaminant	CO	SO_2	NO_2	CNCl	HCN	Benzene	Propane	Sarin	Sulfur mustard
Concentration (ppm)	20	0.5	0.4	780	1780	50	90	170	15

1.4 Effects of contaminants on PEMFC performance

The effects of contaminants on fuel cell are one of the most important issues in fuel cell operation and applications. Three major areas have been addressed in the literature: theoretical and empirical modeling of contamination to provide a fundamental understanding of the mechanisms, experimental observation and validation and mitigation of the effects of contaminants [4].

Contaminants are considered to have influence on MEA (membrane electrode assembly) consisting of ACL (anode catalyst layer), CCL (cathode catalyst layer), GDL (gas diffusion layer) and PEM (proton exchange membrane). The impurities from feed gases, hydrogen for anode, air for cathode and stack component materials, can directly enter the fuel cell, poisoning the catalyst sites, affecting MEA properties such as hydrophilcity and hydrophobicity, modifying the proton transportation path and affecting water management, thus causing performance degradation. Three effects of impurities can be categorized into three major types: kinetic losses due to the poisoning of catalysts on both anode and cathode electrodes, ohmic losses due to an increase in the resistance of cell components and mass transport losses due to changes in structure and hydrophobacity of catalyst layers, PEMs and GDLs [7].

1.4.1 Contaminants on proton exchange membranes

For PEM, the cationic contaminants, such as Ca^{2+}, Fe^{3+}, Cu^{2+}, Na^{+} and Mg^{2+}, can get into the Nafion® membrane to compete with the proton for the sulfonic acid group (SO_3H) due to the sulfonic acid group's affinity for cations and thus decrease the water content resulting in a reduction in proton conductivity causing fuel cell degradation. Ammonium and Cl^- are adsorbed to catalyst surface blocking active sites for oxygen reduction reaction (ORR) and enhancing the formation of peroxide (H_2O_2) which catalyzes the radical formation reactions. The migration of metal impurities, for example Cr, allows the contaminants to spread from one electrode throughout the MEA [4, 8].

1.4.2 Contaminants for anode

For the anode, approximately 95% of hydrogen fuel is produced by steam reforming of natural gas (CH_4), which produces poisoning byproduct gases such as CO, CO_2, H_2S,

NH_3 and carbon-hydrogen compounds. Carbon monoxide is reported to have the worst effect on fuel cell performance due to its strong bond with catalyst Pt resulting in reduction of active sites available for hydrogen adsorption and oxidation. Increases in operating temperature and humidity reduce CO coverage on the catalyst by promoting CO oxidation with an OH_{ads} group [9]. At as low as 10 ppm CO in hydrogen stream, anode performance was slightly affected while 100 ppm CO caused a remarkable increase of anodic overpotential [10]. Carbon dioxide does not affect anode performance directly but is catalytically converted to carbon monoxide [4]. H_2S and ammonia also cause voltage loss by blocking active site on catalysts [4]. After exposure to 50 ppm hydrogen sulfide, only partial recovery of membrane electrode assembly properties by the electrochemical oxidation is achieved [11].

1.4.3. Contaminants on cathode

This research will focus on the effects of air impurities fed into the cathode. SO_x and NO_x have been found as the dominant contaminants for cathode.

1.4.3.1 Effect of nitrogen oxide At low NO_2 concentration, 1 ppm, the cell performance has been reported to decrease by about 10% after running 100 hour. However, the concentration of NO_x in the exhaust of internal-combustion engine vehicles (IEV) on the road can easily exceed 50 ppm, even reaching up to 300 ppm [12, 13]. According to the literature, 85~95% of NO_x is NO [13, 14]. Yang et al. simulated the exhaust of IEV with mixture of NO and NO_2 in the ratio of 9:1 which was mixed with air to obtain 1480, 140 and 10 ppm NO_x in air stream in order to investigate the effect of NO_x on fuel cell performance [12]. The polarization curves of different NO_x concentrations are shown in Figure 1.2. Introduction of 10 ppm NO_x to the cathode slightly decreased the cell

performance and the decline increased with increased NO_x concentration. Experiments have proved that the degradation due to NO_x can be recovered by refeeding clean air as shown in Figure 1.3. With the introduction of 124 ppm NO_x, cell voltage dropped by about 42% but recovered to the initial voltage after operating with clean air for 120 min. After injecting 124 ppm NO_x for four times, the cell could recover approximately by 94%. The abrupt voltage drop with the introduction of NO_x was probably due to the quick adsorption of NO_x on catalyst surface suppressing the oxygen reduction reaction (ORR). But the weak adsorption is reversible and adsorbed NO_x was desorbed recovering the cell voltage. The absence of any oxidation peaks in cyclic voltammetry spectra reported by Mohtadi et al. revealed that the poisoning of NO_2 is not catalyst surface poisoning and suggested that the ionomer or the catalyst-ionomer interface could be affected by the exposure to NO_2 [15]. The possible mechanism of NO_x effect is that NO is oxidized to NO_2 (equation 1.3) which becomes electrochemically reduced on the cathode and thus competes with O_2 for Pt sites forming NH_4^+ (equation 1.4). NH_4^+ is an ionomer poison as the effect of NH_3 on anodes.

$$2NO + O_2 \rightarrow 2NO_2 \tag{1.3}$$

$$NO_2 + 8H^+ + 7e^- \rightarrow NH_4^+ + 2H_2O \tag{1.4}$$

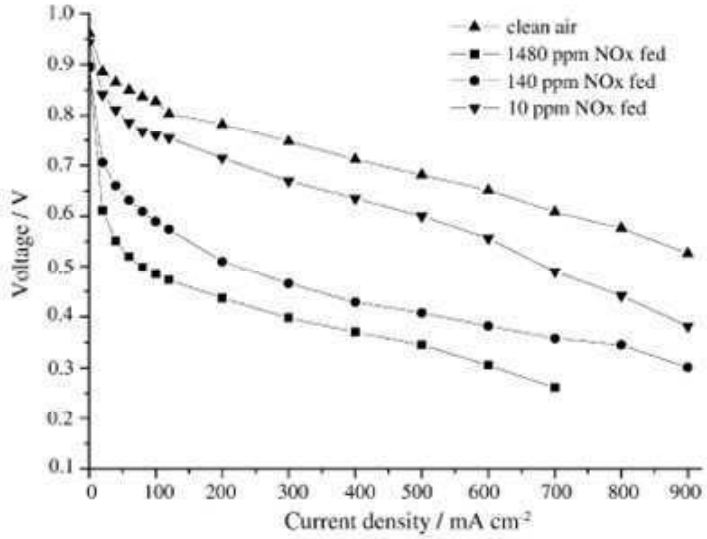

Figure 1.2 Polarization curves with different NO_x concentrations [11].

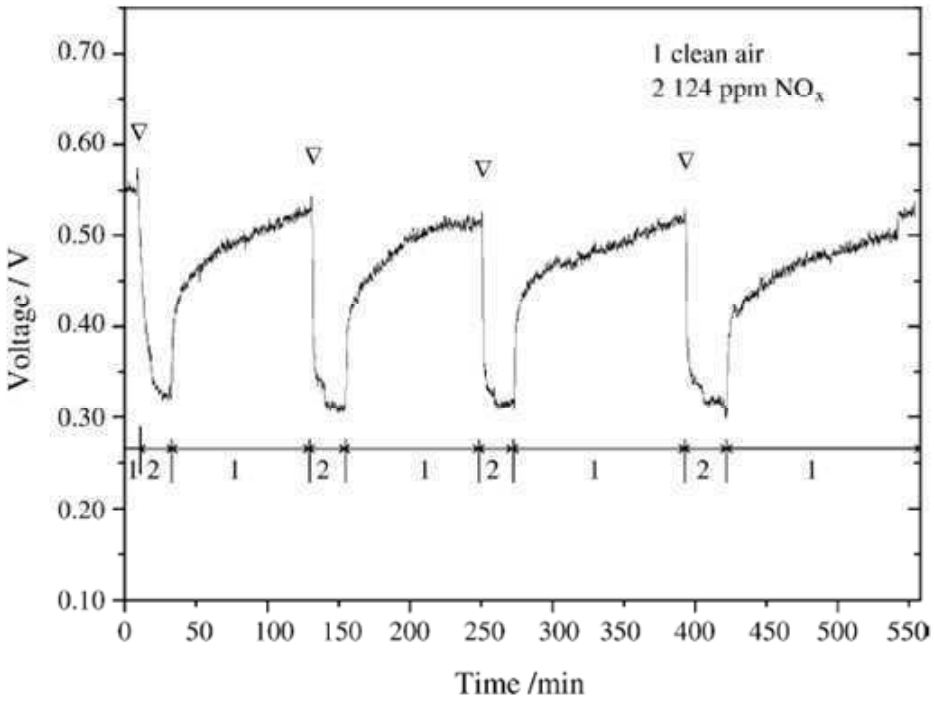

Figure 1.3 Periodic test of the reversibility of cell performance. The fuel cell was discharged at 12.5 A, 338 K, ambient pressure and the utilization rates of H_2 and air were 80 and 40%, respectively [11].

1.4.3.2 Effect of sulfur oxide Several researches have studied the effect of SO_2 on cell performance. Moore et al. did not observe detrimental effect when 500 ppb SO_2 was present in the air [6]. To observe the accumulation effect of SO_2 in a long term, 1 ppm SO_2/air was fed to the cathode and the cell potential declined by 35% after running 100 hour [16]. Mohtadi et al. introduced 2.5 and 5 ppm SO_2 in the air stream and compared it with the same amount of NO_2 and found that the poisoning effect of SO_2 appear to be severe according to the polarization curve data [15]. The degradation of cell performance after exposure to SO_2 recovered partially with neat air as shown in Figure 1.4 but the effect varied with SO_2 concentration. Although the SO_2 concentration was different, the total dosage of SO_2 remained the same by controlling exposure time. 23 hour exposure to 5 ppm SO_2 degraded the cell current by about 78% while 53% current decrease was observed after exposing to the same dose of 2.5 ppm SO_2. Moreover, the recovery of current after applying 2.5 ppm SO_2 was lower compared to 5 ppm SO_2. After cyclic voltammetry, cell voltage almost recovered completely [15].

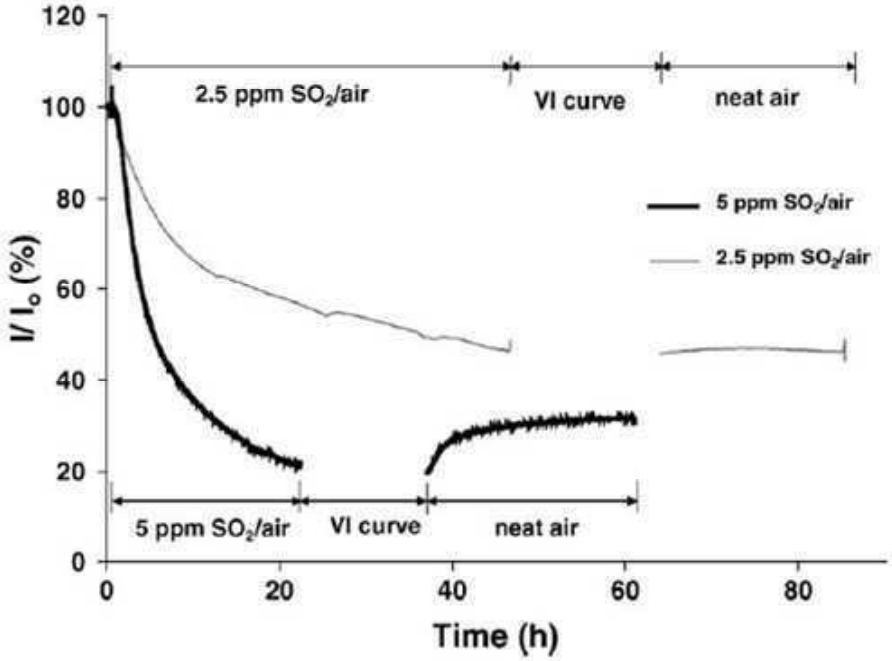

Figure 1.4 Cell current after exposure to 2.5 and 5 ppm SO_2 in air [15]

The mechanism of SO_2 poisoning and its effect on cell performance was analyzed based on cyclic voltammetry by Mohtadi et al. Two oxidation peaks at 0.89 and 1.05 V are shown in Figure 1.5 [15]. They correspond to the presence of two sulfur species adsorbed on the surface of the Pt catalyst. SO_2 was reduced to sulfur on Pt with the formation of SO intermediate as shown in reaction Equations1.5 and 1.6. Figure 1.6 shows the durability of the cell in 5 ppm SO_2/air. Unlike the effect of NO_x on cell performance, the degradation caused by SO_2 cannot be recovered to or close to the intial performance by introducing neat air [15].

$$SO_2 + 2H^+ + 2e^- \xrightarrow{Pt} Pt - SO + H_2O \quad (1.5)$$

$$Pt - SO + 2H^+ + 2e^- \rightarrow Pt - S + H_2O \quad (1.6)$$

where $Pt-SO$ and $Pt-S$ represent that SO and S attach to catalyst Pt.

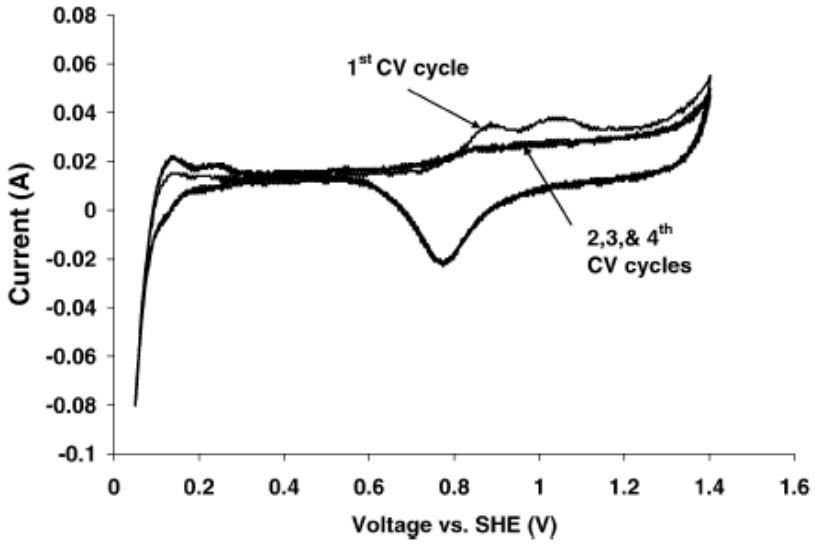

Figure 1.5 Cyclic voltammetry spectra after cathode exposure to 2.5 ppm SO_2 in air [15]

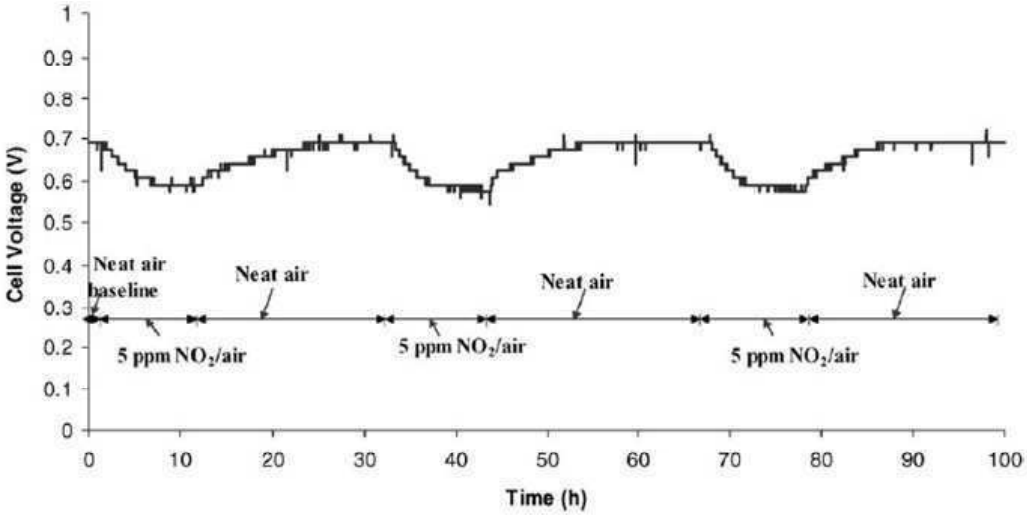

Figure 1.6 Durability of PEMFC when exposure to 5 ppm SO_2 in air [15]

1.5 Need for PEMFC cathode filter

As discussed, even trace amounts of impurities in fuel or air stream will severely poison the anode or the cathode. Some contaminants can irreversibly be adsorbed onto catalyst and thus block the active sites of the catalysts. Most approaches have focused on mitigation of contamination on the fuel side, such as pre-treatment of reformate, anode oxidant-bleeding and CO tolerant catalyst synthesis. However, developments in mitigation of cathode poisons have not been well documented [4]. In order to commercialize PEMFC, contamination prevention on the cathode side must be addressed. Two strategies to purify the feed air stream have been suggested. One is the use of filtration to filter poisons out and the other is the development of contamination tolerance MEA components such as catalysts [4]. The later is more challenging due to the variety of contaminants. Filtration technology is more feasible and separate filters can be developed for either anode or cathode applications. Considering the negative effect of contaminants on the cathode, sulfur dioxide has more severe influence on the PEMFC performance as discussed above. Therefore, sulfur dioxide will be our first filtration target in this study. Kennedy et al. has proposed methodologies for design of fuel cell cathode air filters [17, 18].

1.6 Industry methods for sulfur dioxide purification

Sulfur dioxide is usually produced by volcanoes and in various industrial processes. The main sulfur dioxide emission is from combustion of coal and petroleum, which are currently the main energy resources. The most widely used purification technique to clean sulfur dioxide before released into atmosphere is called flue gas desulfurization.

Due to the US EPA's Acid Rain Program, the America has witnessed a 33% decrease in emissions between 1983 and 2002, resulted from flue gas desulfurization [5]. As this technology advances and becomes more efficient, there are many variations on how this process is executed, such as wet-scrubbing systems, spray-dry scrubbing, sodium sulfite solution and gas phase oxidation with ammonia [19]. Most of the coal burning utilities have chosen lime-based web scrubbing. However, there are a number of disadvantages of this method. Investment cost is usually high to purchase lime-based scrubbing materials. Wet scrubbing system consumes a large amount of water and the byproducts of calcium sulfate/sulfite have low value [20]. Carbon dioxide released in this system is a monitored greenhouse gas [21]. The most important issue is that no industrial process is 100% effective and some sulfur dioxide still escapes into the atmosphere (30ppm) [19, 20]. That will be a problem for high quality air requirement for PEMFC since even a trace amount of sulfur dioxide will cause performance degradation as discussed previously. On the other hand, activated carbon offers numerous advantages: a small sorbent make-up, generation of relatively small amounts of by-products, recovery of sulfur as useful sulfur-containing products, simultaneous removal of sulfur dioxide and nitrogen oxide and elimination of large water consumption [22].

1.7 Porous adsorbents in sulfur dioxide removal

Activated carbons or other porous adsorbents, which have been widely used in purification or filtration systems, can be considered for complete removal of sulfur dioxide through adsorption, either physisorptions or chemisorptions, before air is fed into fuel cell system.

Some researche has been conducted on desulfurization over porous adsorbents, such as alumina, zeolites and activated carbons. They have been treated to enhance sulfur dioxide removal efficiency. We are focusing on the most popular adsorbent, activated carbon because it can remove nearly every impurity found in the combustion flue gas, including particulate material, heavy metals, organic materials and other air toxics [23].

The well-known activated carbon can be classified into three categories according to the shape: granular activated carbon (GAC), powdered activated carbon (PAC) and extruded activated carbon (EAC). Activated carbon fiber (ACF) is a relatively new adsorbent for filtration or purification techniques. Currently used carbon-based flue gas desulfurization systems have mostly consisted of granular activated carbons [23]. The sulfur dioxide capacity of bare activated carbon usually decreases with the increased temperatures. In order to address this problem, they are loaded with metals which result in good sulfur dioxide adsorbents at both low and relatively high temperatures.

1.8 Advantages of ACFs in comparison with GAC and PAC

The desulfurization properties of the four activated carbons mentioned above have been compared for material selection to optimize sulfur dioxide purification technique. GAC and PAC are widely used in a variety of applications, such as gas purification, water purification, medicine manufacturing, sewage treatment, chemical purification, mercury scrubbing and filter masks [24]. A large volume of adsorption devices are usually needed in applications due to the relatively slow adsorption rate of GAC, which also results in slow throughput. Typical size of GAC varies between 200 and 1000 μm. PAC, which is smaller than GAC with the typical particle size between 20 and 200 μm, is found to have

faster adsorption rates. However, powdered activated carbons may compact under flow, leading to a strong flow resistance [25].

The adsorption kinetics and capacities of GAC, PAC and ACF on methylene blue were investigated by Shmidt et al. [25]. The adsorption rate of ACF is an order of magnitude faster than that by PAC and two orders of magnitude faster than that by GAC. The adsorption capacity of ACF was three times higher than the adsorption capacity of PAC and ten times higher than that of GAC. However, the diffusion coefficient in ACF was found to be 2×10^{-11} cm^2/s in comparison with 4.6×10^{-10} cm^2/s for PAC and 3.5×10^{-8} cm^2/s for GAC [25]. Although ACFs possess a smaller diffusion coefficient, which may be because of the tighter packed carbon layers, compared to ACP and GAC, they exhibit a faster adsorption rate than GAC and PAC. This is due to the ratio of macropore size to the adsorbent size. For ACFs, the macropores are relatively large as compared to fiber diameters and therefore a single macropore may lead directly into the center of the ACF. Macropores in PAC and GAC are comparable in size to macropores in ACF but macropores in PAC and GAC are much smaller than the diameters of PAC and GAC particles. Penetration of adsorbate into the center of PAC and GAC is controlled by diffusion through micropore layers that interconnect individual macropores [25]. In other words, the higher the ratio of macropore size to the adsorbent size, the faster the adsorption rate. The effective macropore surface area was estimated by Shmidt as well [25]. ACF was found to have the smallest macropore surface area of 6.3 m^2/g, which is half of macropore surface area of PAC at 14 m^2/g and one fourteenth of that of GAC at 87 m^2/g [25]. However, the influence of effective macropore surface area on the adsorption rate is less than that caused by the adsorbent diameters. Application of PAC is

limited by possible second contamination [26]. In order to improve the contacting efficiency, a technique which entraps PAC in microfiber network has been patented [27, 28].

ACFs have their own characteristics compared to GAC and PAC [26]. First of all, the features of pores in ACFs are different from GAC. Most of the pores in ACFs are micropores with the presence of some mesopores and macropores. Due to the small fiber diameters, pores can directly reach the center of fibers and therefore the diffusion path of adsorbate to reach the adsorption sites is short. The pore schematics and pore size distribution of typical GAC and ACF are shown in Figures 1.7 and 1.8, respectively. The more open characteristic of ACF may contribute to the less possibility to be blocked. GAC and PAC have plenty of micropores and mesopores which adsorbates usually reach after passing macropores. The blockage of macropores would close the access of adsorbates to smaller pores where adsorption would occur. ACF usually has a narrower pore size distribution and a higher surface area. Small fiber diameters also result in a larger contact surface area between adsorbents and adsorbates and thus even contact would be achieved. All of these characteristics of ACF may explain the faster adsorption rate and the higher adsorption capacity in desulfurization process [29]. ACFs are able to remove not only high concentration contaminants but also low concentration contaminants. For instance, 100 ppm toluene can pass through GAC while the lowest toluene concentration ACF can absorb is 10 ppm [26]. ACFs have also been found to have lower pressure drop as compared to GAC [29]. ACF has a lower volume density and lower filtration resistance, which is about 1/3 of GAC. Therefore, unlike GAC, ACFs are able to filter liquids with a higher viscosity and less penalty of energy consumption.

ACFs offer the fabrication flexibility which GAC does not have, and thus they are easier to be made into filter media or devices. ACFs can be made in various forms such as fabrics, nonwovens, paper and composites, which make them suitable for handling in special devices [29-32]. Zhao et al. pointed to some merits of ACFs in specific applications. In water purification systems, ACFs have advantages of less possibility to produce ash, less pressure drop and a higher water flow rate. In air purification systems, ACFs show faster adsorption and desorption rate. In ammonia, toluene, sulfur dioxide and nitrogen dioxide cleaning systems, ACFs showed the higher removal efficiency and adsorption capacities [26].

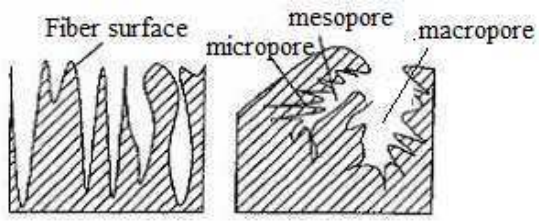

(a) ACF (b) GAC

Figure 1.7 Schematic of pore structures of a) ACF and b) GAC [24]

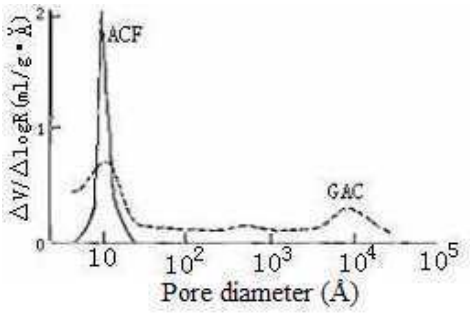

Figure 1.8 Pore size distribution of ACF and GAC [24]

Furthermore, the desulfurization abilities of GAC (made from industrial coke) and viscose-based ACF were tested and compared under the same conditions (70ºC) with a gas stream of 3 L/min by Xu et al [33]. With the presence and absence of water, GACs reached their breakthrough points quickly after the test started while ACFs showed 55 min (with moisture) and 20 min (without moisture) breakthrough time, respectively. However, the utilization of ACFs is low with the short breakthrough period, which is due to very small internal pore sizes of ACFs, compared to sulfur dioxide molecules (bond distance S-O=1.432Å±0.003Å and bond angle OSO=119.53º±0.4º). Capillary condensation

takes place within these pores, resulting in large amounts of adsorption [33]. PAN-based ACFs have been reported by Mochida et al. to have the largest sulfur dioxide removal efficiency among the commercially available active carbons [34].

1.9 Manufacturing and characterization of activated carbon fibers

Manufacturing of activated carbon fibers can be basically classified in terms of the preparation method: physical activation (or gas activation) and chemical activation (or reagent activation). Similar to the preparation of other shapes of activated carbons, there are three basic procedures to make activated carbon fibers: stabilization or oxidation, carbonization and activation. The stabilization is usually carried out at 200~300°C in air for prevention of fibers from melting during the subsequent high temperature carbonization. Stabilization is required for producing ACF from PAN and pitch fibers, but not those from phenolic resin and cellulose because of their thermosetting nature [35]. In the carbonization process, non-carbon elements, such as oxygen and nitrogen, are eliminated through high temperature heat treatment; residual elementary carbon atoms

group into sheets and form condensed aromatic rings. Porous structure is initiated at this stage; however, the adsorption capacity of carbon fibers is still insignificant because most of pore mouths are still blocked with some tarry substances [36], which needs the next stage called activation. During activation, disorganized carbon groups are rearranged and micropores, mesopores and macropores are generated with the help of activating agents. The difference between physical and chemical activation lies in the activating agents and thus the activation process.

In chemical activation, raw materials are first immersed in inorganic salt, such as zinc chloride, phosphoric acid or potassium sulfide [37]. The most popular activation agent in industry was zinc chloride, however, its use has been discontinued due to its damage to environment [38]. Lately, ammonia, potassium hydroxide and sodium hydroxide have been reported as the reagents to make activated carbon fibers chemically [39-41]. Advantages of chemical activation include the short preparation time since carbonization and activation are combined into one step making chemical activation a two-step process and the lower activation temperature.

Unlike chemical activation, the processes of carbonization and activation take place in two separate steps in physical activation. Several physical processes are involved in physical activation including the removal of the tarry products condensed in the pore by the flow of activating agents and the increase of volume as a result of diffusion and evaporation of the tarry products [42].

The most widely used precursors for activated carbons fibers include polyacrylonitrile, carbon fiber, petroleum based pitch, viscose rayon, and phenolic resin [37, 43-45]. Some other fibers have been tried lately to produce ACFs as well, such as polyvinyl chloride,

Nomex® aramid fibers and polyamide [37, 44, 46, 47]. Pore characteristics and physical properties of activated carbon fibers are influenced by a series of factors, including chemistry composition of precursors, activating agents, heating temperature, process period, and flow rate of environmental gases [12, 37, 38, 40, 48].

1.10 Sulfur dioxide adsorption over activated carbon fibers

1.10.1 Sulfur dioxide removal on bare activated carbon fibers

Desulfurization properties of bare ACFs have been studied by some researchers and are found to be dependent on precursors of ACFs, characteristics of ACFs and experimental conditions, such as the composition of carrier gas, flow rate of main gas stream, temperature, and concentration of challenge gas [33, 49].

Compared to pitch-based ACFs, polyacrylonitrile-based activated carbon fibers (PAN-based ACFs) were found to have higher activity while they were subjected to 1000 ppm sulfur dioxide with a flow rate of 100 mL/min at 30 and 50°C. Breakthrough times were longer than 60 hours [50].

Adsorption capacity of SO_2 onto ACFs is dependent not only on textural characteristics, but also surface chemistry, quantity and nature of oxygen-containing and nitrogen-containing functional groups [33, 49]. ACFs impregnated in ammonia increased the nitrogen-containing surface groups (pyidyl C_5H_4N- and C_4H_4N-) leading to increased SO_2 adsorptive performance [33].

Mochida et al. claimed that physical properties of PAN-based ACFs, such as surface area, micropore volume and external surface area appear to be less influential on their SO_2 removal performance [51]. However, Daley et al. obtained different results on phenolic-based ACFs. They found out that initial rate of SO_2 adsorption was inversely

related to pore size, while, at longer times, the amount of SO_2 adsorbed was dependent on both the pore size and pore volume [52]. ACFs may be oxidized with nitric acid/sulfuric acid to introduce more oxygen groups on fiber surfaces followed by heat treatment which results in decomposition of oxygen groups to develop free sites which was found to be proportional to SO_2 adsorption [52, 53]. Activation method also was found to have effect on the activity of ACFs in sulfur dioxide capacity. Activity of steam activated ACFs continuously declines while the potassium hydroxide activated ACFs produced high steady stage sulfur dioxide conversion which was probably due to high oxygen content on steam activated ACFs according to Martin-Gullon's research [54].

1.10.2 Treatment for promotion of sulfur dioxide removal

Attempts have been made to increase sulfur dioxide removal efficiency with treated activated carbons with various approaches: heat treatment, acid pretreatment, loading of base and loading of alkali metals.

1.10.2.1. Heat treatment Heat treatment at high temperatures under while nitrogen atmosphere was found to have effect on sulfur dioxide capacity of activated carbon. Pore structures of activated carbons were found to be influenced by both acid pretreatment and heat treatment: surface area and pore volume decreased a little by oxidation of acid and increased again by heat treatment while pore size was barely affected [52].

Both active carbons and PAN-based ACFs were subjected to high temperature heat treatment in order to increase SO_2 capacity. The capacity of ACFs was increased drastically while only a slight increase of capacity was observed for GAC. At 800ºC heating, SO_2 capacity of ACFs was tripled [51].

To maximize the SO_2 capacity, appropriate temperature of heat treatment is expected to vary with ACFs because the number and natures of oxygen groups on the surface are strongly subjective to the extent of activation [51]. The mechanism was proposed by Mochida and two different adsorption sites were proposed. One is for SO_2 adsorption and oxidation and the other one is for holding H_2SO_4. Polar sites can hold H_2SO_4; however, too many polar sites in the unit area may cause repulsion of polar adsorbate or form the liquid phase of H_2SO_4 at the pore mouth, inhibiting the diffusion of H_2SO_4 as well as SO_2 into pores. Therefore, a balanced number of oxygen groups prepared by heating is optimal for maximum SO_2 adsorption [51].

Pretreatment with nitric acid or sulfuric acid has been applied before heat treatment of activated carbon. Oxidation of activated carbon by nitric acid could offer oxygen groups which would be decomposed with high temperatures leaving free sites behind for enhancement of SO_2 adsorption [52, 55]. Oxidized ACFs showed a reduction of SO_2 capacity at low temperature although it was regained by subsequent heat treatment. Heating could not increase the SO_2 capacity indefinitely, which was limited by the available pore volume [52].

1.10.2.2. Impregnation with basic chemicals Considering the acid of sulfur dioxide, basic chemicals, e. g., K_2CO_3, KOH and ammonia, can be loaded on activated carbon for desulfurization. Two impregnation methods are usually employed to deposit catalysts on porous supports: regular impregnation and wetness incipient impregnation. In the former, porous materials are simply immersed in desired precursor solutions followed by drying to deposit chemicals on supports. The wetness incipient impregnation is a commonly used technique for the synthesis of heterogeneous catalysts in which a solution is added

to a support containing the same pore volume as the volume of solution that was added. Capillary action draws the solution into pores. The catalyst can be dried and calcined to drive off the volatile components within the solution, depositing chemicals on the catalyst surface. However, the maximum loading is limited by the solubility of the precursor in the solution. The concentration profile of the impregnated compound depends on the mass transfer conditions within the pores during impregnation and drying [56].

Activated carbon impregnated with potassium hydroxide was reported to achieve simultaneous removal of sulfur dioxide, nitrogen monoxide and nitrogen dioxide by Lee et al. [57]. The sulfur dioxide capacity of K_2CO_3-impregnated activated carbons prepared by soaking varies linearly with K_2CO_3 loading up to 12wt%. Above 12wt%, the capacity levels out and then decreases since high loads of K_2CO_3 may aggregate and block pores of activated carbon. However, it was reported that the incipient wetness impregnation may cause aggregation but did not block carbon pores [58]. The release of carbon monoxide during desulfurization limits the application of K_2CO_3 in PEMFC systems due to poisoning effect of carbon monoxide on the fuel cell unit. Xu et al. impregnated GAC and viscose-based ACFs in ammonia. The impregnation of activated carbon fibers in ammonia introduced more nitrogen-containing groups (pyidyl C_5H_4N- and C_4H_4N-) on carbon surface enhancing SO_2 capacity [33].

1.10.2.3. Activated carbon supported metal catalysts Several kinds of metal were treated onto the activated carbons to increase the SO_2 removal efficiency or SO_2 adsorption capacity [29, 55, 59, 60]. Transition metals, such as Fe, Ni, Co, Mn and V were deposited on pitch-based activated carbon by immersing the carbon in aqueous solution of metal nitrates followed by filtration, washing, drying and calcinations at 800ºC in nitrogen

flow. Properties of metallic derivatives, such as BET surface area, acidic and basic surface characteristics, were found to be similar to the bare activated carbon without treatment. With the nitrogen as the carrier gas, AC supported with vanadium is the most favorable SO_2 adsorbent in comparison with other four metal-AC sorbents. Moreover, SO_2 capacities of V/AC and Fe/AC sorbents were more likely to be promoted by the oxygen and water in the carrier gas (185 mg SO_2/g V-AC and 172 mg SO_2/g Fe-AC in the mixture of SO_2+O_2+H_2O for 0.3 wt% vanadium and 0.8 wt% iron, respectively) [60]. Polyacrylonitrile-based ACFs were loaded with Cu, Co, Mg, Mn and N_i and increased SO_2 activity was obtained. Among these metal-ACFs, Co/ACF (34wt% of cobalt) showed the best activity (93 mg SO_2/g carbon) and a constant removal ratio of sulfur dioxide above 87% during continuous exposure to the flow of SO_2+O_2+H_2O with the flow rate of 125 mL/min for more than 216 hour [29].

Copper catalysts supported on acid treated AC were designed and studied by Tseng et al., who found out that carbon acted as catalyst support for copper oxide provided a higher catalytic activity for sulfur dioxide. Sulfur dioxide was catalytically oxidized to sulfur trioxide which was converted be copper sulfate. Acid pretreatment on AC before loading copper dioxide provided the surface oxygen content to enhance the activity of sulfur dioxide oxidation [55]. The regeneration of spent CuO/AC was achieved by heating in inert gases between 260 and 480°C without the need of reducing agents. The decomposition of surface oxygen complexes on carbon surfaces resulted in the evolution of CO_2 and CO which act as the reducing agents in regeneration process [59]. However, during regeneration, the over reduction of Cu^{2+} to Cu^0 may occur, which my results in sintering of copper reducing the desulfurization capacity of regenerated Cu/carbon. Ma et

al. developed a regenerable Fe/AC desulfurizer which may have a longer service life than Cu/AC [22]. H_2SO_4 and $Fe_2(SO_4)_3$ were produced during the desulfurization process and the spent Fe/AC desulfurizer was able to be regenerated by NH_3 at 350ºC to directly form solid ammonium-sulfate salts [22].

1.11 Objectives of the research

Because of advantages of ACFs in the adsorption rate and the fabrication flexibility, they are considered in this study to removal sulfur dioxide from air fed into fuel cell systems. According to literature review, modification on ACFs attempting to promote sulfur dioxide adsorption has focused on heat treatment and metal load for catalytically oxidation of sulfur dioxide to sulfur trioxide. However, both heat treatment and impregnation of metal require high temperature and inert gas, which are energy consuming. Impregnating of activated carbon fibers with alkali and oxidants will address this problem without the need of nitrogen as the protecting gases and high temperature. The adsorption mechanism of ACF supported oxidants will be studied. Since the current available models in the literature are estimating SO_2 adsorption over bare activated carbon fibers, models for prediction of adsorption performance of ACFs with promoters (potassium permanganate) will be developed for different conditions: the absence of water and oxygen, the presence of oxygen, the presence of water and the copresence of water and oxygen. Although model for the prediction of adsorption of sulfur dioxide and other adsorbate over bare activated carbon fibers have been reported by the literature, the impregnated ACFs or AC are barely described in these models. In the current research, a model will be developed to predict the adsorption properties of the modified ACFs.

References

1. Fuel Cell Handbook (Sixth Edition), U.S. Department Of Energy, West Virginia, (2002).
2. Podatz, P., Onder, C. and Guzzella, L., Air supply system of a PEMFC stack dynamic model, *Fuel Cells*, 5 (1), 126-133, (2005).
3. Larminie, J. and Dicks, A., Fuel cell systems explained, John Wiley & Sons Ltd, West Sussex, England, (2003).
4. Cheng, X., Shi, Z., Glass, N., Zhang, L., Zhang, J. J., Song, D. T., Liu, Z. S., Wang, H. J. and Shen, J., A review of PEM hydrogen fuel cell contamination: Impacts, mechanisms, and mitigation, *J. Power Sources*, 165 (2), 739-756, (2007).
5. www.wikipedia.org, Jan 2010 accessed.
6. Moore, J. M., Adcock, P. L., Lakeman, J. B. and Mepsted, G. O., The effects of battlefield contaminants on PEMFC performance, *Journal of Power Sources*, 85 (2), 254-260, (2000).
7. Zhang, J. J., Wang, H. J., Wilkinson, D. P., Song, D. T., Shen, J. and Liu, Z. S., Model for the contamination of fuel cell anode catalyst in the presence of fuel stream impurities, *Journal of Power Sources*, 147 (1-2), 58-71, (2005).
8. Collier, A., Wang, H. J., Yuan, X. Z., Zhang, J. J. and Wilkinson, D. P., Degradation of polymer electrolyte membranes, *International Journal of Hydrogen Energy*, 31 (13), 1838-1854, (2006).
9. Jiang, R., Kunz, H. R. and Fenton, J. M., Electrochemical oxidation of H_2 and H_2/CO mixtures in higher temperature (T_{cell}>100° C) proton exchange membrane

fuel cells: electrochemical impedance spectroscopy, *Journal of The Electrochemical Society*, 152 (7), A1329-A1340, (2005).

10. Han, J. N., Park, G. G., Yoon, Y. G., Yang, T. H., Lee, W. Y. and Kim, C. S., A new evaluation method of anode/cathode used for polymer electrolyte membrane fuel cell, *International Journal of Hydrogen Energy*, 28 (6), 609-613, (2003).
11. Mohtadi, R., Lee, W. K., Cowan, S., Van Zee, J. W. and Murthy, M., Effects of hydrogen sulfide on the performance of a PEMFC, *Electrochemical and Solid State Letters*, 6 (12), A272-A274, (2003).
12. Yang, D. J., Ma, J. X., Xu, L., Wu, M. Z. and Wang, H. J., The effect of nitrogen oxides in air on the performance of proton exchange membrane fuel cell, *Electrochimica Acta*, 51 (19), 4039-4044, (2006).
13. Kandylas, I. P., Haralampous, O. A. and Koltsakis, G. C., Diesel soot oxidation with NO_2: Engine experiments and simulations, *Industrial & Engineering Chemistry Research*, 41 (22), 5372-5384, (2002).
14. Betournay, M. C., Bonnell, G., Edwardson, E., Paktunc, D., Kaufman, A. and Lomma, A. T., The effects of mine conditions on the performance of a PEM fuel cell, *Journal of Power Sources*, 134 (1), 80-87, (2004).
15. Mohtadi, R., Lee, W. K. and Van Zee, J. W., Assessing durability of cathodes exposed to common air impurities, *Journal of Power Sources*, 138 (1-2), 216-225, (2004).
16. Jing, F. N., Hou, M., Shi, W. Y., Fu, J., Yu, H. M., Ming, P. W. and Yi, B. L., The effect of ambient contamination on PEMFC performance, *Journal of Power Sources*, 166 (1), 172-176, (2007).

17. Kennedy, D. M., Cahela, D. R., Zhu, W. H., Westrom, K. C., Nelms, R. M. and Tatarchuk, B. J., Fuel cell cathode air filters: Methodologies for design and optimization, *Journal of Power Sources*, 168 (2), 391-399, (2007).

18. Kennedy, D., Fuel cell cathode air filters: methodologies, Master Thesis. Auburn, Auburn University, (2007).

19. www.ehow.com, Jan 2010 accessed.

20. Huda, M., High-efficiency SO_2 removal using activated carbon fibers, (2007).

21. Grutzeck, M., SO_2 removal from flue gases using utility synthesized zeolites, Report, The Pennsylvania State University, (1999).

22. Ma, J. R., Liu, Z. Y., Liu, S. J. and Zhu, Z. P., A regenerable Fe/AC desulfurizer for SO_2 adsorption at low temperatures, *Applied Catalysis B-Environmental*, 45 (4), 301-309, (2003).

23. Debarr, J. A., Lizzio, A. A. and Daley, M. A., Adsorption of SO_2 on bituminous coal char and activated carbon fiber, *Energy & Fuels*, 11 (2), 267-271, (1997).

24. Wey, M. Y., Fu, C. H., Tseng, H. H. and Chen, K. H., Catalytic oxidization of SO_2 from incineration flue gas over bimetallic Cu-Ce catalysts supported on pre-oxidized activated carbon, *Fuel*, 82 (18), 2285-2290, (2003).

25. Shmidt, J. L., Pimenov, A. V., Lieberman, A. I. and Cheh, H. Y., Kinetics of adsorption with granular, powdered, and fibrous activated carbon, *Sep. Sci. Technol.*, 32 (13), 2105-2114, (1997).

26. Zhao, L., Huang, X., Gu, Q. and Di, Y., The performance comparison of ganular activated carbon filter and fiber filter of activated carbon, *Contamination Control & Air-conditioning Technology*, (2), (2004).

27. Tatarchuk, B., Chang, B. K., Lu, Y., Luna, E. and Cahela, D., Auburn University, Microfibrous entrapment of small reactive particulates and fibers for high contacting efficiency removal of contaminants for gaseous or liquid streams, patent 7501012, USA,(2009).

28. Tatarchuk, B., Chang, B. K., Lu, Y., Chen, L., Luna, E. and Cahela, D., Auburn University, Microfibrous entrapment of small reactive particulates and fibers for high contacting efficiency removal of contaminants from gaseous or liquid streams, patent 20050169820, USA,(2005).

29. Wang, J. Y., Zhao, F. Y., Hu, Y. Q., Zhao, R. H. and Liu, R. J., Modification of activated carbon fiber by loading metals and their performance on SO_2 removal, *Chin. J. Chem. Eng.*, 14 (4), 478-485, (2006).

30. Edens, R. L., Gadsby, E. D., Lindsay, J. D., Pike, R. D. and Mangun, C., Kimberly-Clark Worldwide, Inc. , Flexible activated carbon substrates, patent 20040121688, USA,(2004).

31. Hsieh, S.-J., Clothing material structure of fiber cloth containing PAN series activated carbon, patent 20040092188,(2004).

32. Giglia, R. and Battistelli, E., American Cyanamid Company Non-woven activated carbon fabric, patent 4904343, USA,(1990).

33. Xu, L., Guo, J., Jin, F. and Zeng, H., Removal of SO_2 from O_2-containing flue gas by activated carbon fiber (ACF) impregnated with NH_3, *Chemosphere*, 62, 823-826, (2006).

34. Mochida, I., Hirayama, T., Kisamori, S., Kawano, S. and Fujitsu, H., Marked increase of SO2 removal ability of polyacrylonitrile-based activated carbon fiber by heat treatment at elevated temperatures, *Langmuir*, 8, 2290-2294, (1992).

35. Worasuwannarak, N., Hatori, S., Nakagawa, H. and Miura, K., Effect of oxidation pre-treatment at 220 to 270 degrees C on the carbonization and activation behavior of phenolic resin fiber, *Carbon*, 41 (5), 933-944, (2003).

36. Gaur, V., Preparation and characterization of activated cabron fabric for the control of BTX, SO_2 and NO_x emissions, Indian Institute of Technology Kanpur, (2005).

37. Wu, Q. L., Zhang, Z. H., Gu, S. Y. and Gong, J. H., Macroporous activated carbon fibers from rayon precursors impregnated with phosphoric acid, *Journal of Macromolecular Science Part A - Pure and Applied Chemistry*, 43 (11), 1787-1792, (2006).

38. Su, C. I. and Wang, C. L., Optimum manufacturing conditions of activated carbon fiber absorbents. I. Effect of flame retardant reagent concentration, *Fibers and Polymers*, 8 (5), 477-481, (2007).

39. Shim, J. W., Park, S. J. and Ryu, S. K., Effect of modification with HNO3 and NaOH on metal adsorption by pitch-based activated carbon fibers, *Carbon*, 39 (11), 1635-1642, (2001).

40. Lee, Y. J., Kim, J. H., Kim, J., Lee, D. B., Lee, J. C., Chung, Y. J. and Lim, Y. S., Fabrication of activated carbon fibers from stabilized PAN-based fibers by KOH, *Designing, Processing and Properties of Advanced Engineering Materials, Pts 1 and 2*, 449-4, 217-220, (2004).

41. Li, K., Ling, L., Liu, L., Zhang, B. and Liu, Z., Desulfurization of active carbon fibers activated with ammonia water, *Acta Scientiae Circumstantiae*, 21 (1), 74-78, (2001).

42. Gaur, V., Preparation and characterization of activated carbon fabric for the control of BTX, SO_2 and NO_x emission (Dissertation), Inidian Institute of Technology Kanpur, (2005).

43. Moon, S. Y., Kim, M. S., Hahm, H. S. and Lim, Y. S., Preparation of activated carbon fibers by chemical activation method with hydroxides, *Eco-Materials Processing & Design VII*, 510-511, 750-753, (2006).

44. Qiao, W. M., Yoon, S. H., Korai, Y., Mochida, I., Inoue, S., Sakurai, T. and Shimohara, T., Preparation of activated carbon fibers from polyvinyl chloride, *Carbon*, 42 (7), 1327-1331, (2004).

45. Liu, C. L., Wen, Y. H., Cheng, J., Guo, Q. G., Cao, G. P., Liu, L. and Yang, Y. S., Influence of pore structure of phenolic resin based activated carbon fibers on the electrochemical performance of electrical double-layer capacitors, *Acta Physico-Chimica Sinica*, 21 (7), 786-791, (2005).

46. Suarez-Garcia, F., Martinez-Alonso, A. and Tascon, J. M. D., Beneficial effects of phosphoric acid as an additive in the preparation of activated carbon fibers from Nomex aramid fibers by physical activation, *Fuel Process. Technol.*, 77, 237-244, (2002).

47. Villar-Rodil, S., Suarez-Garcia, F., Paredes, J. I., Martinez-Alonso, A. and Tascon, J. M. D., Activated carbon materials of uniform porosity from polyaramid fibers, *Chem. Mater.*, 17 (24), 5893-5908, (2005).

48. Park, S. J., Kim, K. D. and Lee, J. R., Influence of activation temperature on surface and adsorption properties of PAN-based activated carbon fibers/phenolic resin matrix composites, *Polymer-Korea*, 24 (1), 97-104, (2000).

49. Li, K., Ling, L., Lu, C., Liu, Z., Liu, L. and Mochida, I., Influence of CO-evolving groups on the activity of activated carbon fiber for SO_2 removal, *Fuel Process. Technol.*, 70 (3), 151-158, (2001).

50. Kisamori, S., Kuroda, K., Kawano, S., Mochida, I., Matsumura, Y. and Yoshikawa, M., Oxidative Removal of SO_2 and Recovery of H_2SO_4 over Poly(Acrylonitrile)-Based Active-Carbon Fiber, *Energy & Fuels*, 8 (6), 1337-1340, (1994).

51. Mochida, I., Hirayama, T., Kisamori, S., Kawano, S. and Fujitsu, H., Marked Increase of SO_2 Removal Ability of Poly(Acrylonitrile)-Based Active-Carbon Fiber by Heat-Treatment at Elevated-Temperatures, *Langmuir*, 8 (9), 2290-2294, (1992).

52. Daley, M. A., Mangun, C. L., Debarr, J. A., Riha, S., Lizzio, A. A., Donnals, G. L. and Economy, J., Adsorption of SO_2 onto oxidized and heat-treated activated carbon fibers (ACFS), *Carbon*, 35 (3), 411-417, (1997).

53. Lizzio, A. and Debarr, J., Mechanism of SO_2 removal by carbon, *Energy & Fuels*, 11, 284-291, (1997).

54. Martin-Gullon, I., Jagtoyen, M., Kimber, G. and Derbyshire, F., Activated carbon fibers from PAN. II. Catalytic activity for SO_2 oxidation, The American Carbon Society 1997 Proceedings - 23rd Biennial Conference, The Pennsylvania State University, University Park, PA,(1997).

55. Tseng, H. H., Wey, M. Y. and Fu, C. H., Carbon materials as catalyst supports for SO_2 oxidation: catalytic activity of CuO-AC, *Carbon*, 41 (1), 139-149, (2003).

56. http://en.wikipedia.org/wiki/Incipient_Wetness_Impregnation, Jan 2010 accessed.

57. Lee, Y. W., Kim, H. J., Park, J. W., Choi, B. U., Choi, D. K. and Park, J. W., Adsorption and reaction behavior for the simultaneous adsorption of NO-NO_2 and SO_2 on activated carbon impregnated with KOH, *Carbon*, 41 (10), 1881-1888, (2003).

58. Fortier, H., Zelenietz, C., Dahn, T. R., Westreich, P., Stevens, D. A. and Dahn, J. R., SO_2 adsorption capacity of K_2CO_3-impregnated activated carbon as a function of K_2CO_3 content loaded by soaking and incipient wetness, *Appl. Surf. Sci.*, 253 (6), 3201-3207, (2007).

59. Tseng, H. H. and Wey, M. Y., Study of SO_2 adsorption and thermal regeneration over activated carbon-supported copper oxide catalysts, *Carbon*, 42 (11), 2269-2278, (2004).

60. Davini, P., The effect of certain metallic derivatives on the adsorption of sulphur dioxide on active carbon, *Carbon*, 39 (3), 419-424, (2001).

Chapter 2 Manufacturing of Activated Carbon Fibers via Electrospinning

2.1 Introduction

Electrospinning, a simple approach to make very fine fibers ranging from nano to micro scales, is attracting more attention due to high surface area, high porosity and high surface area to volume ratio of electrospun fibers. These properties make them suitable for manufacturing carbon and graphitic nanofibers, tissue scaffold and drug delivery, filtration and reinforced nanocomposites, etc. Dependence of fiber diameter and electrospun nonwoven structure on polymer viscoelasticity and electrostatic field formed between two electrodes has been reported by many researchers. Although composites filled with nanofibers have shown enhanced mechanical properties with respect to unfilled composites, compared to cast films, electrospun membranes had a reduction in peak tensile strength [1]. However, not much information is available on mechanical properties of electrospun nanofiber nonwoven membranes.

Activated carbon fiber, a relatively new adsorbent, offers wonderful adsorption properties, such as faster adsorption rate, longer life and lower pressure drop, in comparison with traditional granular activated carbons. Therefore, they are widely used in separation of gases, recovery of solvents, removal of organic pollutants from drinking water and catalyst support [2, 3]. Rayon, pitch and PAN fibers are mainly used as

precursors for activated carbon fibers. The advantage of finer fibers to make activated carbon fibers has been studied by Park et al. The electropun ultrafine pitch fibers have faster activation rate constant than melt-spun pitch fibers due to high surface area [4]. Kim et al., activated stabilized electrospun PAN with steam and three different surface areas, namely 850 m^2/g, 1000 m^2/g and 1230 m^2/g were obtained at various activation temperatures [5, 6]. They also tried poly (amic acid) as precursor to make activated carbon nanofibers [7]. These studies mentioned above employed physical activation to create pores in precursor fibers. Compared to physical activation, chemical activation process has important advantages including low heat treatment temperature, short period of time, large surface area and high carbon yield [8]; however, there has been no work reported for chemically activated carbon nanofibers.

In our work, the effects of main electrospinning parameters on resulting nanofiber diameters were studied. Mechanical properties, such as tensile, tear and burst strength of electrospun PAN nonwoven membrane structures were measured and the quantitative relationships between membrane thickness and membrane properties were established. Other physical properties, such as air permeability, pore size and porosity were studied as well. Activated carbon nanofibers were produced from electrospun PAN by chemical activation with potassium hydroxide (KOH) as the activating agent. They were characterized by morphology, Fourier transform infrared (FTIR) spectrum, Brunauer-Emmeet-Teller (BET) surface area, total pore volume and pore size distribution.

2.2 Materials and experimental procedures

Polyacrylonitrile (PAN, M_w=150,000g/mol from Sigma-Aldrich®) was dissolved in N,N-dimethylformamide (DMF) (from Sigma-Aldrich®) and stirred for 24 hours. PAN/DMF solution was stored in BD 10mL syringe and delivered by KD® scientific syringe pump through BD 18G 1½ precision glide needle (outside diameter 1.27 mm+/-0.0127 mm; inner diameter 0.711 mm+/-0.0127 mm). Under the accelerating voltage obtained from Gamma high voltage power supply (0-30 kV DC), polymer jets were stretched by the electrostatic force and columbic force from charged polymer. After the DMF solvent evaporated during stretching, nanofibers were deposited on aluminum foil (the negative electrode) and the electrospun PAN nonwoven membranes were formed.

Activated carbon nanofibers were obtained from electrospun PAN nanofibers with stabilization and activation processes. Electrospun PAN nanofibers were stabilized in air by raising temperature from 20ºC to 280 ºC at 1 ºC /min and holding at 280ºC for 1 hour, which prevented fibers from sticking to each other for further treatment at higher temperature. The stabilized PAN was immersed in KOH (Spectrum®) solution for 12 hours followed by drying up at 85℃. The weight ratio of KOH to stabilized PAN was 1, at which the highest surface area was reported [8]. The stabilized electrospun PAN containing KOH was activated at 800℃ for 40 min under nitrogen atmosphere to generate micropores within fibers. The residual KOH on fibers was neutralized with hydrogen chloride acid (36.5-38% concentration, from J.T. Baker) and the extra HCl was rinsed with distilled water.

Morphology of electrospun PAN nonwoven was observed under Scanning Electron Microscope (SEM, Zeiss® EVO 50) and fiber diameters were measured with SEM built-

in software. The electrospun PAN membranes were cut into 25.4×101.6 mm rectangle for tensile strength tests and into 50.8×76.2 mm for tear strength tests on Instron tester (Model 1122). Burst strength test was carried out on Mullen burst tester (B.F. Perkins & Son. Inc.). Air permeability was measured on Gurley Densometer. Interfiber pore size within membrane was tested with Capillary Flow Porometer (Porous Materials Inc.) using Galwick with the surface tension of 15.9 dynes/cm as the solvent for wet curve. Activated carbon nanofibers were too brittle for these physical property measurements. BET surface area, average pore size and pore volume of electrospun PAN and activated carbon nanofibers were analyzed on Autosorb-1 (Quantachrome® Instruments) using nitrogen as absorbate at 77 K. FTIR (Thermo®) was used for analyzing the structure evolution during stabilization and activation process. Pore size distribution analysis was carried out on AS1 WIN software (Quantachrome® Instruments). Dubinin-Astakhov (DA) equation is good for analyzing activated carbon nanofibers and the generalized Halsey equation is more suitable for determination of micropore volume of electrospun PAN in which mesopores might be present [9] . Both analysis methods were employed for comparison.

2.3 Results and discussion

2.3.1 Influence of electrospinning parameters on fiber diameters

To study the impact of individual electrospinning parameters on fiber diameters, a series of experiments were performed. One parameter was changed as all others were fixed during any specific experiment.

2.3.1.1 Solution concentration. At 20 kV voltage, the needle tip-collector distance was set at 20 cm, the flow rate at 1 mL/h and PAN/DMF solutions with concentrations of 8, 10,

12 and 14 wt% were electrospun. The observed morphology of resultant PAN nanofiber nonwoven is illustrated in Figure 2.1. Fiber diameters vary depending on solution concentrations. The average fiber diameters for 8, 10, 12 and 1 4 wt % were 170 nm, 287 nm, 438 nm and 519 nm, respectively. The relationship between polymer solution concentration and fiber diameters is shown in Figure 2.2. The steady increase of fiber diameter is observed as the solution concentration increases. The increasing solution concentration contributes to increasing molecular entanglement and higher viscoelasticity resulting in difficulty in streching fibers, which leads to thicker fibers. The numerical relation is estimated by the linear equation $y = 59.9x - 305.4$ with an R^2 of 0.9881 as shown in Figure 2.2. The statistical frequency distribution of nanofiber diameters for each concentration is represented in Figure 2.3. Nanofibers spun from 8 wt% PAN/DMF solution have 66.1% of fibers with diameters ranging from 100 nm to 200 nm, which is the biggest frequency among the nanofibers from four different concentrations. Correspondingly, the biggest fraction of nanofiber diameters from 10 wt% is 58.3% which is in the range of 200-300 nm. This number becomes smaller, 52.5% in 400-500 nm range and 47.8% in 500-600 nm range for fibers from 12 and 14 wt% solutions, respectively. Therefore, fibers spun from low concentration have more narrow distribution than those from higher concentration.

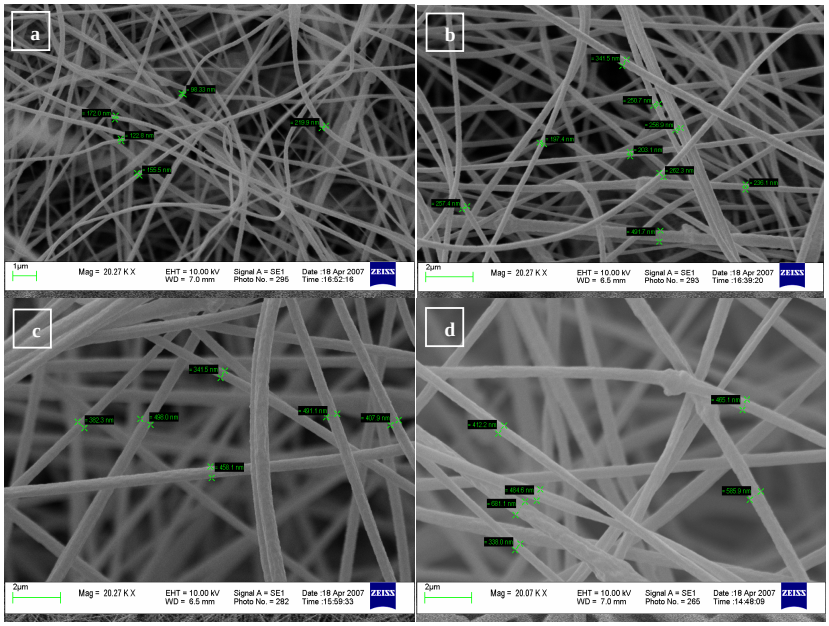

Figure 2.1. SEM images of electrospun PAN from different concentrations (a) 8% (b)10% (c)12% (d)14% (20 kV voltage, 20 cm tip-collector distance and 1 mL/h flow rate).

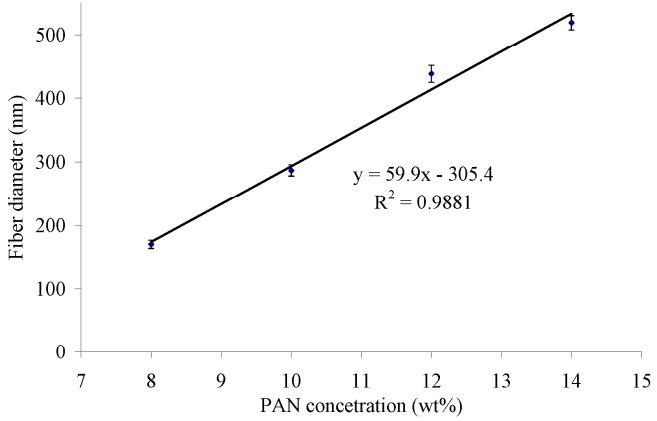

Figure 2.2. Fiber diameters with different PAN concentrations (20 kV voltage, 20 cm distance and 1 mL/h flow rate).

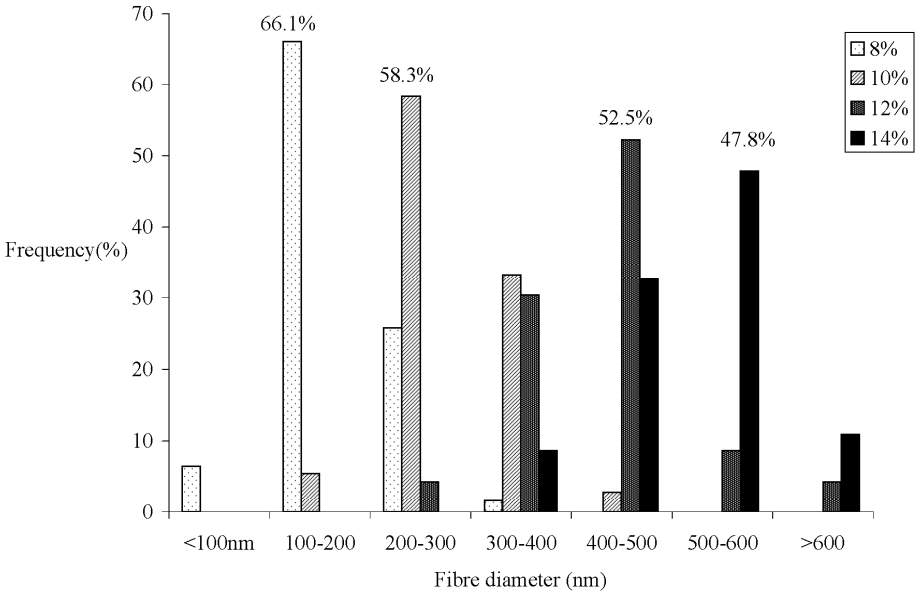

Figure 2.3 The frequency distribution of nanofiber diameters for different solution concentrations.

2.3.1.2 Applied voltage. PAN/DMF solution was electrospun at 5, 10, 15, 20, 24 and 29 kV as solution concentration, flow rate and needle tip-collector distance remained at 10 wt%, 2 mL/h and 20 cm, respectively. The resulting average fiber diameters are plotted as the function of applied voltage as shown in Figure 2.4. The increasing voltage results in thicker fibers and their relation fits the equation $y = 7.0995x + 226.05$ with an R^2 of 0.7805. The biggest diameter difference of 156nm happens between 10 kV (263 nm) and 29 kV (419 nm). Nanofibers are drawn by the electrostatic force between two electrodes.

The increase in applied voltage leads to stronger electrostatic forces and therefore accelerates polymer jet toward target collector which was an aluminum foil. Higher jet speed might not allow fibers to be stretched enough with less traveling time from needle to the collector, resulting in bigger fiber diameter. Similar results were obtained by Yang et al. [10]. The voltages below 5 kV generated too low electrostatic force to overcome solution surface tension and no polymer jet was formed.

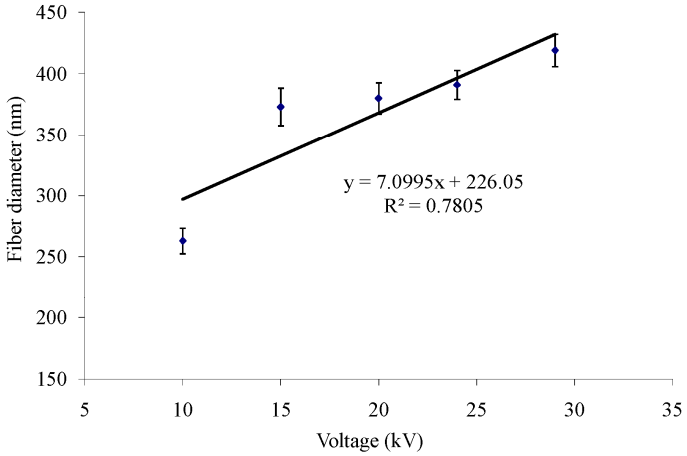

Figure 2.4. Fiber diameters at different voltages (10% PAN/DMF, 20 cm tip-collector distance and 2 mL/h flow rate).

2.3.1.3 Flow rate. To study the influence of flow rate on the electrospun fiber diameters, 10 wt% PAN/DMF was electrospun keeping the needle tip-collector distance at 20 cm and applied voltage at 20 kV. The flow rate was set 0.5, 1, 1.5, 2, 2.5 and 3 mL/h. The resulting fiber diameters are shown in Figure 2.5. No strong relation between flow rate and fiber diameter is observed. Compared to diameter variation caused by PAN/DMF concentration and applied voltage, the difference between the thickest and the thinnest fiber caused by varying flow rate is smaller, only 82 nm. Thus it can be concluded that

flow rate has less influence than polymer concentration and applied voltage on fiber diameter.

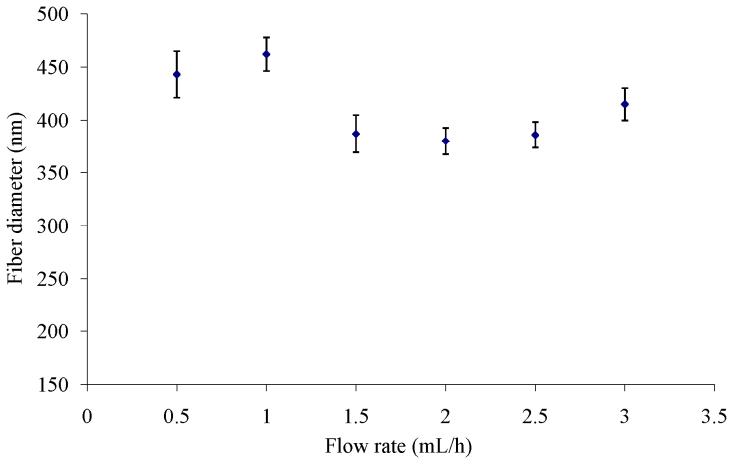

Figure 2.5. Fiber diameters at different flow rates
(10% PAN/DMF, 20 cm distance and 20 kV voltage).

2.3.1.4 Needle tip-collector distance. The increase of needle tip-collector distance is considered to decrease the electrostatic force between the collector and the needle and therefore the thicker fibers are expected. However, longer distance provides more time for stretching resulting in smaller fiber diameters which may balance the impact of electrostatic force. In the experiment, when the distance was raised from 10 cm to 30 cm, randomly scattered fiber diameters were observed as shown in Figure 2.6. The finest fiber of 366 nm was obtained when the distance was set at 24 cm while the thickest fiber of 401 nm was at 15 cm. Other fibers diameters vary between them. It is interesting to note that the trend of the data points on Figures 2.5 and 2.6 are somewhat similar.

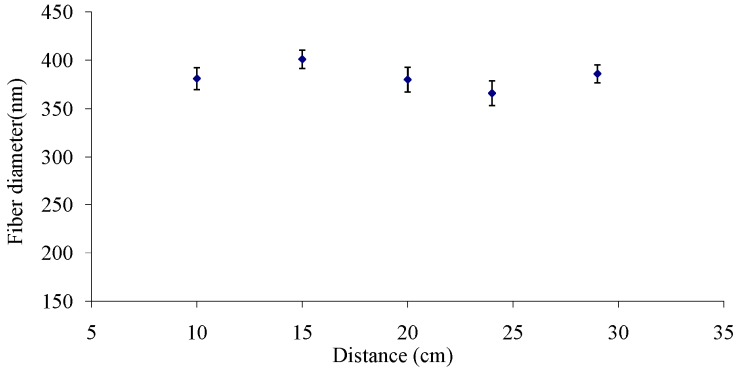

Figure 2.6. Fiber diameters at different needle-tip distances (10% PAN/DMF, 20 kV voltage and 2 mL/h flow rate).

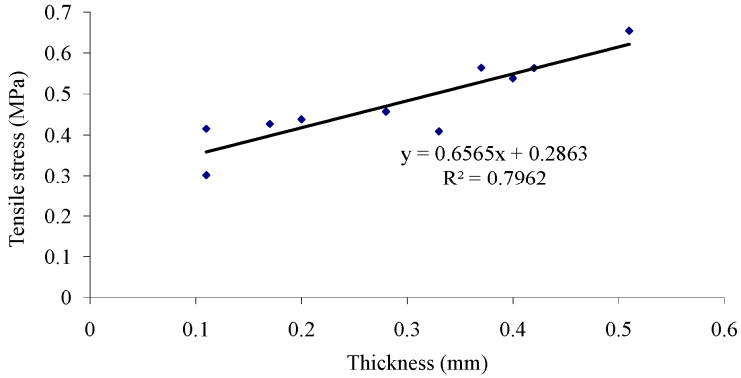

Figure 2.7. Variation of tensile strength with the change of electrospun PAN membrane thickness.

2.3.2 Physical and mechanical properties of electrospun PAN membranes

Generally, the increase of thickness causes an increment of strength with the loss of air permeability as the penalty. In this part, experiments were designed to investigate the numerical relation between strength (tensile, tear and burst) and electrospun PAN membrane thickness. All membranes in this part were electrospun from 10 wt% PAN/DMF at 20 kV/ 20cm with a delivery rate of 1 mL/h.

2.3.2.1 Tensile, tear and burst strength. The variations of tensile, tear and burst strength with the increase of thickness of electrospun PAN are shown in Figures 2.7, 2.8 and 2.9. As expected, the thicker the membrane, the higher the tensile and tear strength. Tensile-thickness relation fits the linear equation $y = 0.6565x + 0.2863$ with an R^2 of 0.7962 and tear-thickness relation fits the equation $y = 81.106x + 3.6858$ with an R^2 of 0.9602. In tensile strength test, the membranes with different thickness exhibited different breaking behaviour. Thinner membranes had a uniform fracture, which was mostly due to breakage of individual fibers simultaneously while the thicker membranes had transverse contraction. When the load was applied to a thick membrane, it deformed in order to align fibers in the stretching direction and then fiber slippage took place after overcoming the friction due to fiber entanglement [11].

Figure 2.9 shows the burst strength of membranes at various thicknesses. For the membranes with the thickness of 0.34 mm or higher, burst strength varies between 0.096 and 0.102 Pa which was not a big change. The relation between the thickness and burst strength of membranes could be best expressed by the equation $y = 0.105x^{0.1126}$ with an R^2 of 0.7705. For comparison, the burst strength of 1mm thick regular print paper was measured as 0.11 Pa, which was higher than electrospun PAN membrane by 7.8%.

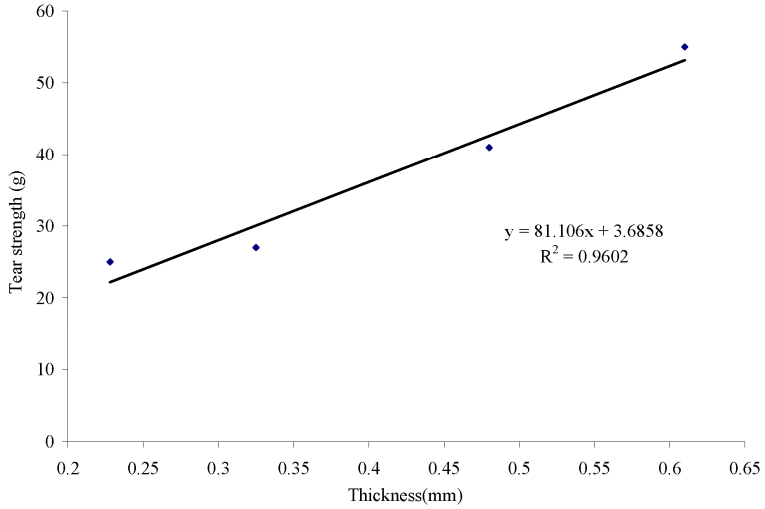

Figure 2.8. Variation of tear strength with the change of membrane thickness.

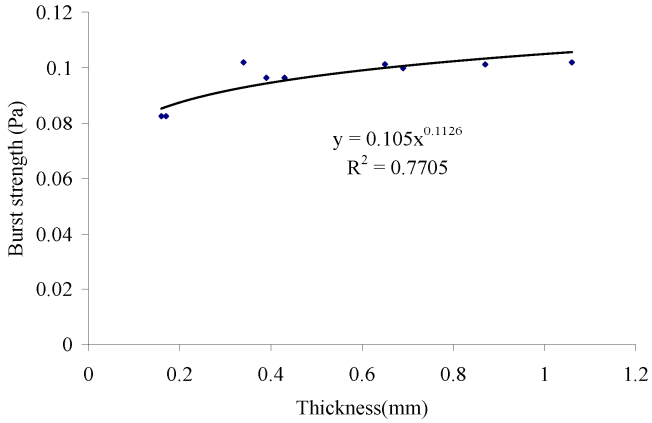

Figure 2.9. Variation of burst strength with the change of membrane thickness.

2.3.2.2 Air Permeability. Gain of strength with the increasing thickness of membrane accompanies the loss of air permeability. As shown in Figure 2.10, the increase of thickness results in an exponential decrease in air permeability that could be represented by the equation $y = 9.5551x^{-0.9245}$ with an R^2 of 0.9792.

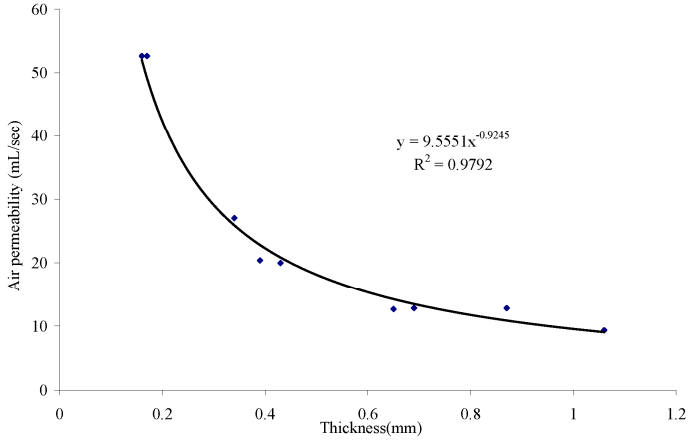

Figure 2.10. Air permeability as a function of membrane thickness.

2.3.2.3 Porosity and pore size. Porosity of a membrane is calculated as,

$$\mu = (1 - \frac{V_F}{V_t}) \times 100\% = (1 - \frac{m/\rho}{t \times A}) \times 100\% \quad (2.1)$$

where μ is calculated porosity, V_F is the fiber volume in the membrane, V_t is the membrane total volume, m is the weight, ρ is PAN density (1.17 g/cm^3), t is the membrane thickness and A is the membrane area [11]. The porosity and interfiber pore size within electrospun PAN nonwoven made from various solution concentrations are summarized in Table 2.1. As discussed above, different solution concentrations result in different fiber diameters if all other electrospinning parameters are fixed. Since the applied voltage, flow rate and tip-collector distance are all fixed, higher solution concentration represents thicker fibers. Regardless of nanofiber diameters, the porosity of the electrospun membrane did not show much variation. The electrospun PAN nonwoven with small pore size ranging from 0.801 to 1.3548 μm could catch very small particles. The high porosity and small interfiber pore size of electrospun membranes

make them a good candidate for tissue scaffold by providing enough space for cell accommodation and an easy passage for nutrient intake and metabolic waste exchange [1, 12].

Table2.1 Physical properties of electrospun PAN membrane and stabilized PAN membrane.

Concentration (wt%)	8	10	12	14
Interfiber pore size (μm)	0.801	1.0245	0.8727	1.3547
Porosity (%)	96.12	96.75	96.34	95.89
Porosity after stabilization (%)	96	96.05	96.7	96.19

2.3.2.4 Physical properties of stabilized PAN nanofiber membrane. Electrospun PAN membrane made from 8, 10, 12 and 14 wt% PAN/DMF solutions were stabilized at 280ºC for 1 hour. The stabilized PAN showed different breaking behaviour from the electrospun PAN without stabilization as shown in Figure 2.11. For stabilized PAN made from 8 and 10 wt% solutions, tensile strength showed an obvious reduction with the increase in thickness. However, stabilized PAN from the other two solutions did not show strong relation between thickness and tensile strength. More uniform breaking fracture was observed on the stabilized electrospun PAN membranes than those before stabilization.

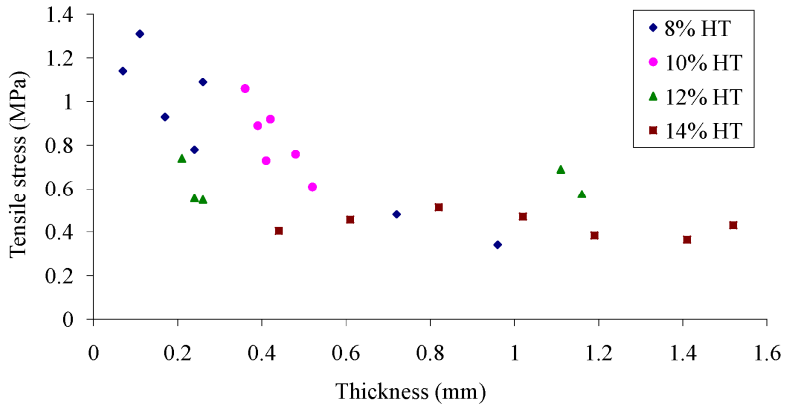

Figure 2.11. Tensile strength variations of stabilized electrospun PAN with the increase in thickness (20 kV voltage, 20 cm distance and 1.5 mL/h flow rate).

Porosity of stabilized electrospun PAN nanofibers was compared with those without stabilization as shown in Table 2.1. Although some shrinkage was observed after stabilization at 280 ºC, it did not show significant influence on the porosity of membrane. The stabilized PAN nanofibers were too brittle to carry out the pore size test on porometer.

2.3.3 Properties of electrospun PAN based activated carbon nanofibers

Since the thinnest nanofibers were made from 8 wt% PAN/DMF solution based on the study above, they were used as precursors to make activated carbon nanofibers.

2.3.3.1 Morphology. The structures of electrospun PAN and activated PAN nanofibers are shown in Figure 2.12. A denser looking structure was obtained after activation, which was probably due to shrinkage and crimping of fibers resulting from the cyclization during stabilization and activation. The average nanofiber diameter decreased slightly from 287 nm before activation to 270 nm afterward.

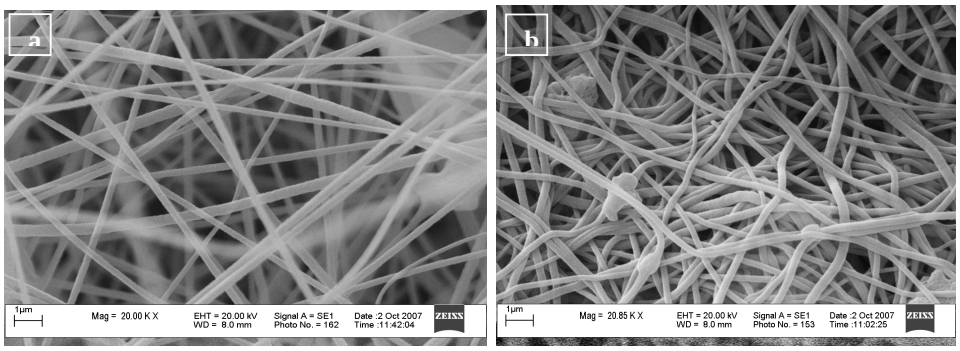

Figure 2.12. SEM images of (a) electrospun PAN membrane and (b) activated carbon nanofibers (8 wt% PAN/DMF, 20 kV voltage, 20 cm distance and 1mL/h flow rate).

2.3.3.2 FTIR spectrum. Figure 2.13 shows the FTIR spectrum of electrospun PAN, stabilized PAN and activated PAN (activated carbon nanofibers). The remarkable change during the conversion is the decrease of CN triple bond. The FTIR spectrum for electrospun PAN has the peak at the wavenumber of 2242 cm^{-1} to represent CN triple bond in the PAN (Figure 2.13a). In the stabilization process, the CN triple bond was converted to CN double bond and the cycle including carbon and nitrogen atoms was formed so that the peak of CN triple bond became very small. In the spectrum for activated PAN shown in Figure 2.13(c), CN triple bond disappeared and no CH or CH_2 bond at 2936 cm^{-1} was obtained. During activation process at high temperature, most of non-carbon atoms, such as nitrogen and hydrogen, were removed and micropores grew at the same time.

2.3.3.3 Pore structure of activated carbon nanofiber. BET surface area, average pore diameter, total pore volume and DA micropore volume of electrospun PAN and activated carbon nanofibers are compared in Table 2.2. The surface area of activated carbon nanofiber is 27.2 times larger than that of electrospun PAN nanofibers before activation.

The activated carbon nanofibers have 0.59 cc/g micropore volume, which is 14.75 times larger than that of 0.04 cc/g before activation. Compared to conventional fibers with diameters in the scale of micron or bigger, electrospun PAN has relatively high surface area of 34.4 m^2/g due to very small fiber diameter in nano scale. However, activation process created micropores and mesopores within fibers, which contributes to the dramatic increase in surface area that is one of the dominant factors to determine adsorption capacity of adsorbents.

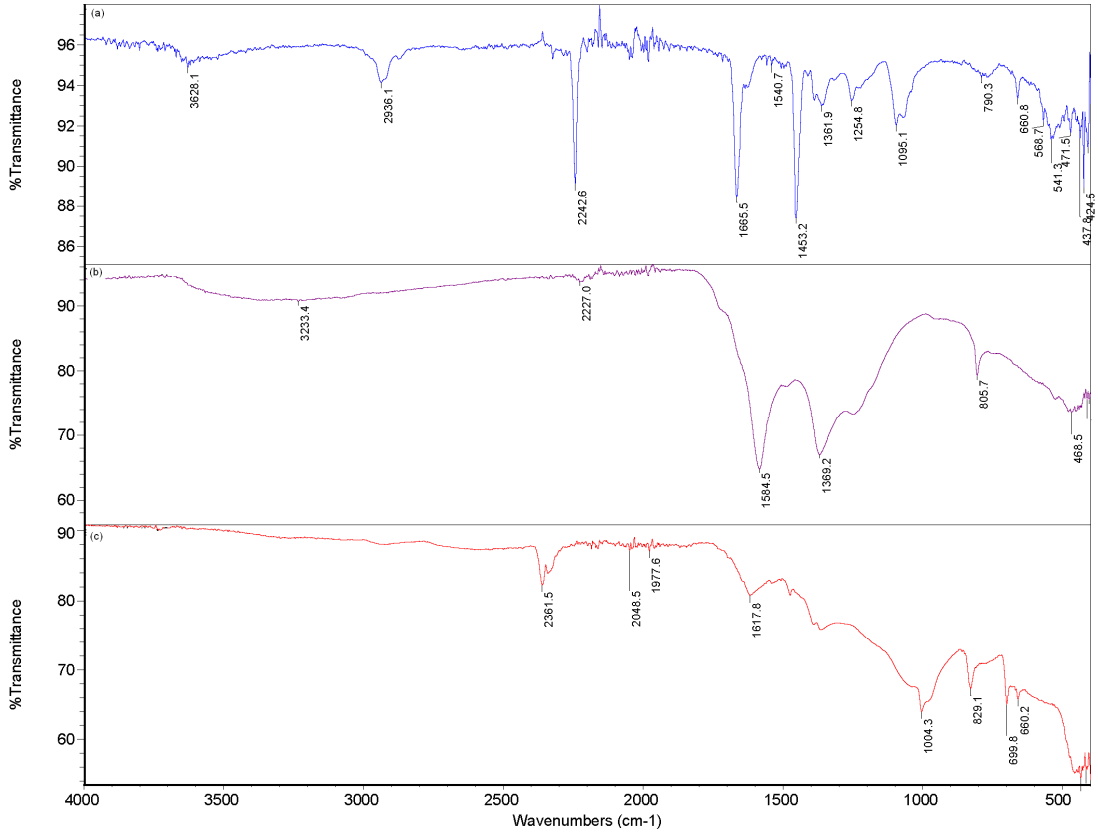

Figure 2.13. FTIR spectrum for (a) electrospun PAN, (b) stabilized PAN and (c) activated carbon nanofibers.

Pore size distribution was analyzed based on the DA equation and the generalized Halsey equation. In the DA pore size distribution curve presented in Figure 2.14, activated carbon nanofiber has a high peak between 1nm and 4nm pore diameter while electrospun PAN before activation has a small peak, which indicates that activated carbon nanofibers contain much more micropores than electrospun PAN. Based on the generalized Halsey method, the pore volume is plotted as the function of Halsey statistical thickness, as shown in Figure 2.15. The electrospun PAN line can be extrapolated to the y axis close to the origin, which is the evidence of small amount of micropores; the V-t plot of activated carbon nanofibers has a large positive intercept on Y axis (312.73), which means they contain a big amount of micropores [9]. Micropores and mesopores with an average pore diameter of 3nm could trap small molecules so that it could be used for water purification, gas separation and chemical protection.

Table 2.2. Pore structures of electrospun PAN and activated carbon nanofibers.

	Surface area (m^2/g)	Average pore diameter (Å)	Total pore volume (cc/g)	DA micropore volume (cc/g)
Electrospun PAN	34.4	147	0.127	0.04
Activated carbon nanofibers	936.2	30	0.723	0.59

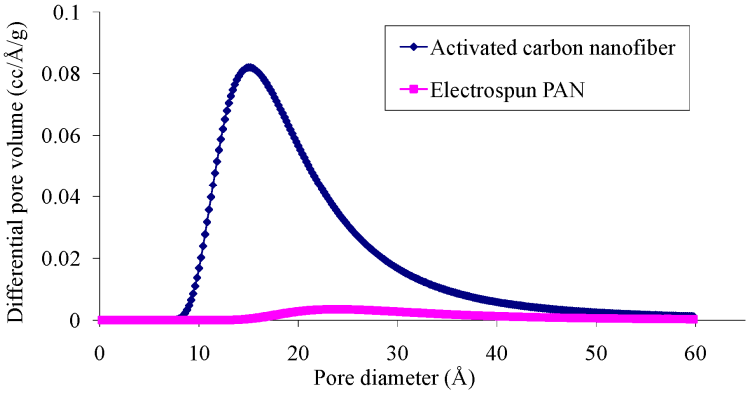

Figure 2.14 DA pore size distribution

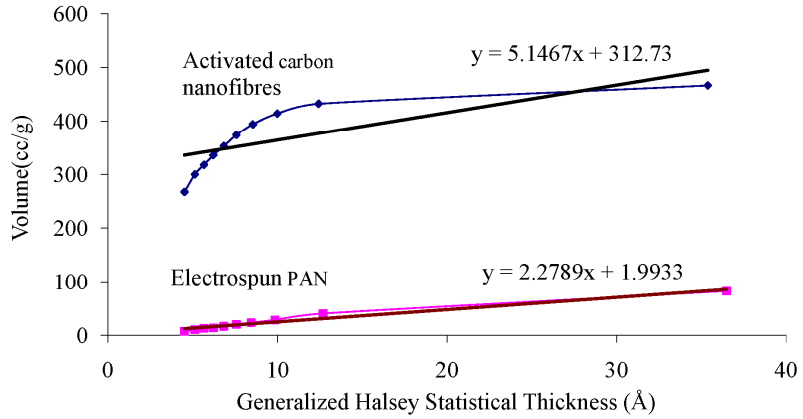

Figure 2.15 Generalized Halsey V-t plot

2.4 Conclusions

Electrospun polyacrylonitrile fiber diameters were mainly determined by the solution concentration and applied voltage rather than flow rate and needle tip-collector distance. Tensile and tear strengths increased with increasing thickness of the electrospun PAN membrane, which was accompanied by a decrease of air permeability. Burst strength was

not affected much by thickness when the membrane is 0.34 mm or thicker. After stabilization, tensile strength of electrospun nanofiber membranes made from 8 and 10 wt% solution decreased with increasing thickness. Electrospun PAN had a very high porosity, which was not affected by the solution concentration and stabilization process. Electrospun polyacrylonitrile nanofibers were chemically activated to obtain activated carbon nanofibers using KOH as the activating agent. The disappearance of CN triple bond in the FTIR spectrum for the activated carbon nanofibers and a dramatically increased surface area and micropore volume after activation proved the successful conversion from PAN to activated carbon nanofibers. In V-t plot based on the generalized Halsey equation, activated carbon nanofiber line has a large positive intercept reflecting the presence of a large amount of micropores; however, the intercept for electrospun PAN line is very small reflecting small micropore volume. The same result is concluded from the DA pore size distribution analysis. Most of the generated pores in activated carbon nanofibers are micropores and mesopores with an average pore diameter of 3 nm.

References

1. Subbiah, T., Bhat, G. S., Tock, R. W., Pararneswaran, S. and Ramkumar, S. S., Electrospinning of nanofibers, *Journal of Applied Polymer Science*, 96 (2), 557-569, (2005).
2. Lawrence L, W., Norman C. Pereira, Yang-Tse Hung, *Air Pollustion Control Engineering*, Humana Press, Totowa, NJ, (2004).

3. Moon, S. Y. K., M.; Hahm, H.; Lim, Y., Preparation of Activated Carbon Fibres by Chemical Activation Method with Hydroxides, *Materials Science Forum*, 510-511, (2006).

4. Park, S. H., Kim, C., Jeong, Y. I., Lim, D. Y., Lee, Y. E. and Yang, K. S., Activation behaviors of isotropic pitch-based carbon fibers from electrospinning and meltspinning, *Synthetic Metals*, 146 (2), 207-212, (2004).

5. Kim, C. and Yang, K. S., Electrochemical properties of carbon nanofiber web as an electrode for supercapacitor prepared by electrospinning, *Applied Physics Letters*, 83 (6), 1216-1218, (2003).

6. Kim, C., Yang, K. S. and Lee, W. J., The use of carbon nanofiber electrodes prepared by electrospinning for electrochemical supercapacitors, *Electrochemical and Solid State Letters*, 7 (11), A397-A399, (2004).

7. Kim, C., Choi, Y. O., Lee, W. J. and Yang, K. S., Supercapacitor performances of activated carbon fiber webs prepared by electrospinning of PMDA-ODA poly(amic acid) solutions, *Electrochimica Acta*, 50 (2-3), 883-887, (2004).

8. Lee, Y. J., Kim, J. H., Kim, J., Lee, D. B., Lee, J. C., Chung, Y. J. and Lim, Y. S., Fabrication of activated carbon fibers from stabilized PAN-based fibers by KOH, *Designing, Processing and Properties of Advanced Engineering Materials, Pts 1 and 2*, 449-4, 217-220, (2004).

9. AS1 win Version 1.51, Operating Manual, (2005).

10. Yang, Y., Jia, Z. D., Li, Q. and Guan, Z. C., Experimental investigation of the governing parameters in the electrospinning of polyethylene oxide solution, *IEEE Transactions on Dielectrics and Electrical Insulation*, 13 (3), 580-585, (2006).

11. Wang, Y., A method for tensile test of geotextile with confining pressure, *Journal of Industrial Textiles*, 30 (4), 289-302, (2001).

12. Thorvaldsson, A., Stenhamre, H., Gatenholm, P. and Walkenstrom, P., Electrospinning of highly porous scaffolds for cartilage regeneration, *Biomacromolecules*, 9 (3), 1044-1049, (2008).

Chapter 3 Sulfur Dioxide Removal over Activated Carbon Fibers and Modified Activated Carbon Fibers

Activated carbon fibers (ACFs) have been considered as one of the most promising sorbents for gas and liquid purification, such as water purification, flue gas desulfurization and denitrification, and removal of volatile organic compounds. As for desulfurization, their ability to absorb sulfur dioxide was discussed in Chapter 1.

In this work, activated carbon fibers manufactured from various raw materials are studied and their pore structures and sulfur dioxide removal performance under dry and humid conditions are investigated. Furthermore, they are modified by various promoters with the purpose of improving capability of desulfurization; the corresponding sulfur dioxide removal efficiencies are studied.

3.1 Experimental

3.1.1 Materials

Five types of activated carbon fibers are studied in this research, namely ACF10, ACF15, ACF20, CR and SY. They are classified based on the precursors. ACF10, ACF15 and ACF20 were made from Kynol^{TM} novoloid fibers by American Kynol Inc. Novoloid fibers, whose structure is shown in Figure 3.1, containing 75.8% carbon are transformed to 95% carbon (Figure 3.2) at 700ºC followed by activation with activating agents, such as CO_2 or steam [1]. ACF10, ACF15 and ACF20 are differentiated by distinct surface areas, pore sizes and pore volumes due to the extent of activation. CR (purchased from

Carbon Resources, Inc.) is rayon-based ACFs in the form of felt. SY is rayon-based ACFs provided by Senyou Carbon Fiber Co., Ltd (China). For the purpose of comparison, powdered activated carbon is studied in parallel. Activated carbon powder (60~140 mesh) is manufactured from coconut shell by PICA Inc.

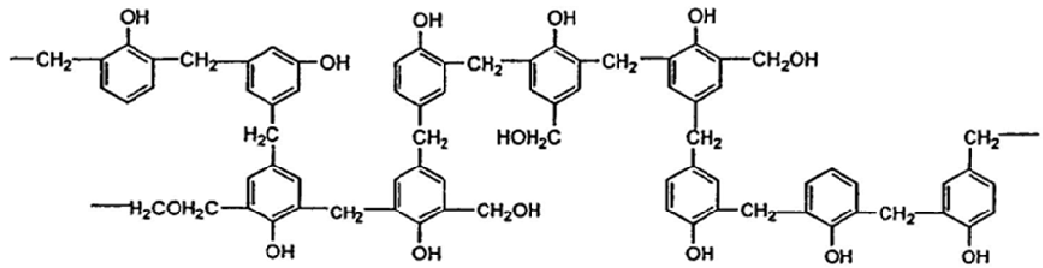

Figure 3.1 Structure of Kynol^{TM} novoloid fibers [1]

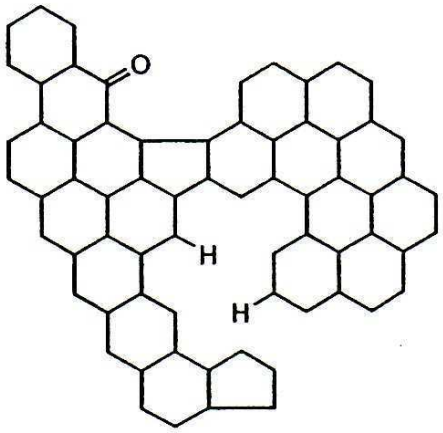

Figure 3.2 Structure of carbonized novoloid fiber with 95% carbon [1]

ACFs were treated with different promoters to improve their capability in desulfurization. Promoters, potassium hydroxide (KOH), potassium carbonate (K_2CO_3), potassium chlorate ($KClO_3$) and potassium permanganate ($KMnO_4$) were dissolved in water with certain concentrations and two methods were used for treatment. Incipient wetness impregnation (IWI) was used first. The volume of solutions which were injected

to ACFs was equal to the pore volume in ACFs. ACFs were also simply immersed in solutions so that a variety of promoter loads could be achieved. Drying at 120ºC followed to remove extra water. In order to prepare metal/ACFs, a certain amount of solution, based on the incipient wetness impregnation, was injected onto ACFs, followed by drying in air and calcinations at high temperature either in nitrogen or air depending on metal precursors. The detailed modification process is further explained in Section 3.1.4.

3.1.2 Pore structure and element analysis

Pore characteristics of activated carbon fibers, such as BET surface area, average pore size and pore volume, were analyzed based on isotherm obtained on Autosorb-1 (Quantachrome® Instruments) using nitrogen as adsorbate at 77 K. For BET surface area analysis, multipoints with a partial pressure (P/P_0) between 0.05 and 0.3 are considered to be accurate in predicting an adsorption process. The number of adsorption sites was estimated based on the BET testing results using equation 3.1.

$$N_{ad} = \frac{W_m}{M} * N = \frac{S_t}{A_{cs}} \quad (3.1)$$

where N_{ad} is the number of adsorption sites, W_m is the sample weight in gram, M is the molecular weight of the adsorbate (nitrogen) in g/mol, N is the Avogadro's number (6.023×10^{23} molecules per mol), S_t is the specific surface area (m^2/g), and A_{cs} is the cross-sectional area of the adsorbate (16.2 $Å^2$ for nitrogen).

Element analysis for nitrogen, carbon and sulfur was conducted on Vario Macro Elementar by analyzing the released carbon dioxide, nitrogen oxide and sulfur oxide during burning of raw materials. Other elements were analyzed on VARIAN Vista-MPX CCD simultaneous ICP-OES. Both of them were performed in the Soil Testing Laboratory at Auburn University.

3.1.3 Sulfur dioxide adsorption testing

Dynamic sulfur dioxide adsorption characteristics over ACFs and PAC were studied by analyzing the breakthrough curves which were obtained through adsorption tests performed in a fixed tubular column reactor (15.9 mm in diameter) made of glass. The experimental test bench was designed based on the ASTM D6646-01 and is shown in Figure 3.3.

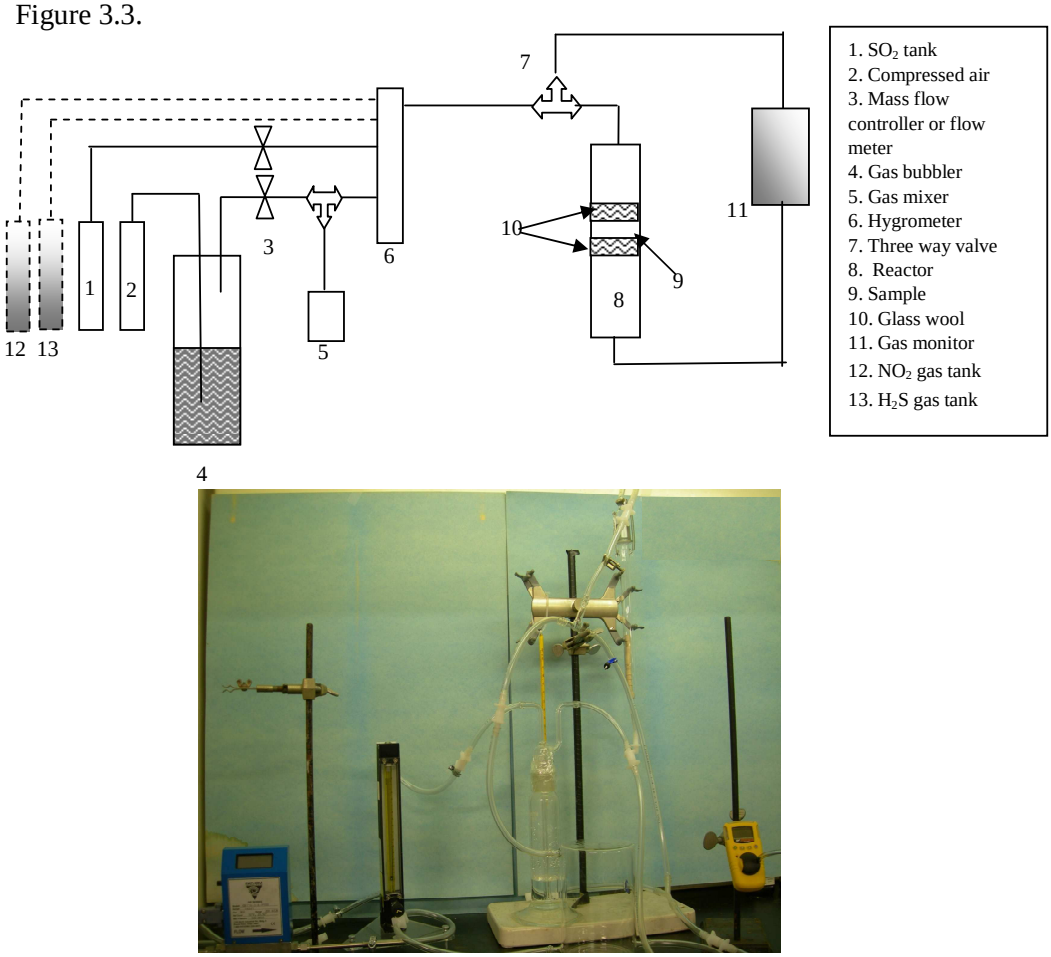

Figure 3.3 Schematic (top) and picture (bottom) of SO_2 adsorption test bench

High concentration sulfur dioxide (2000 ppmv) purchased from Airgas was diluted by air such that a certain concentration of sulfur dioxide could be obtained for adsorption

tests. Before mixing with sulfur dioxide, compressed air can pass through the gas bubble filled with water to be humidified. The relative humidity was monitored with RH 390 Precision Psychrometer (Extech Instruments). In order to obtain a desired relative humidity which determines the water concentration in the main gas stream, air with high humidity was mixed with dry air.

The challenge gas for adsorption tests (one of the mixtures of SO_2+N_2, SO_2+air, SO_2+H_2O+N_2 or SO_2+H_2O+air) was fed into the glass reactor where the adsorbent sample was supported by glass wool and SO_2 adsorption would occur. Before starting the adsorption test, the initial sulfur dioxide concentration was monitored and recorded on a sulfur dioxide single gas detector (BW Gasalert Extrem). As the experiment started, the transient concentration of sulfur dioxide leaking from the reactor was measured. The simultaneous removal of nitrogen dioxide and hydrogen sulfide over adsorbents can be performed on the same set up by adding gas tanks. Breakthrough times and breakthrough curves were obtained during each test and the corresponding sulfur dioxide capacities were calculated. The time from the beginning of the test until SO_2 can be detected at the exit of the reactor is called the breakthrough time or breakthrough period, beyond which the desulfurization efficiency starts decreasing. The breakthrough curve or breakthrough profile, which is the transient response of the adsorbent bed to adsorbates, is a reflection of the adsorbents performance under dynamic conditions. A relatively larger breakthrough time and gradual increase in the concentration following breakthrough are desirable [2]. In order to study the effect of oxygen on SO_2 adsorption, air was replaced by nitrogen. The utilization of samples refers to the ratio of breakthrough time to saturation time.

3.1.4 Modification of activated carbon fibers

3.1.4.1 ACFs supported metals In the literature, copper, nickel and iron have been reported to be better than other promoters for activated carbon and activated carbon fibers in enhancing sulfur dioxide removal efficiency [3-8]. In this study, they were supported by ACF20 and their sulfur dioxide capacities were measured and compared with each other and with bare ACF20 to investigate their potential to be good desulfurizer. For Cu/ACF20 and Ni/ACF20, the metal precursors are copper nitrate with trihydrate ($Cu(NO_3)_2 \cdot 3H_2O$) and nickel nitrate with hexahydrate ($Ni(NO_3)_2 \cdot 6H_2O$), respectively.

Before the treatment, ACF20s were dried at 110ºC. Cu/ACF20 and Ni/ACF20 were prepared with the incipient wetness impregnation with metal loads of 5 wt%. Since the total pore volume of ACF20 was 1.46 cc/g, there was 2.92 mL pore volume available for the solutions. However, a little more solution was used to account the loss of solution induced by the operation. Thus, 3.2 mL 12.9 wt% copper nitrate and 16.96 wt% nickel nitrate solutions were injected to 2 g ACF20 with syringe following 110ºC drying for 6 hours for the designed 5 wt% load of metal. $Cu(NO_3)_2$/ACF20 and $Ni(NO_3)_2$/ACF20 were calcined at 300ºC for 1 hour. The ratio of iron to ACF20 was 3.5 wt% since this ratio was found to give the maximum sulfur dioxide capacity in the literature. The precursor of iron was $Fe(NO_3)_3 \cdot 9H_2O$, which was made to 17.34 wt% solution. The same amount of iron nitrate solution (3.2 mL) was injected to 2 g ACF20 following drying at 110ºC and calcinations at 250ºC for 3 hours in nitrogen.

Unlike the incipient wetness impregnation, ACF20 was impregnated in both 12.9 wt% and 2 wt% $Cu(NO_3)_2$ solutions followed by washing, drying and 1 hour calcination at 300°C in nitrogen such that different weight ratios of copper on ACFs could be obtained.

The washing process was expected to clean extra $Cu(NO_3)_2$ which was not trapped in the pores. Pretreatments of ACF20 with HCl and HNO_3 were also employed, respectively, before loading copper to investigate their influences. ACF20s were immersed in 36.8% HCl and HNO_3 at 25°C, respectively, and then were washed with distilled water until the pH value of water reached 7 followed by drying at 110°C.

3.1.4.2 ACFs impregnated with oxidants Sulfur dioxide has the potential to be oxidized by stronger oxidants except oxygen. If oxidants are treated onto fiber surfaces, they are expected to oxide sulfur dioxide and thus clean it from the main gas stream. In the current research, potassium chlorate and potassium permanganate were treated onto porous activated carbon fibers through IWI (incipient wetness impregnation) and impregnation with a variety of oxidant loads. Their effects on sulfur dioxide removal efficiency of ACFs were analyzed. A certain amount of potassium chlorate and potassium permanganate solutions was ejected to activated carbon fibers followed by drying. In theory, if IWI was used, the maximum load of $KMnO_4$ on ACF10, ACF15 and ACF20 would be 2.9, 5 and 8 wt%, respectively, since $KMnO_4/H_2O$ solution gets saturated at 6 wt% at 20°C. Since the total pore volumes of ACF10, ACF15 and ACF20 were 0.51, 0.88 and 1.46 mL/g, respectively, 1, 1.8 and 3 mL 6 wt% KMnO4 solutions were sprayed onto them, respectively, followed by drying at 110°C and 2.01, 5.54 and 7.24 wt% of $KMnO_4$ were obtained on ACF10, ACF15 and ACF20, respectively. The $KMnO_4$ and $KClO_3$ solutions were increased gradually such that a series of weight loads of promoters over ACFs were obtained. This process avoided the high temperature calcination in inert gases (usually nitrogen is chosen) which is energy consuming. Considering wet-laying method for formation of filter media where ACFs are exposed to a large amount of water,

$KClO_3$/ACFs or $KMnO_4$/ACFs needed to be washed with distilled water. The effect of washing on the sulfur dioxide capacity was investigated.

3. 1.5 ACFs surface morphology analysis

Surface characteristics of bare ACFs, modified ACFs prior to and after SO_2 adsorption were observed on scanning electron microscope (SEM, Zeiss® EVO 50 or JEOL 7000 FESEM). Diameters of ACFs were measured on SEM. In order to elucidate pores on fiber surfaces, Matlab® was used to simulate SEM images and show micropores. Diameters of PAC were measured on Spencer optical microscope made by American Optical Company.

3.1.6 Thermogravimetric analysis (TGA)

The thermal stability of bare ACFs, modified ACFs and ACFs saturated with sulfur dioxide were analyzed using TGA (TA instruments) which can help to identify compounds on fiber surfaces.

3.1.7 X-Ray diffraction analysis

For species identification on fiber surfaces, X-Ray diffraction (XRD) was carried out on X-ray diffractometer (D8 Discover manufactured by Bruker-axs). Samples were supported by a glass slide which was put on the platform of the machine. The scanning was performed with a scan rate of 0.01°/s and 2θ for 5° to 90° at 40 kV and 25 mA.

3.1.8 Manufacturing of activated carbon fiber paper (ACFP)

In comparison with particular adsorbents, ACFs offer advantages in formation of a mat with the wet lay technology in two aspects: formation and retention. The density difference between the fibers and other stock components causes an imbalance in formation with respect to dispersion of polymeric fibers across the wet lay mat and thus

additives are usually used to provide even dispersion in the stock to help formation. In our research, the density difference between ACFs and binder fibers is less in comparison with that between metal fibers and adsorbents. Retention is usually a problem if particular adsorbents are employed since the loss of particulates would increase the cost; therefore, additives are included to help entrap particles. The usage of ACFs as adsorbents replacing the particulates addresses the problem of retention. Although ACFs may be broken during preparation of paper slurry, they still keep the length of 1~3 mm and are more likely to form well-dispersed slurry.

For the application of ACFP in filtration, strong, uniform and high contaminant removal efficiency is desired. Physical entanglement along with hydrogen bonding between fibers in regular paper made from cellulose fibers offers the major force that binds fibers together. After formation of paper, extra water needs to be removed to decrease the distance between fibers to form hydrogen bonding which only occur while hydrogen and oxygen atoms are close enough. The subsequent pressing and drying can achieve this goal. Due to the lack of hydrogen and oxygen in ACFs, it is impossible to form a strong ACFP by hydrogen bonding. Therefore, in the current research, cellulose fibers acting as binding agents were mixed with ACF20. Other binders, for example, polyester and bicomponent polyester (CoPET), which would provide bonding by melting, were tried as well in order to optimize the physical and mechanical performance of ACFP, such as tensile strength and uniformity. To determine the fusing temperature for bonding formation in ACFP, melting points of these bonding agents were tested on a differential scanning calorimeter (DSC TA instrument).

To make ACFP with the wet-laying process, ACFs were mixed with bonding agents in 1000 mL water in a blender for 1min to make ACF slurry; then ACFP was formed in a hand sheet former. The hand sheet former consists of a metal column (15 cm in diameter) called headbox, a forming fabric or wire mesh and a drainage system. After the stock suspension was poured into the headbox, ACFs and bonding agents were dispersed thoroughly using a hand held mixer, called a dasher, followed by draining by gravitational forces. A wet mat was formed on the forming fabric followed by pressing twice with the same pressure (560 KPa) for 5 min and 2 min, respectively. The relatively dry wet mat was transferred to a metal plate and covered with another plate to provide 160 Pa pressure during drying/fusing, which completed the bonding between fibers in ACFP.

In order to increase the uniformity of ACFP, a surfactant was added into the slurry to help disperse ACFs and binder fibers. The strength of ACFP was expected to enhance accordingly due to improvement of uniformity. The compositions of ACFP are listed in Table 3.1.

Table 3.1 Compositions of activated carbon fiber papers

Sample	Composition
A	Cellulose/ACF20=50/50 no heating
B	Cellulose/ACF20=30/70 no heating
C	Cellulose/CoPET/ACF20=15/15/70 135°C
D	Cellulose/CoPET/ACF20=15/15/70 165°C
E	Cellulose/CoPET/ACF20=15/15/70 200°C
F	CoPET/ACF20=30/70 122°C
G	CoPET/ACF20=30/70 132°C
H	CoPET/ACF20=30/70 139°C
I	CoPET/ACF20=30/70 180°C
G	CoPET/ACF20=30/70 200°C
K	CoPET/ACF20=30/70 220°C
L	CoPET/ACF20=30/70 260°C
M	CoPET/ACF20=30/70 200°C + 2 drops of surfactant

It should be noted that CR is in the form of felt and therefore does not need to be made into paper. However, CR felt is too weak to be used in the filtration application due to short ACF fibers which cannot provide strong interaction. They may be mixed with binder fibers to enhance their strength. Most ACFP involved in this dissertation are made from individual ACFs rather than from ACF felt.

3.2 Results and Discussion

3.2.1. Pore structure and surface morphology of ACFs

According to International Union of Pure and Applied Chemistry (IUPAC), pores are classified into three categories, namely micropore, mesopore, and macropore with pore sizes less than 2 nm, between 2 and 50 nm, and larger than 50 nm, respectively. Surface area, total pore volume, average pore diameter and micropore diameter (calculated according to Dubinin-Astakhov equation) of ACFs and ACP are summarized in Table 3.2. On the Autosorb-1, surface area was estimated based on Brunauer-Emmett-Teller (BET) equation by assuming that a monolayer of nitrogen molecules covers the adsorbent surfaces. The total pore volume was derived from the amount of vapor adsorbed at a relative pressure close to unity, by assuming the pores are filled with liquid adsorbates. The average pore diameter was evaluated from the total pore volume. To characterize micropores, the Dubinin-Astakhov (DA) equation is more appropriate for strongly activated carbon [9-11], which is used in this research:

$$W = W_0 exp\left[-\left(\frac{-RTln(\frac{P}{P_0})}{E}\right)^n\right] \qquad (3.2)$$

where, W is the weight adsorbed at P/P_0 and T, W_0 is the total weight adsorbed, E is the characteristic energy and n is a non-integer value (typically between 1 and 3) [11]. Characteristic energy (E) is the measure of the mean value of adsorption potential which is a measure of the affinity of the surface for the adsorbate molecules for microporous adsorbents. The values of component n and characteristic energy E were found to be related to pore size distribution. High value of n and low value of E result in narrow pore size distribution [9].

ACF10, ACF15 and ACF20 were made from the same precursors. However, they exhibit different pore properties, which is due to the variation of activation conditions. ACF20 with a higher surface area, more pore volume and bigger pore size was activated at a higher temperature. Regardless of precursors, total pore volume shows linear relation with the surface area: higher surface area corresponds to higher total pore volume, as shown in Figure 3.4. Since the majority of pores is micropores (Table 3.3), a similar trend is shown between surface area and micropore volume. Although the average pore diameter fluctuates in a narrower range of 24.28 and 26.82 regardless of precursors and activation conditions, DA micropore diameter is dependent on surface area: the higher the surface area, the bigger the micropore diameter is.

Table 3.2 BET surface area, pore volume and pore size of ACFs and PAC

	ACF10	ACF15	ACF20	CR	SY	PAC
BET surface area (m^2/g)	784.2	1370	2247	1763	806	913
Total pore volume (cc/g)	0.51	0.88	1.462	1.09	0.515	0.6
Average pore diameter (Å)	24.28	25.79	26.03	24.88	25.5	26.82
DA micropore width (Å)	11.97	15	17.69	16	14	14.2

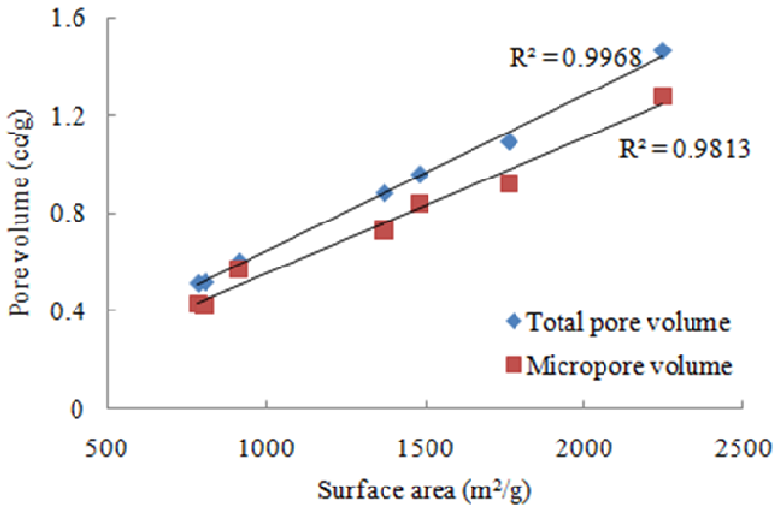

Figure 3.4 Relation between surface area and pore volume

Pore size distribution (PSD) of ACFs and PAC based on DA equation is illustrated in Table 3.3 and Figure 3.5. Among ACFs made from novoloid fibers (Table 3.3), the values of n for three of them are close to each other while ACF10 and ACF20 have the lowest and highest characteristic energy, respectively, indicating a narrower PSD of ACF10 which agrees with Figure 3.5. As the ACF20 was more activated than ACF10, separated micropores in ACF10 might be expanded and thus connect with neighboring micropores resulting in the formation of macropores. However, the value of n and E cannot generally represent the shape of pore size distribution for all ACFs and PAC discussed in this research.

Table 3.3 Pore volume distributions of ACFs and PAC

DA pore analysis	ACF10	ACF15	ACF20	PAC	CR	SY
Micropore (cc/g)	0.376	0.611	0.966	0.427	0.665	0.385
Mesopore (cc/g)	0.051	0.12	0.314	0.138	0.262	0.039
Macropore ($\times 10^{-4}$ cc/g)	1.92	2.81	12.7	18.5	13.9	0.323
Total pore volume (cc/g)	0.427	0.731	1.28	0.567	0.928	0.424
Micropore percentage (%)	88	83.55	75	75.33	71.63	90.73
Mesopore percentage (%)	11.98	16.41	24.53	24.35	28.22	9.26
Macropore percentage (%)	0.045	0.038	0.099	0.033	0.015	0.008
E (kJ/mol)	8.59	6.6	5.67	7.11	5.36	7.41
n	1.9	2.1	1.9	1.4	1.8	2.5

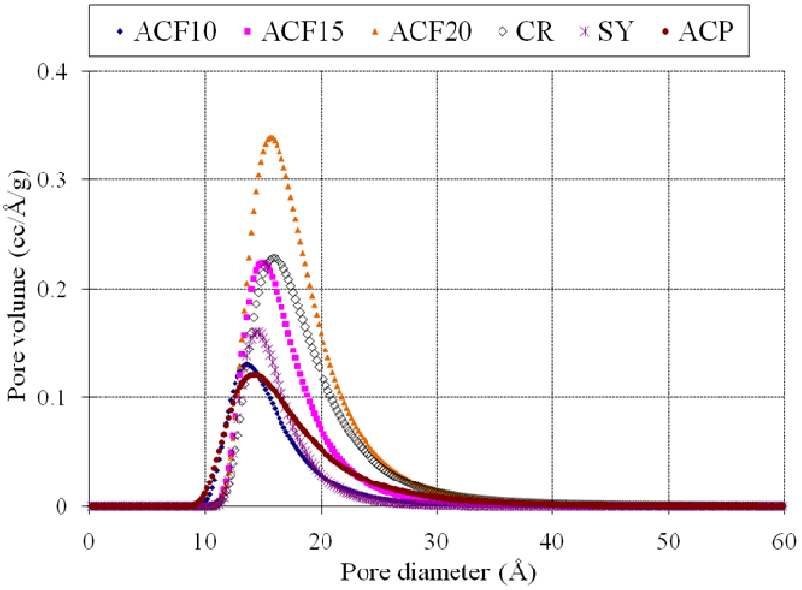

Figure 3.5 Pore size distributions of ACFs and ACP

The number of adsorption sites of ACFs and PAC, which is considered to be responsible for the adsorption of adsorbate over adsorbents, are summarized in Table 3.4.

Table 3.4 Number of adsorption sites of activated carbon fibers and PAC

Samples	ACF10	ACF15	ACF20	CR	SY	PAC
Number of adsorption sites ($\times 10^{20}$)	2.99	5.22	8.56	6.72	3.07	3.48

The surface morphology of ACF15 is shown in Figure 3.6. At a low magnification, a smooth fiber surface was observed without the appearance of pores. As the magnification was increased to 250,000, a macropore with a diameter of about 100nm and some mesopores showed up but micropores are still too small to see under SEM.

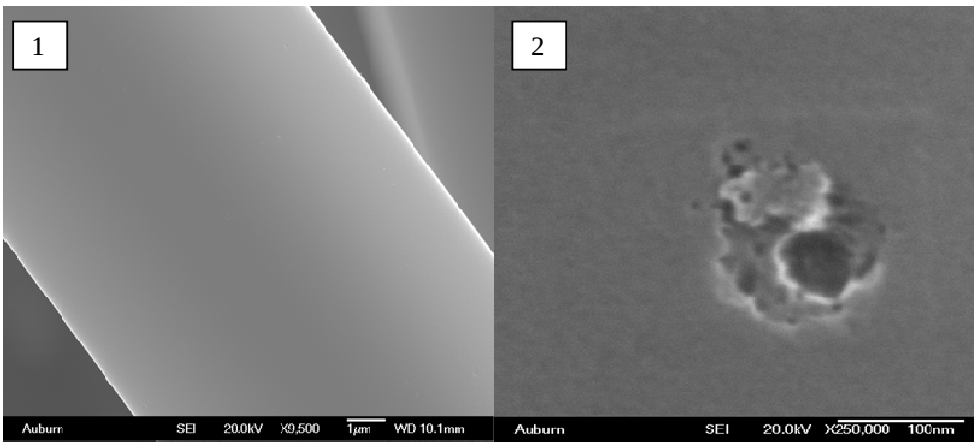

Figure 3.6 Surface morphology of ACF15 1) ×9500 and 2) ×250,000

PAC was found to be in an irregular shape rather than sphere as assumed by most research. The average PAC diameter is 290 μm with a coefficient of variation of 25.08%.

3.2.2. Element analysis

Nitrogen and carbon weight percentage of as received various activated carbon fibers were measured with burning tests and oxygen weight percent was calculated by weight difference; the results are shown in Table 3.5. Nitrogen content and the ratio of nitrogen to carbon in ACFs manufactured from the same precursor are found to be related to surface area although carbon and oxygen contents are less dependent on the surface area. The higher the surface area whose extent of activation may be higher, the more nitrogen detected. It can been seen that the elements in fibers are more dependent on the type of precursors of activated carbon fibers. Rayon based ACFs, CR and SY contain more nitrogen than novoloid based ACFs. The heat treatment at high temperatures burned non-carbon elements, nitrogen and oxygen.

Table 3.5 Element components of activated carbon fibers

	ACF10	ACF15	ACF20	CR	SY	ACF20-500	ACF20-700
N %	0.8	0.83	0.96	2.1	1.28	0.66	0.85
C %	97.7	87	94.5	87.1	87.6	96.9	96.9
O %	5.5	12.17	4.54	10.8	11.12	2.44	2.25
N/C %	0.849	0.958	1.015	2.407	1.463	0.686	0.874

* ACF20-500 and ACF20-700 refer to ACF20 after heat treatment at 500 and 700℃, respectively.

3.2.3 Sulfur dioxide adsorption properties of activated carbon fibers and modified activated carbon fibers

3.2.3.1 Sulfur dioxide adsorption over bare activated carbon fibers The activated carbons were subjected to 20 ppm sulfur dioxide with a face velocity of 33cm/s with air as the

balance at room temperature. The water was firstly excluded in the main gas stream, where the sulfur dioxide is expected to be adsorbed onto free sites on fiber surfaces where they are oxidized to sulfur trioxide. The resulting breakthrough time, breakthrough capacity, saturation capacity and utilization of ACFs and PAC are listed in Table 3.6.

Adsorption capacity of porous adsorbents is usually dependent on their surface area since more free sites are available in adsorbents with a higher surface area. However, there is no general relation between surface area and SO_2 breakthrough capacity of ACFs as shown in Figure 3.7.

Samples are classified according to precursors, namely novoloid-based ACFs and rayon-based ACFs. For novoloid-based ACFs, ACF10 with 88% micropores exhibited the highest breakthrough capacity of 1.72 while ACF20 with the least micropore ratio gave the lowest breakthrough capacity of 0.45. In the rayon-based ACF group, SY with 90.73% micropores is more capable in desulfurization than CR whose micropore ratio is much smaller, 71.63%. In other words, SO_2 breakthrough capacity of ACFs in dry condition is proportionately dependent on micropore ratio or on pore size distribution for each group: the higher the micropore ratio, the higher the breakthrough capacity. More micropores in adsorbents indicates a lower ratio of mesopores and macropores through which adsorbates have to pass before reaching adsorption sites in micropores where adsorption usually occurs. Blockage is more likely to happen if there are more macropores in adsorbents. Furthermore, SO_2 capacity for each group of ACFs was inversely proportional to micropore pore size, pore volume and surface area, which can be explained by the concept proposed by Marsh et al., where adsorbents with smaller

pores adsorb contaminants better at lower concentrations due to a higher overlap in potential between the pore and walls [10, 12].

Breakthrough profiles of ACFs and PAC are shown in Figure 3.8 when water is excluded in the carrier gas. ACF10, ACF15, ACF20 and CR became saturated by sulfur dioxide quickly after breakthrough in comparison with SY and PAC which have lower slopes in breakthrough curves. SY exhibited the highest utilization of 22.69% (Table 3.6) which is even higher than PAC which has the highest breakthrough and saturation capacity.

Although PAC has a longer breakthrough time and thus higher breakthrough capacity as shown in Figure 3.8, the breakthrough curve of PAC has lower slope which reflects the slower adsorption rate, probably due to harder access of adsorbates to free sites in pore, in comparison with ACFs. As discussed in Chapter 1, micropores in ACFs allow adsorbate to reach the fiber center directly while, in PAC, adsorbates have to pass through macropores in order to reach micropores where adsorption usually happens. The diameter of PAC was measured to be 290 μm, which is much thicker than ACFs with a diameter of about 12 μm. Although ACF20 and PAC have very close micropore ratio, micropores in PAC may be imbedded in the middle and therefore it is hard to reach for adsorbates.

Table 3.6 Sulfur dioxide capacities of bare activated carbon fibers in the absence of water

	ACF10	ACF15	ACF20	CR	SY	PAC
BT (min)	4.67	3.57	1.4	7.67	14.75	19
BC (mg SO_2/g sample)	1.72	1.32	0.45	2.85	5.05	7.07
SC (mg SO_2/g sample)	4.26	1.98	1.99	5.52	10.68	16.39
Utilization (%)	14.15	16.23	5.83	10.22	22.69	19.79

*Sample weight is about 0.5 g, the initial sulfur dioxide concentration is 20 ppm, and the face velocity is about 35 cm/s at the temperature of 20ºC. BT is the breakthrough time and BC is breakthrough capacity.

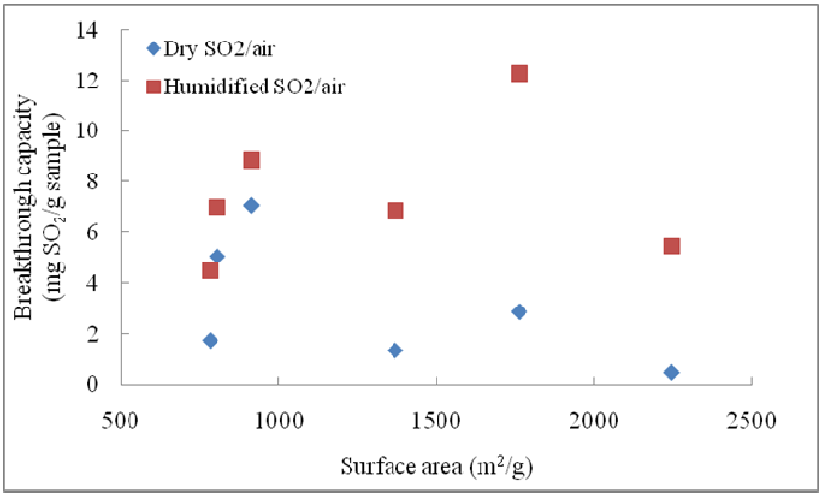

Figure 3.7 Effect of surface area of ACFs on sulfur dioxide breakthrough capacity

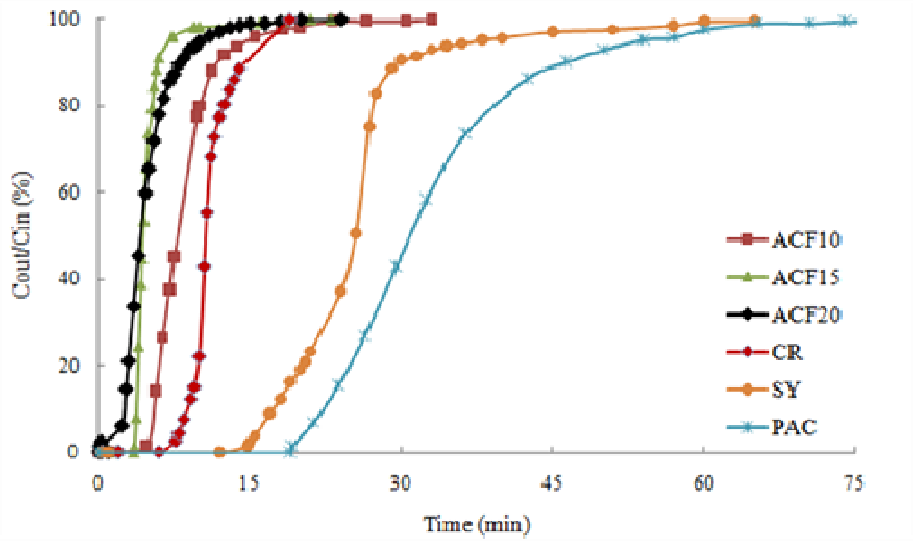

Figure 3.8 Breakthrough profiles of ACFs with the absence of water in gas stream (C_{in} is 20 ppm, velocity is 33 cm/s and sample weight is 0.5 g.)

Without the presence of water in the carrier gas, SY exhibits the highest breakthrough capacity with the longest period before breakthrough among all ACFs (Figure 3.8 and Table 3.6) although it is still lower than that of PAC. The spent SY felts were regenerated both in air (110°C for 2 hour) and nitrogen (600°C for 1 hour). Air-regenerated SY at 110°C gave a breakthrough capacity of 1.98 mg SO_2/g sample, which is 39.21% of the original capacity, while the nitrogen-regenerated SY shows a breakthrough capacity of 6.5 mg SO_2/g sample, which is 50% of the initial capacity, in dry air. The saturation capacity of nitrogen-regenerated SY is 4.93 mg SO_2/g sample, which is 46.16% of the fresh sample. Furthermore, the utilization of N_2-regenerated SY (27.08%) is a little higher than the fresh one (22.69%) which is due to decreased saturation time.

As shown in Table 3.7 and Figure 3.10, the presence of water in the main gas stream greatly increased the sulfur dioxide capacities of all ACFs and PAC while their utilizations were affected by water differently. Utilizations of ACF10, ACF15,ACF20

and CR were improved since their breakthrough times were increased greatly while those SY and PAC were reduced because they needed a lot longer time to achieve saturation as shown in breakthrough curves in Figure 3.9. For activated carbons fibers, the outlet SO_2 concentration first increased quickly after breakthrough; and then the rate of increase slowed down, causing longer time to achieve saturation. The increased capacity is attributed to the water which eventually promoted the continuous removal of sulfur dioxide through a series of procedures which was proposed by Mochida et al., and can be described by Figure 3.10 along with equations 3.3 - 3.8 [13]. The oxidized sulfur dioxide, sulfur trioxide, is hydrated by water producing sulfuric acid which is attached to fiber surfaces occupying the adsorption sites. If extra water is available, adsorbed sulfuric acid is eluted to aqueous from fiber surface releasing active adsorption sites for coming sulfur dioxide, preceding the continuous removal of sulfur dioxide.

Table 3.7 Sulfur dioxide capacities of bare activated carbon fibers with water present

	ACF10	ACF15	ACF20	CR	SY	PAC
BT (min)	25	18.5	14.67	24	19.75	24
BC (mg SO_2/g sample)	7.92	6.84	5.46	8.73	6.99	8.86
80% SC (mg SO_2/g sample)	13.89	20.1	37.32	32.23	44.94	74.81
Utilization (%)	21	25.26	10.55	16.78	7.68	5.8

*Sample weight is about 0.5 g, the initial sulfur dioxide concentration is 20 ppm, and the face velocity is about 35 cm/s at the relative humidity of about 100% and temperature of 20ºC. BT is the breakthrough time and BC is breakthrough capacity.

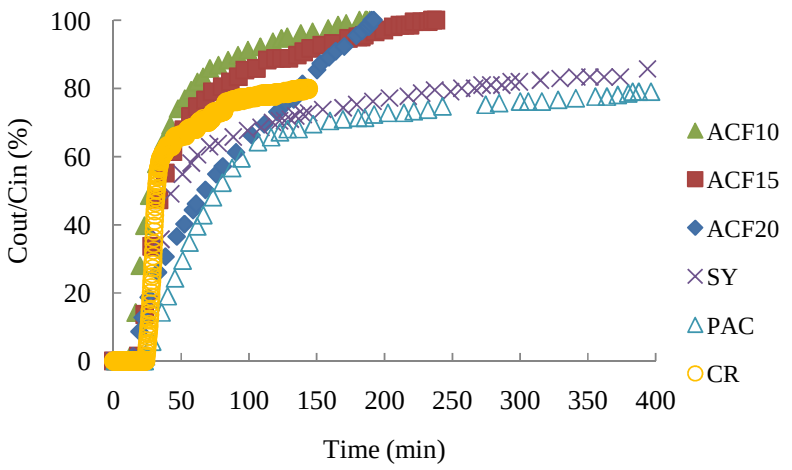

Figure 3.9 Breakthrough profiles of ACFs with the presence of water in the carrier gas (Initial sulfur dioxide concentration was 20 ppm, face velocity was 33 cm/s and sample weight was 0.5 g).

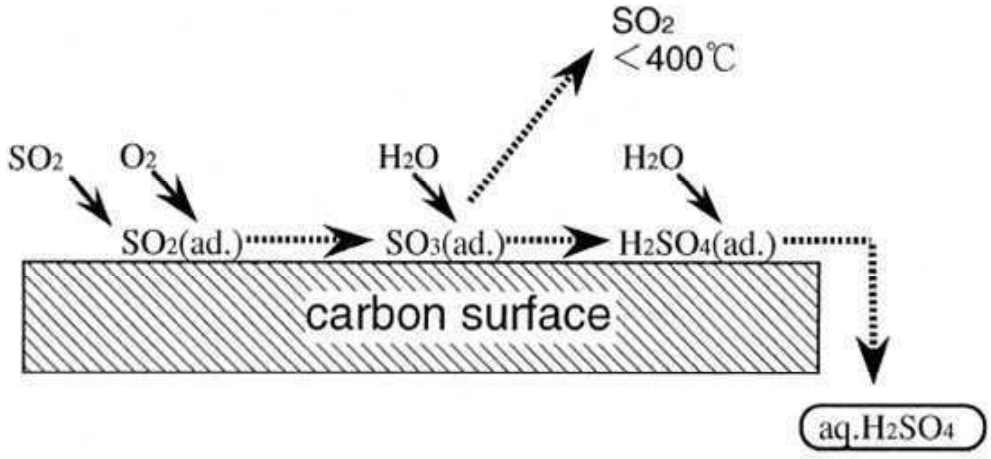

Figure 3.10 Mechanism of sulfur dioxide removal over activated carbon surface with the presence of oxygen and water [13]

$$SO_2 \rightarrow SO_{2(ads)} \quad (3.3)$$

$$H_2O \rightarrow H_2O_{(ads)} \quad (3.4)$$

$$O_2 \rightarrow 2O_{(ads)} \quad (3.5)$$

$$SO_{2(ads)} + O_{(ads)} \rightarrow SO_{3(ads)} \quad (3.6)$$

$$SO_{3(ads)} + H_2O_{(ads)} \rightarrow H_2SO_{4(ads)} \quad (3.7)$$

$$H_2SO_{4(ads)} + nH_2O \rightarrow H_2SO_4 \cdot nH_2O_{(ads)} \quad (3.8)$$

When water was present in the carrier gas, the breakthrough capacity of novoloid-based ACF is still proportionally related to micropore ratio of ACFs, which is the same trend with those with the absence of water. However, their saturation capacities increased with the surface area and pore volume, as shown in Table 3.7. In comparison with fibers, PAC has a higher breakthrough capacity if water is absent in the carrier gas. If the air was humidified before mixing with sulfur dioxide, breakthrough capacity of CR is close to PAC but saturation capacity of PAC is higher.

Moreover, under humid conditions, both breakthrough capacity and saturation capacity of ACFs are observed to be impacted by nitrogen content in fibers. The higher the nitrogen content, the higher the breakthrough and saturation capacity of ACFs.

Considering the long experiment period, the input sulfur dioxide concentration was increased to 50 ppm, the resulting SO_2 capacities and breakthrough curves over ACF10, ACF15, ACF20, CR and PAC in the presence of water are shown in Table 3.8 and Figure 3.11, respectively.

Table 3.8 Sulfur dioxide capacities of bare ACFs with initial SO_2 concentration of 50 ppm and humidified air as the carrier gas

	ACF10	ACF15	ACF20	CR	PAC
BT (min)	3.48	1.7	0	4.67	3.15
BC (mg SO_2/g sample)	2.63	1.3	0	3.53	2.405
80% SC (mg SO_2/g sample)	12.66	14.77	28.94	11.64	36.6
80% Saturation Utilization (%)	13.92	5.89	-	28.3	4.505

Compared to low concentration sulfur dioxide challenge, breakthrough times and capacities of ACFs and PAC decreased drastically when exposed to a higher concentration SO_2. ACF20 did not show any capacity at breakthrough. The same phenomenon of low utilization of PAC was observed regardless of challenge concentration of sulfur dioxide though higher saturation capacities could be reached.

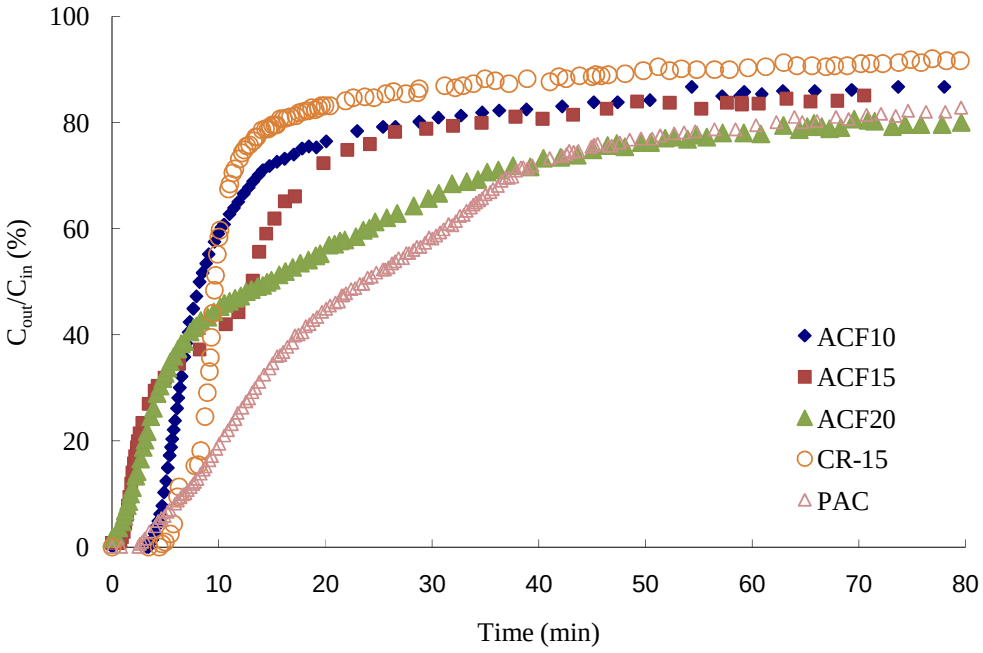

Figure 3.11 Breakthrough profiles of ACFs in SO_2/humidified air (Initial SO_2 concentration was 50 ppm, the face velocity was 33 cm/s and sample weight was 0.5 g)

3.2.3.2. Sulfur dioxide adsorption over alkali/ACF ACF20 has the largest surface area and pore volume among all ACFs available in the lab and thus is expected to accommodate more solutions in pores, ACF20 was immersed in KOH and K_2CO_3 solutions to apply them onto ACF20. A variety of weight percentages of KOH or K_2CO_3

were loaded on ACF20: 5, 8.67, 11, 29.3 wt% KOH and 8.67, 19.3 and 28 wt% K_2CO_3. Their sulfur dioxide capacities were evaluated while exposed to 20 ppm sulfur dioxide carried by dry air with a face velocity of 33 cm/s at room temperature (20ºC). Breakthrough behaviors of these samples are compared in Figure 3.12. It can be seen that even a small amount of KOH (5 wt%) on ACF20 increased the breakthrough time from 1.4 min to 21min, and increased the breakthrough capacity from 0.45 to 7.81 mg SO_2/g sample. However, the increased capacity by alkali sacrificed the adsorption rate of ACF20, which is elucidated by less steep breakthrough curves of alkali/ACF20 compared to bare ACF20 in Figure 3.12. However, the utilization of ACF20 was increased. Both SO_2 breakthrough capacity and saturation capacity are increased with the increased KOH and K_2CO_3 content (up to 29 wt%) on ACF20, as shown in Figure 3.13. The influences of KOH load on breakthrough and saturation capacities are different. On the one hand, at low KOH weight ratio on AF20, breakthrough capacity increased quickly but the increase in speed slowed down when 8.67 wt% or more KOH were loaded. On the other hand, the saturation capacity of KOH/ACF20 gradually increased with the increased KOH amount on ACF20. The similar trend was observed for K_2CO_3/ACF20 as well. Utilizations of alkali/ACF20 are less dependent on alkali weight ratio: the increase was from 12.96% at 5 wt% KOH to 21.18% at 8.67 wt% KOH; the fluctuation was in the range of 19.72~22.15% for other alkali loads.

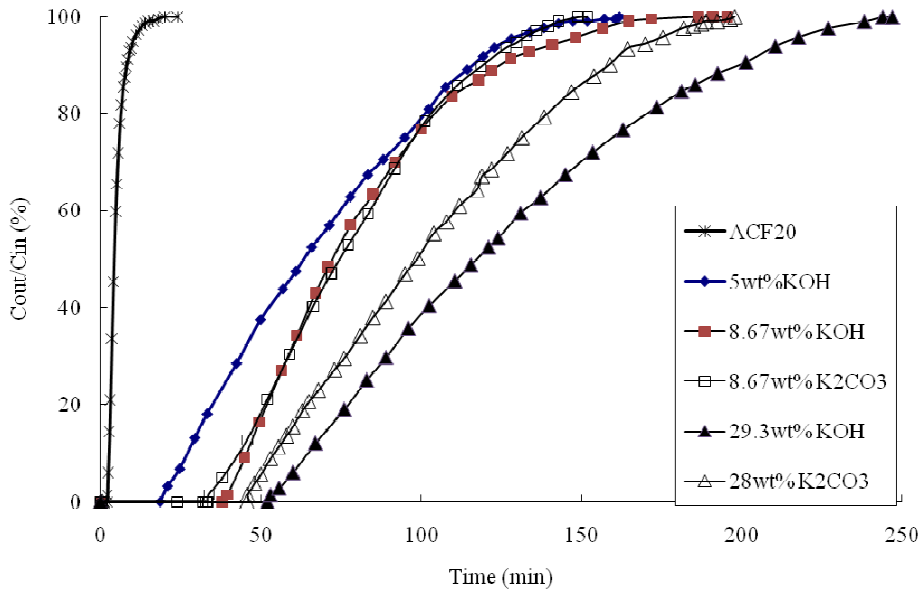

Figure 3.12 Breakthrough curves of KOH/ACF20 exposed to 20 ppm SO_2 carried by dry air (C_{in}=20 ppm, Face velocity=33 cm/s, Sample=0.5 g)

Although potassium carbonate is weaker alkali in comparison with potassium hydroxide, with the same load (8.67 wt%) on ACF20, their capacities are close and even the breakthrough curve shapes are very similar. However, as their load increased, their effect on sulfur dioxide capacity became distinct: KOH turns out to be a better promoter for sulfur dioxide removal.

It should be noted that one of the by-products of the desulfurization over K_2CO_3/ACF20, carbon dioxide, causes a second contamination on fuel cell system during the test, which is not desirable.

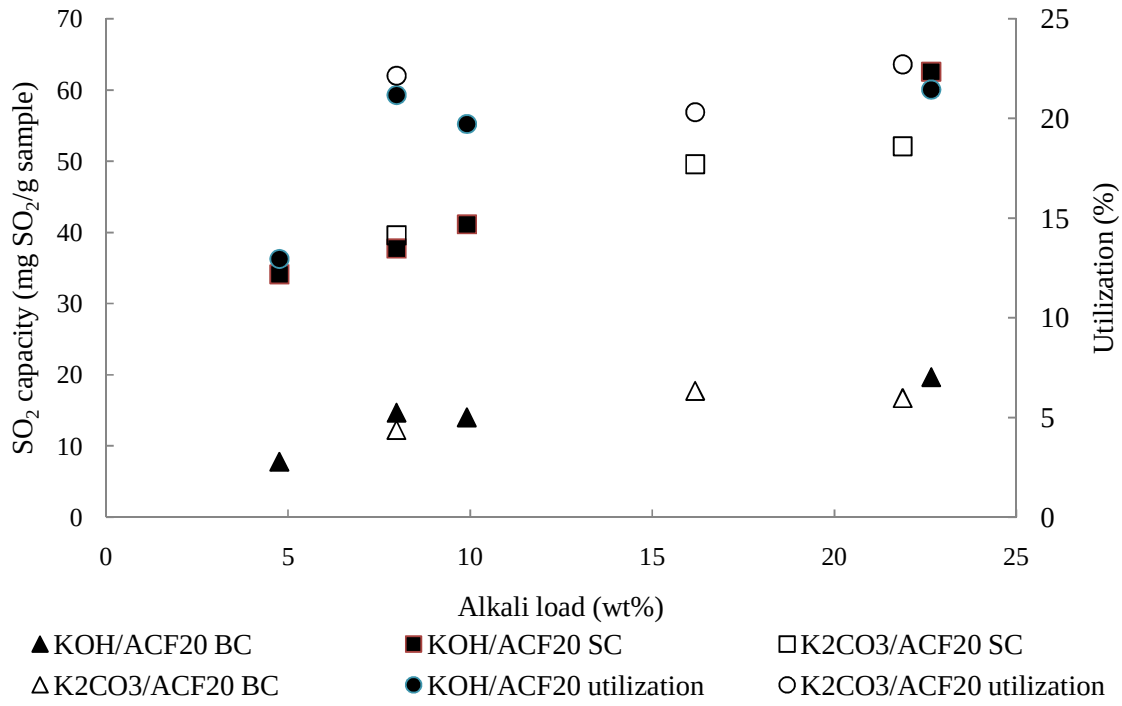

Figure 3.13 SO_2 adsorption capacity and utilization of KOH/ACF20 and K_2CO_3/ACF20

3.2.3.3 Sulfur dioxide adsorption over activated carbon fibers supported metal catalysts

Copper, nickel and iron were supported on ACF20 in order to enhance sulfur dioxide removal abilities of ACFs because these three metal derivatives were reported to have higher activity in sulfur dioxide removal. Metal/ACF20 was exposed to the challenge gas of 50ppm sulfur dioxide carried by humidified air with a face velocity of 33 cm/s. Treatment parameters and resulting breakthrough capacities are shown in Table 3.9. In comparison with bare ACF20 under the same conditions, the loads of metals of copper, nickel and iron enhanced the sulfur dioxide breakthrough capacity at different levels.

When copper and nickel were loaded on fibers with the incipient wetness method, the former had higher sulfur dioxide capacity. However, when they were loaded with immersing ACFs in metal nitrate solutions, the capacities were found to be much lower, about 1. 3mg SO_2/g sample. Pretreatment with HCl before modification with copper nitrate by the incipient wetness method increased the sulfur dioxide breakthrough capacity from 3.55 to 9.28 mg SO_2/g sample.

Table 3.9 Sulfur dioxide capacities of metal/ACF20

ACFs	Metal precursors	Con[1] (wt%)	Load (wt%)	TM[2]	BT (min)	BC ($mgSO_2/g$ sample)
ACF20	$Cu(NO_3)_2 \cdot 3H_2O$	12.9	5	IWI	4.5	3.55
HCl-ACF20[3]	$Cu(NO_3)_2 \cdot 3H_2O$	12.9	5	IWI	11.8	9.28
HNO_3-ACF20[3]	$Cu(NO_3)_2 \cdot 3H_2O$	12.9	5	IWI	2.16	1.78
ACF20	$Ni(NO_3)_2 \cdot 6H_2O$	16.96	5	IWI	3.34	2.62
ACF20	$Fe(NO_3)_3 \cdot 9H_2O$	17.34	3.5	IWI	11.67	9.25
ACF20	$Cu(NO_3)_2 \cdot 3H_2O$	12.9	51.15	IM[4]	1.667	1.305
ACF20	$Cu(NO_3)_2 \cdot 3H_2O$	2	7.9	IM[4]	1.667	1.309

1. Concentration of precursor solutions; 2. Treatment method; 3. HCl-ACF20 and HNO_3-ACF20 represent ACF20 was pretreated with HCl and HNO_3, respectively; 4. Immersion.

3.2.3.4 Sulfur dioxide adsorption over activated carbon fiber supported oxidants Two different oxidants were used to oxidize sulfur dioxide in the current research: potassium chlorate and potassium permanganate. They were treated on ACF15 by spraying a certain amount of $KClO_3$ or $KMnO_4$ solutions over ACF15 followed by washing and drying. The prepared oxidant/ACF15 fibers were exposed to 50 ppm SO_2 stream carried by either dry or humidified air with a face velocity of 33 cm/g at room temperature of 20°C.

Capacities of ACF15 loaded with $KClO_3$ by impregnation are shown in Figure 3.14. It can be concluded that breakthrough capacity is promoted almost linearly by loading $KClO_3$ on the fibers. The maximum SO_2 capacity is expected with a certain amount of

$KClO_3$ considering that overloading may result in pore blockage. However, $KClO_3$ is easily removed by exposure to water and thus it is not suitable for wet-laying which is a flexible method for forming activated carbon fiber paper. When the same amount of $KClO_3$ and $KMnO_4$ (for example, 15 wt%) was applied to ACF15 separately, $KMnO_4$ showed a higher capacity, about 40 mg SO_2/g sample, compared to about 27 mg SO_2/g sample of $KClO_3$ as shown in Figure 3.15. Another issue of potassium chlorate is that the mixture of sulfur and $KClO_3$ is prone to spontaneous deflagration and sulfur-containing acids can cause spontaneous ignition [14].

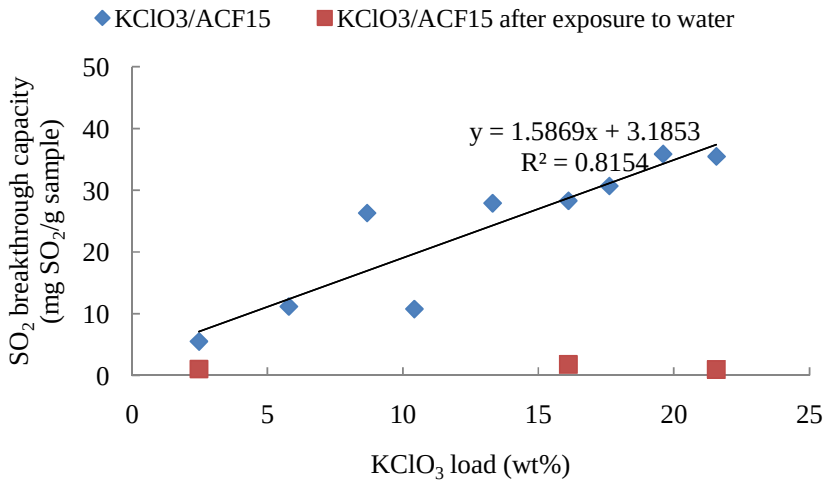

Figure 3.14 SO_2 breakthrough capacities of $KClO_3$/ACF15 before and after exposure to water

Different weight ratios of $KMnO_4$ were loaded on ACF10, ACF15, ACF20 and PAC, to investigate the best support. In Figure 3.15, it can be seen that, as $KMnO_4$ content increases on ACF10, ACF15, ACF20 and PAC, the breakthrough capacities increase. With the same amount of $KMnO_4$, PAC exhibited the lowest sulfur dioxide breakthrough capacity and ACF10 showed the best capacity to remove SO_2 among the three different

ACFs. Although ACF20 contains the largest pore volume and thus was expected to accommodate more $KMnO_4$ solutions than the other two, $KMnO_4$/ACF20 exhibits the lowest capacity for sulfur dioxide.

When $KMnO_4$ solution was injected onto ACFs, it was expected to be diffused into the pores without forming aqueous solutions. However, when the solution volume was greater than 5 mL, which resulted in 10 wt% $KMnO_4$ over ACF10, extra aqueous solution was observed with ACF10. Thus, ACF10 was suspected to hold more solution with increased $KMnO_4$ weight ratio. Therefore, ACF15 was chosen for the rest of the research work.

As discussed previously, KOH, K_2CO_3 and $KClO_3$ are not eligible for the wet-laying method to form activated carbon fiber paper (ACFP). Capability of $KMnO_4$/ACF in SO_2 purification was slightly affected by exposure to water as shown in Figure 3.16. The maximum SO_2 capacity of $KMnO_4$/ACF was obtained with 43.34 wt% $KMnO_4$ load. Furthermore, the effect is more at a higher content of $KMnO_4$ than those with a lower ratio.

The breakthrough curves of $KMnO_4$/ACF15 prior to and after exposure to water are shown in Figure 3.17. They are similar to each other except the slightly increased slope of the washed sample, which is probably due to the higher contact efficiency caused by redistribution of $KMnO_4$ on ACF15 during washing. Although the breakthrough capacity of washed sample is higher, its saturation capacity of 210 mg SO_2/g sample is lower than that of 317 mg SO_2/g sample before washing.

It has been reported that experimental parameters affect desulfurization by carbon including gas component, temperature, humidity and other properties. $KMnO_4$/ACF15

was exposed to different challenge gases, namely, SO_2, SO_2+air, SO_2+H_2O and SO_2+H_2O+air and their breakthrough profile characteristics are compared in Figure 3.18, which exhibits drastically different SO_2 capacities and breakthrough curve patterns. Both the presence of oxygen and water promote the ability of desulfurization of $KMnO_4$/ACF15 (43.34 wt%) while co-presence of them enhances the ability further. Furthermore, the improvement of sulfur dioxide capacity caused by water seems to be more than that resulted from oxygen.

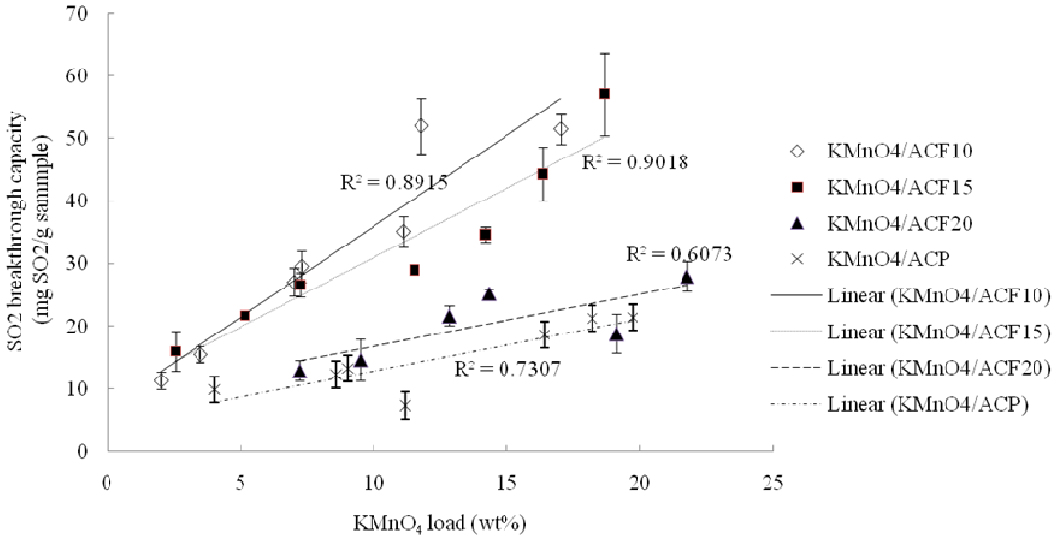

Figure 3.15 SO_2 breakthrough capacity of $KMnO_4$ loaded ACF10, ACF15, ACF20 and PAC (50 ppm input sulfur dioxide, 33 cm/s face velocity and 0.5 g sample for adsorption test).

For the same amount of KOH, K_2CO_3 and $KMnO_4$ on ACF20, such as 22 wt%, the breakthrough capacities were 19.69, 16.75 and 27.95 mg SO_2/g sample, respectively, indicating that $KMnO_4$ promoted the sulfur dioxide capacity more than the other two.

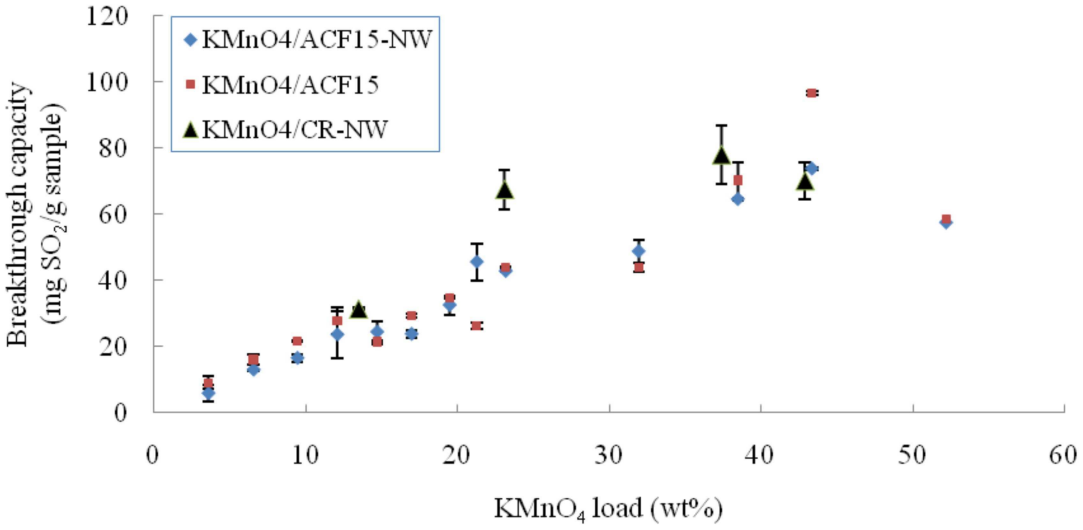

Figure 3.16 SO_2 breakthrough capacity of ACF15 loaded with different ratios of $KMnO_4$ (NW refers to non-washing).

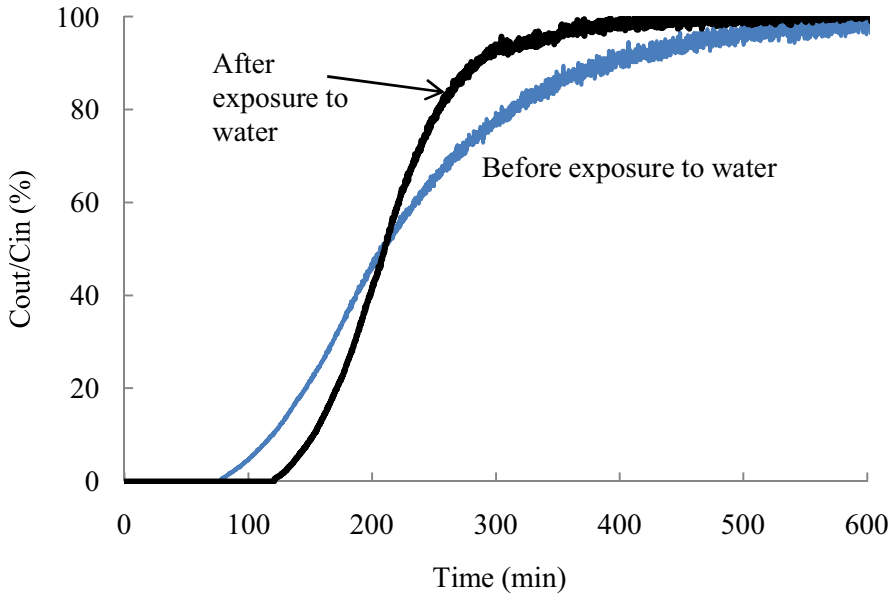

Figure 3.17 Breakthrough profiles of $KMnO_4$/ACF15 before and after exposure to water

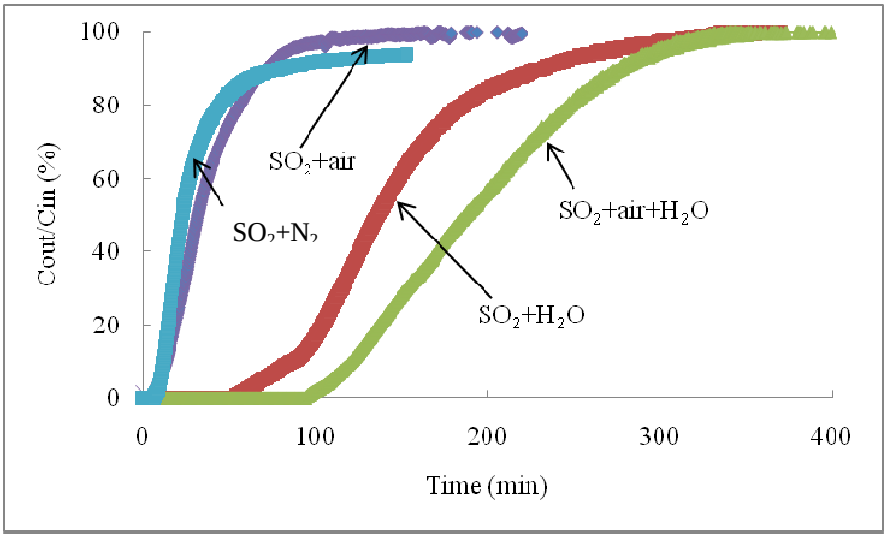

Figure 3.18 Breakthrough profiles of $KMnO_4$/ACF15 after exposure to water under different adsorption conditions

The potassium permanganate solutions used for $KMnO_4$/ACFs preparation were all 6 wt% so far. It is possible that the desulfurization capability was influenced by the precursor concentration. A lower $KMnO_4$ concentration (2 wt%) was used to treat ACF15 and different weight ratios of $KMnO_4$ were obtained. For the same $KMnO_4$ load (43 wt%) on ACF15, samples prepared from 2wt% and 6wt% solutions showed similar breakthrough curves and saturation process; however, ACF15 impregnated with 6wt% concentration of $KMnO_4$ solution exhibited a longer breakthrough period as shown in Figure 3.19. Their breakthrough capacities are 34 and 44.3 mg SO_2/g sample, respectively.

The adsorption properties of ACF15 with 20, 33 and 43 wt% KMnO4 prepared from 2wt% solutions are illustrated in Figure 3.19. Their breakthrough capacities were calculated to be 34, 59.7 and 60.8 mg SO_2/g sample, respectively. It can be seen that,

with the increase of $KMnO_4$ content, sulfur dioxide saturation capacity increased but the breakthrough capacity increased first and then leveled off.

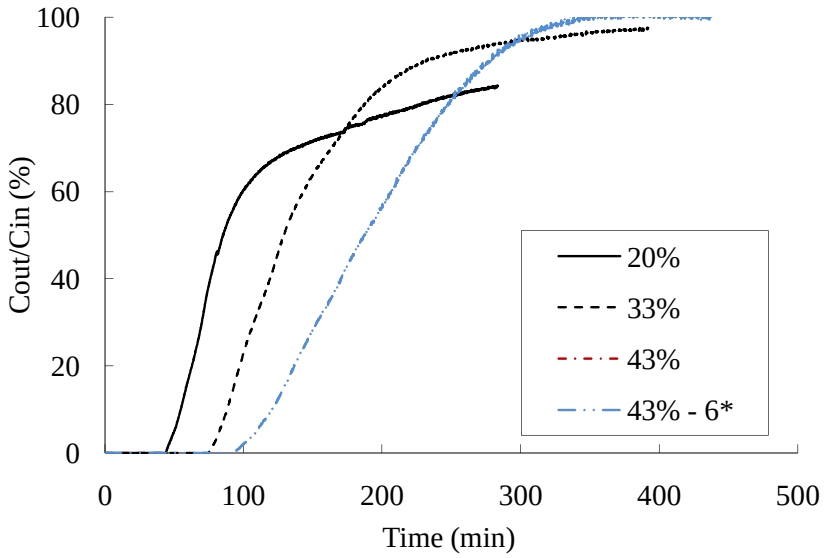

Figure 3.19 Breakthrough profiles of $KMnO_4$/ACF15 prepared from 2 wt% $KMnO_4$ solutions (* 43%-6 represents the sample prepared from 6wt% $KMnO_4$ solution)

It was reported that the pre-humidification before activated carbons were exposed to sulfur dioxide improved the sulfur dioxide removal efficiency by forming a water film over carbon surface where the conversion of sulfur trioxide to sulfuric acid and elution of aqueous sulfuric acid from carbon surfaces were promoted. $KMnO_4$ treated ACF15 was exposed to humidified air (91% relative humidity) for one hour before starting the sulfur dioxide adsorption test and a film of water was expected to form. However, the breakthrough period was shortened in comparison with dry KMnO4/ACF15s (Figure 3.20) and the adsorption rate was initially similar which is indicated by a similar slope of the breakthrough curve. After 80% sulfur dioxide released from the reactor, the adsorption rate on the prehumidified sample slowed down and became lower than that of

dry samples. On the other hand, the saturation capacity (85%) of prehumidified $KMnO_4$/ACF15 of 215 mg SO_2/g sample is higher than that of dry samples of 205 mg SO_2/g. Furthermore, as the adsorption process continues, a higher saturation capacity would be obtained if samples were prehumidified.

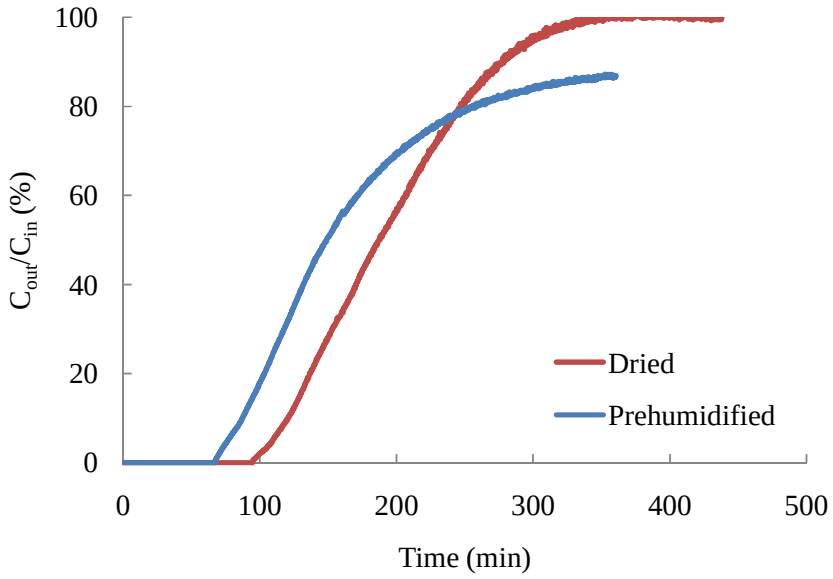

Figure 3.20 Sulfur dioxide adsorption properties of humidified $KMnO_4$/ACF15 in comparison with dried sample (initial SO_2 is 50 ppm, face velocity is 33 cm/s, and sample weight is 0.5 g.)

3.3 SEM imaging analysis

SEM images of $KMnO_4$/ACF15 with different chemical weight ratios are shown in Figure 3.21. At a low $KMnO_4$ load (6.55 wt%), the distribution of $KMnO_4$ on fiber surfaces are not uniform: some areas are smooth while $KMnO_4$ is dense on some other areas causing coarse fiber surfaces. As the weight ratio increased to 23.16 wt%, the uniformity of $KMnO_4$ was enhanced; it seems that fiber surfaces were covered by $KMnO_4$ at the weight percentage of 43.34 wt%. After exposure to water, $KMnO_4$ seemed to be redistributed uniformly, which may contribute to efficient contact between the

adsorbate and oxidant during adsorption tests, which is consistent with the sharper breakthrough curve as discussed in the previous section.

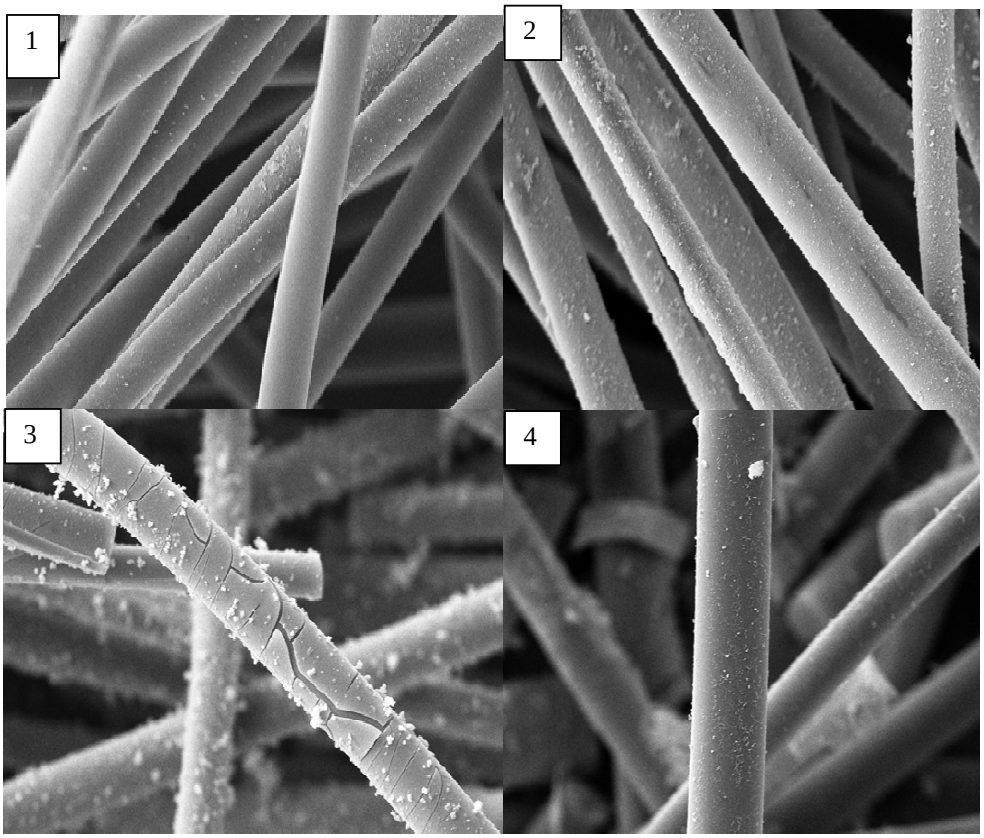

Figure 3.21 Surface morphology of $KMnO_4$/ACF15 1) 6.55wt% $KMnO_4$ 2) 23.16 wt% $KMnO_4$, 3) 43.34 wt% $KMnO_4$ and 4) 43.34 wt% $KMnO_4$ after exposure to water

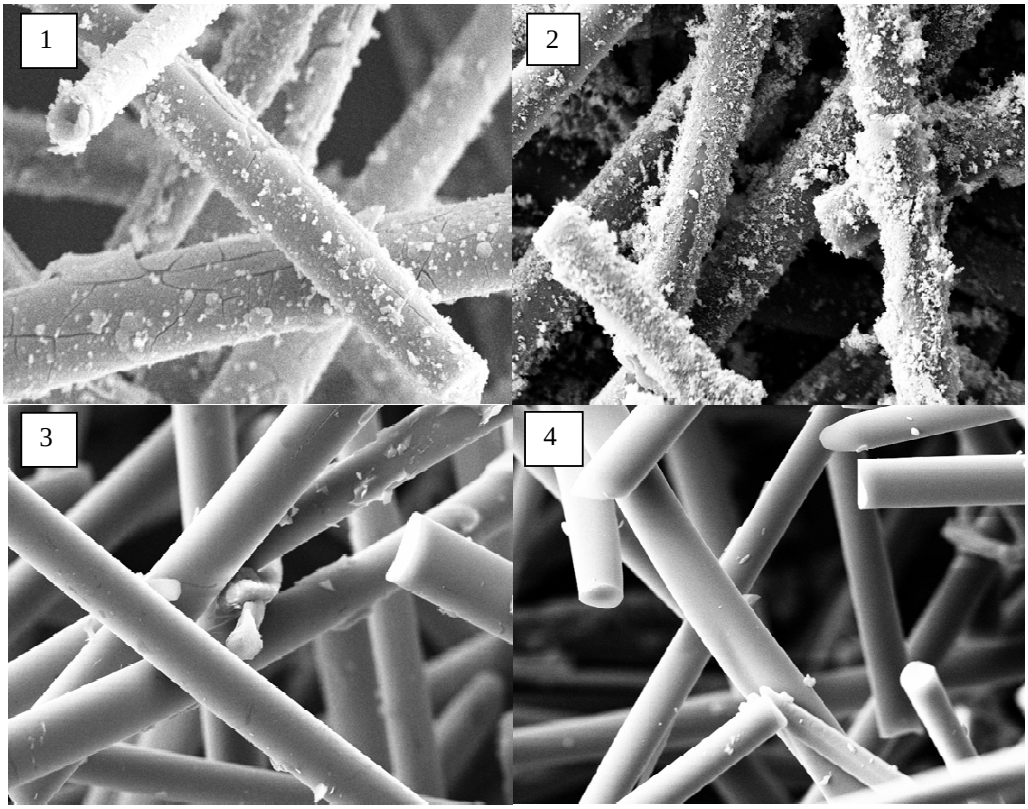

Figure 3.22 $KMnO_4$/ACF15 surface morphology after exposure to 1) SO_2+N_2, 2) SO_2+air, 3) $SO_2+H_2O+N_2$ and 4) SO_2+H_2O+air

Since 34.34 wt% $KMnO_4$ over ACF15 showed the highest sulfur dioxide capacity, they were subjected to different challenge gases: SO_2+N_2, $SO_2+H_2O+N_2$, SO_2+air and SO_2+H_2O+air and the spent samples were observed under SEM, which are shown in Figure 3.22. As $KMnO_4$/ACF15 was exposed to SO_2 only, the fiber surfaces were similar to the fresh sample but the challenge gas mixture of SO_2 and O_2 without water resulted in rougher surfaces. The coarse surfaces are considered to result from incomplete reaction between sulfur dioxide and potassium permanganate. However, the other two spent samples, which were exposed to the water-containing challenge gases, exhibited much smoother surface with few particles attached, which may be due $KMnO_4$ being consumed

by sulfur dioxide during the reaction. From the SEM images, it seems that a key factor to remove sulfur dioxide by potassium permanganate.

3.4 Activated carbon fiber papers (ACFP) and their SO_2 adsorption capacities

For the purpose of optimizing paper strength, bare ACFs rather than KMnO4/ACF15 were used. Thickness, tensile strength and coefficient of variation of thickness (CV) of thirteen ACFPs are shown in Figure 3.23. The composition of each sample is listed in Table 3.1.

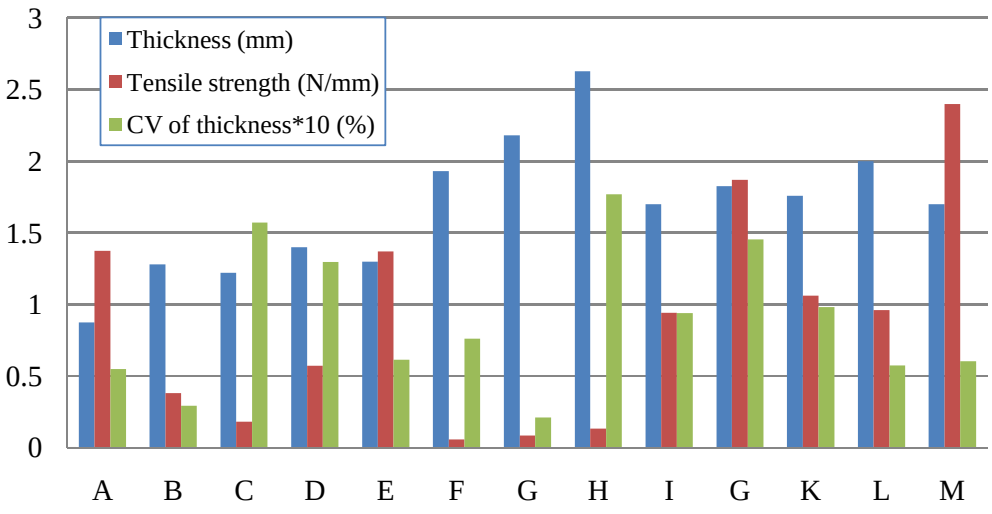

Figure 3.23 Thickness, tensile strength and coefficient of thickness variation (CV) of ACFP samples corresponding to Table 3.1

As shown in Figure 3.23, cellulose fibers in the manufactured ACFP A and B contributed greatly to the paper strength (the wet mat was dried in air without heating). As the ratio of cellulose fibers was decreased from 50% to 15%, the strength of ACFP decreased. 15% CoPET was included for sample C which was fused. It can be seen that the strength of ACFP A and B is mainly provided by the hydrogen bonding and entanglement between cellulose fibers. Among all the samples, ACFPs containing

ACF20 and cellulose show better uniformity than most of ACFPs containing CoPET probably due to easy dispersion of cellulose in the slurry. The hydrophobic feature of CoPET causes it to be less likely dispersed in water than the hydrophilic cellulose fibers. However, a high ratio of ACF20 is preferred for the purpose of sulfur dioxide removal and thus the weight ratio of ACF20 in ACFP was chosen 70% for the rest of samples. The cellulose and CoPET were mixed together as the bonding agents and papers were fused at high temperature for bonding from CoPET. As the fusing temperature increased from 135 to 200°C, the strength of ACFP also increased. However, the fusing temperature was limited by cellulose fibers which decompose above 200°C.

A large group of ACFP samples were made from ACFs (70 wt%) with CoPET (30 wt%) as the binder with a series of fusing temperatures. As the fusing temperature increased, the strength increased first and then decreased. As shown in DSC curves of CoPET (Figure 3.24), CoPET has two melting temperatures due to its core/sheath structure. The low melting point is attributed to the sheath and the high melting point is due to the core polyester. As the wet mat from the wet lay process was heated above the low melting point (76°C), the sheath of CoPET started melting and thus bonded ACF20 with the unmelted CoPET core which provided the structure of paper as shown in Figure 3.25. The higher the fusing temperature, the more polyester melted. However, while too much binder fibers were melted, less polyester was left, which thus resulted in weaker ACFPs. The optimum fusing temperature was found to be 200°C which gave the strongest ACFP (referring to sample G). Surfactant was used to enhance the affinity between CoPET and water and thus to produce a more uniform dispersion for the wet lay process, which corresponded to sample M. Other parameters were the same with the

sample G. Compared to G without surfactant, the low coefficient of variation of thickness in M indicates an increase in uniformity which accordingly may have contributed to the improved paper strength.

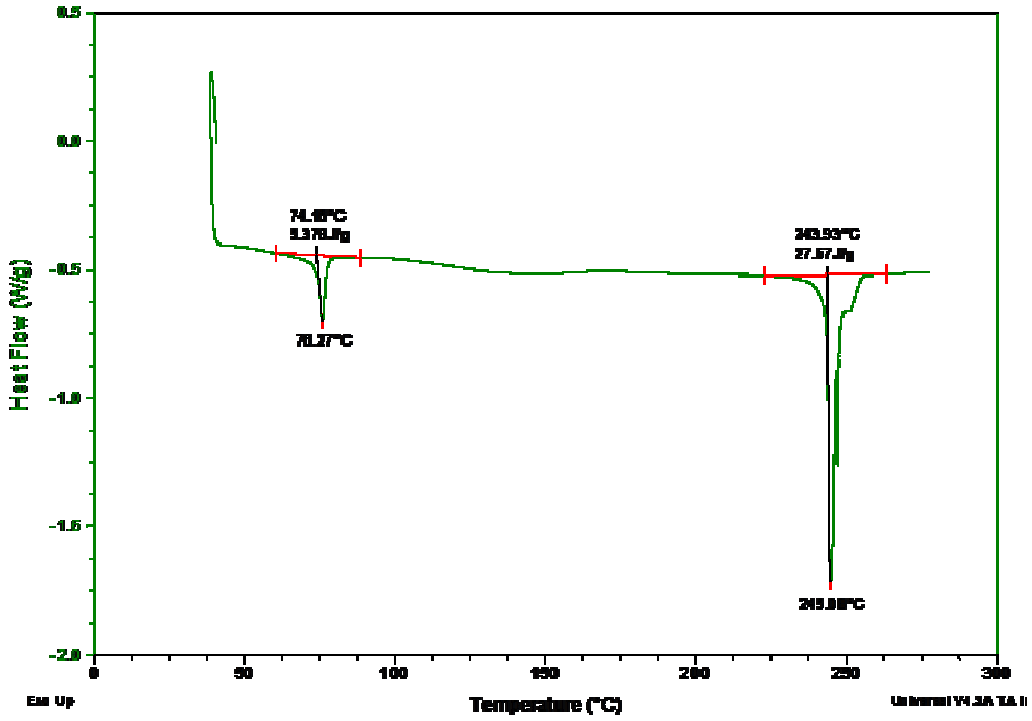

Figure 3.24 DSC analysis of CoPET

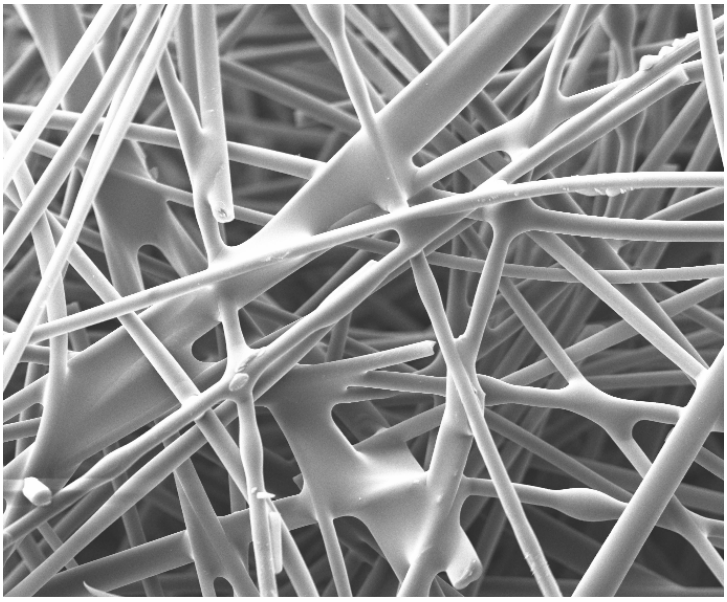

Figure 3.25 SEM images of ACFP composed of 70 wt% ACF20 and 30 wt% CoPET with a fusing temperature of 200°C for 20 min (×500)

$KMnO_4$/ACF15 paper (K-ACFP) was manufactured with optimum parameters obtained with the bare ACFs: the wet mat consisting of 70 wt% $KMnO_4$/ACF15 and 30 wt% CoPET was heated at 200°C for 20 min. The surface morphology of K-ACFP was observed with SEM as shown in Figure 3.26 (1). Fused polyester formed strong interaction in the K-ACFP but some parts of ACFs were covered with the fused binder fibers and thus the effective surface area for sulfur dioxide removal reduced in theory.

The ability of resulting K-ACFP in sulfur dioxide removal was tested and the breakthrough properties are shown in Figure 3.27. K-ACFP showed shorter breakthrough period because since $KMnO_4$/ACF15 was included because 30 wt% bicompoent polyester in ACFP. However, as the capacity was calculated with respect to $KMnO_4$/ACF15 rather than the sample weight of ACFP, the estimated breakthrough capacity of ACFP (76 mg SO_2/g modified ACF15) is close to that of fibers (74.78 mg

SO_2/g modified ACF15) while the saturation capacity of ACFP (186.75 mg SO_2/g modified ACF15) is less than that of fibers (210.83 mg SO2/g modified ACF15). ACFP exhibited quicker saturation illustrated by the steeper breakthrough curve (Figure 3.27), which is probably due to more efficient contact when activated carbon fibers are diluted by binders. As shown in Figure 3.26 (2), fiber surface after sulfur dioxide adsorption test became smoother with some scale-like substances which are probably the adsorption products.

It is possible that the desulfurization capability of $KMnO_4$/ACF15 is reduced due to the existence of joint points where fused binder fibers blocked fiber surface exhibiting the reaction. To investigate the effects of joints, the formed wet mat was dried naturally in air rather than heat at high temperature. Thus, binder fibers remained as they were and there were not joints in the fiber network. Fibers in unfused ACFP were individual fibers which were subjected to sulfur dioxide under the same conditions with those fused ACFP. The resulting 90% saturation capacity was 217 mg SO_2/g modified ACF15, which is slightly higher than those fused ACFP. It can be concluded that the joints formed by fusing only occupies a small part of reactive sites on fiber surfaces and thus barely influence sulfur dioxide capacity.

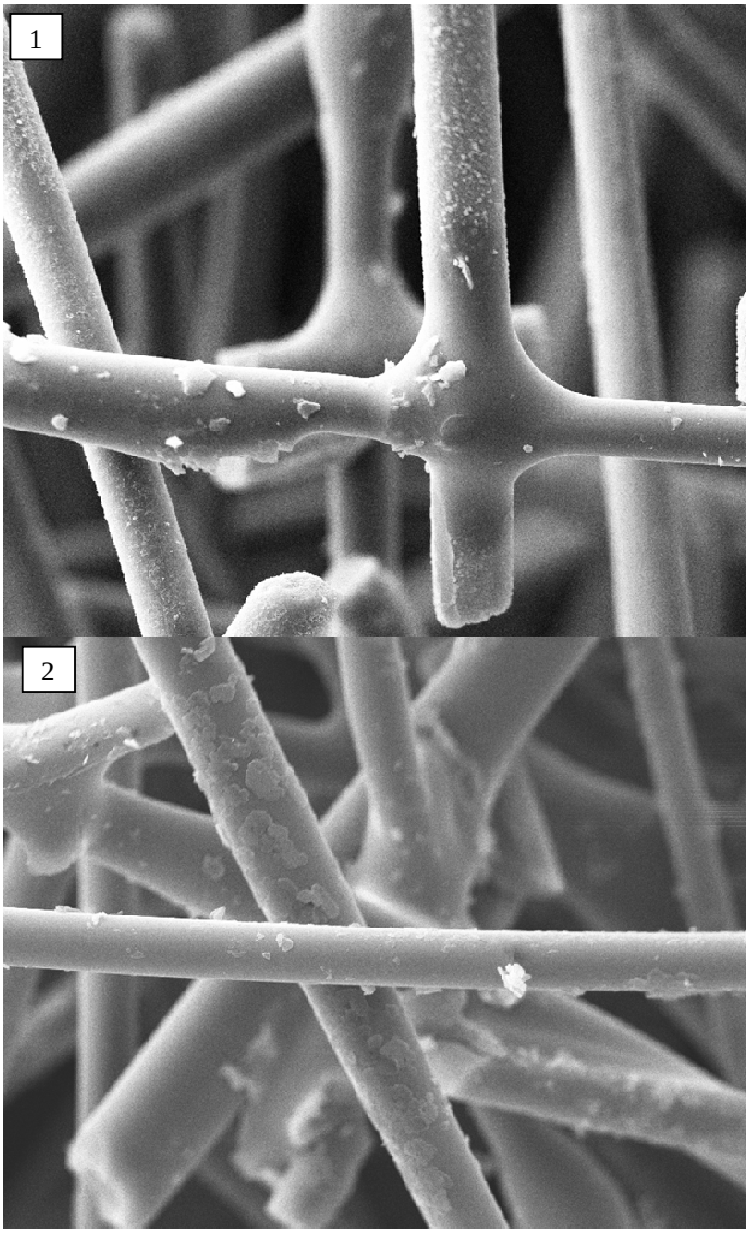

Figure 3.26 SEM images of K-ACFP: (1) before and (2) after sulfur dioxide adsorption tests (×2000).

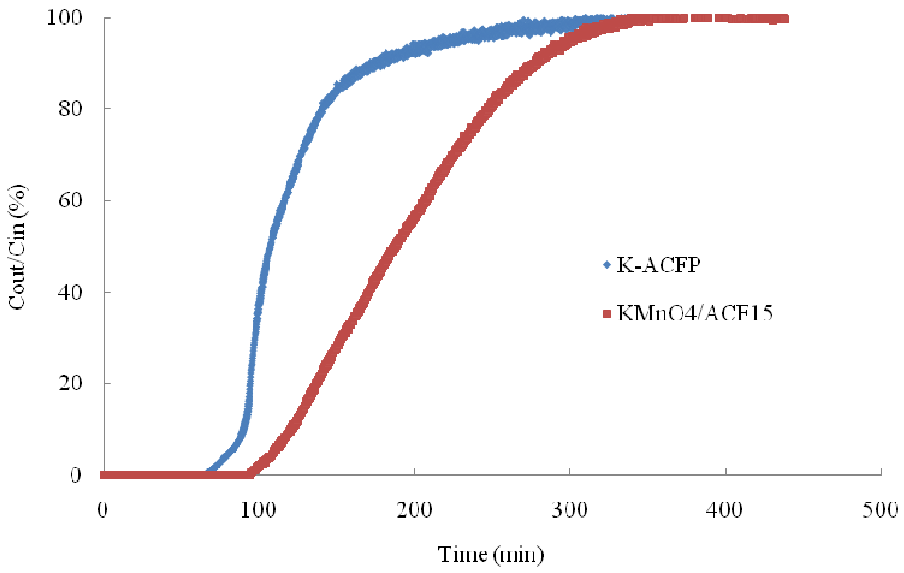

Figure 3.27 Breakthrough profiles of ACFP in comparison with $KMnO_4$/ACF15 with 50 ppm SO_2 challenging gas carried by humidified air (ACFP contains 0.35g $KMnO_4$/ACF15 while $KMnO_4$/ACF15 is 0.5 g).

3.5 XRD analysis on $KMnO_4$/ACF15

To investigate the changes on ACFs surface caused by the adsorption of sulfur dioxide with $KMnO_4$/ACF15, X-ray diffraction analysis was used. Bare ACF15, $KMnO_4$/ACF15 and spent $KMnO_4$/ACF15 after exposed to sulfur dioxide carried by dry air, dry nitrogen, humidified nitrogen and humidified air were subjected to X-ray scanning.

XRD patterns of ACF15, $KMnO_4$/ACF15 and spent $KMnO_4$/ACF15 after exposure to sulfur dioxide carried by humidified air are shown in Figure 3.28. Peaks at 14.5°, 28° and 34° indicate the crystals of MnO_2, which are only observed in the spent sample and therefore MnO_2 is considered to be one of the products during the adsorption test. The peak at 17° and 19° come from potassium permanganate. The expected product $MnSO_4$ during the sulfur dioxide adsorption was not detected probably due to the small amount.

MnO_2 was also detected by XRD after $KMnO_4$/ACF15 was exposed to the challenge gas of SO_2+H_2O+N_2 as shown in Figure 3.29. Figure 3.30 illustrates the XRD pattern of $KMnO_4$/ACF15 before and after adsorption in SO_2+air. There is no appearance of new peaks observed like in Figures 3.28 and 3.29. The same XRD pattern was obtained if adsorption was performed in SO_2+N_2. In other words, if water was absent from the challenge gas, reaction between sulfur dioxide and potassium permanganate on fiber surfaces would be less likely to occur, which is consistent with the previous discussion.

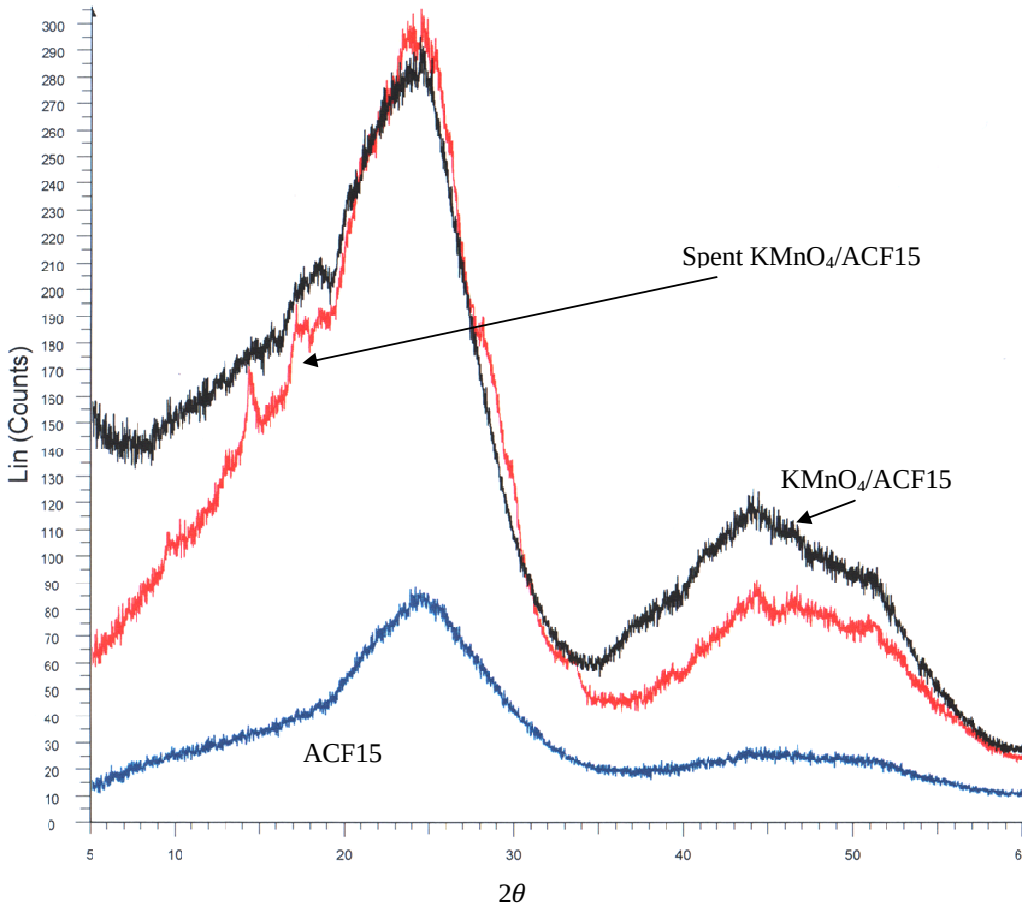

Figure 3.28 XRD patterns of ACF15, $KMnO_4$/ACF15 and spent $KMnO_4$/ACF15 after exposure to sulfur dioxide carried by humidified air

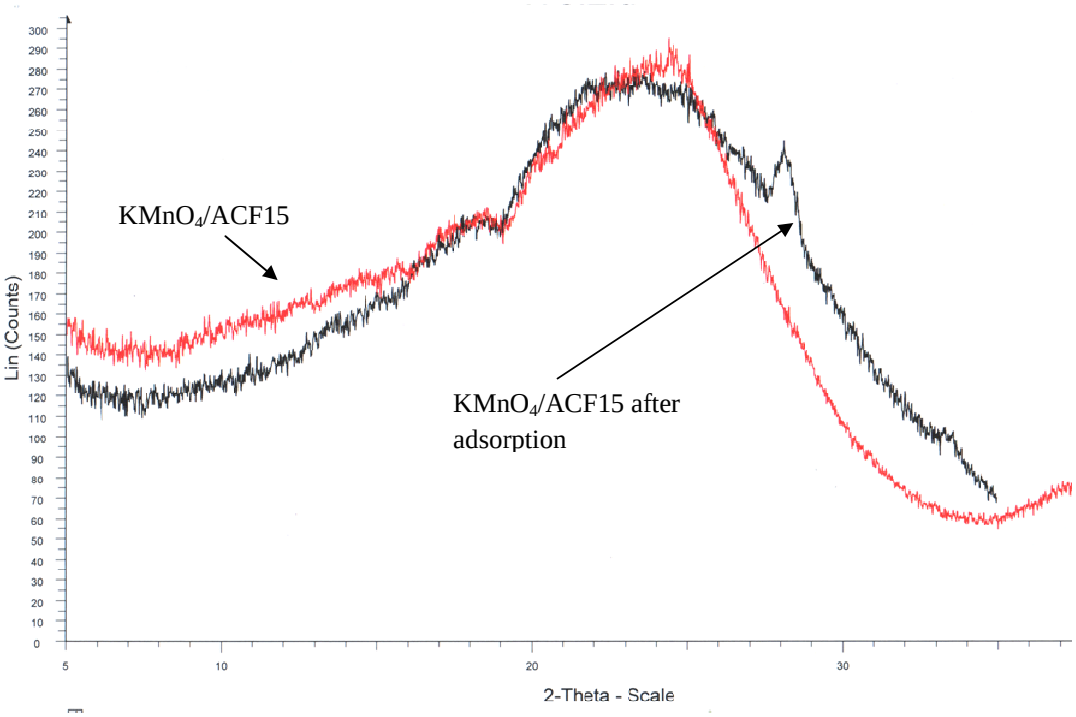

Figure 3.29 XRD patterns of $KMnO_4$/ACF15 before and after adsorption of sulfur dioxide carried by humidified nitrogen

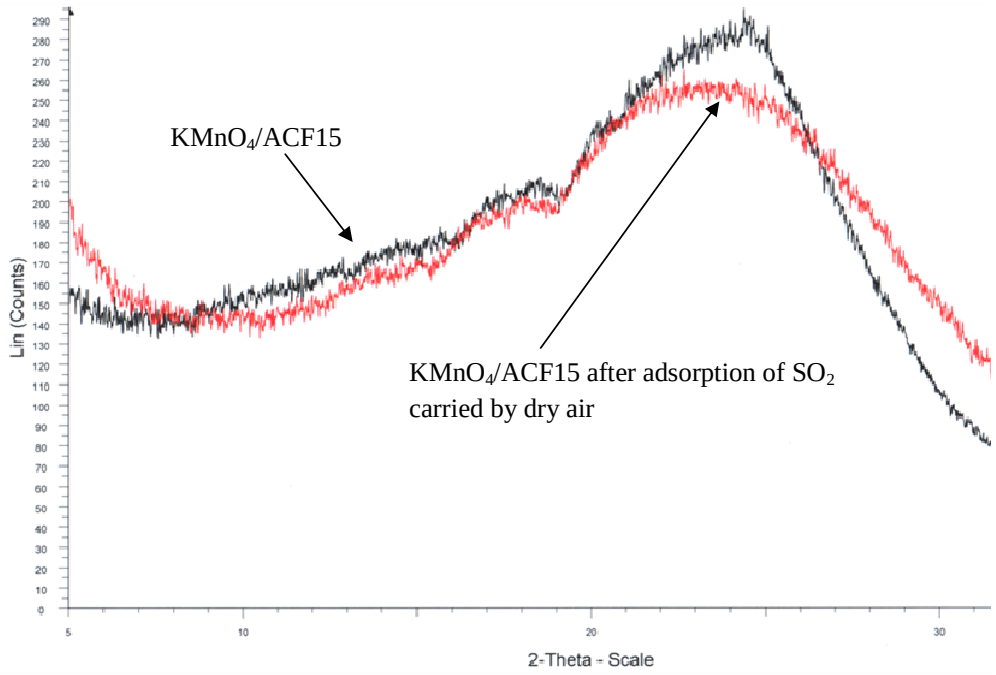

Figure 3.30 XRD patterns of $KMnO_4$/ACF15 before and after adsorption of sulfur dioxide carried by dry air

3.6 Energy Dispersive X-ray analysis

Energy Dispersive X-ray (EDS) analysis was performed on a SEM/EDS system to analyze the element composition on $KMnO_4$/ACF15 fiber surfaces both before and after sulfur dioxide adsorption tests with the carrier gas of humidified air. Weight percentages and atom percentages of K, Mn, S and C are listed in Table 3.10. Sulfur content on $KMnO_4$/ACF15 is very low, 0.045 wt% and 0.02 at%, but increased to 9.47 wt% and 4.3 wt%. Sulfur species were caught by adsorbents effectively and the goal of desulfurization was achieved. Changes of other elements are because of the change of sulfur ratio. As shown in Figure 3.31, before sulfur dioxide adsorption, the intensity of potassium and permanganate signals are very strong and sulfur signal is barely observed. However, after

adsorption, the sulfur signal intensity was strengthened greatly although the percentage of sulfur was still far lower than the carbon element.

Table 3.10 Element contents of $KMnO_4$/ACF15 before and after adsorption of SO_2 in humidified air

	K		Mn		S		C	
	wt%	at%	wt%	at%	wt%	at%	wt%	at%
Before	11.77	4.855	21.42	6.29	0.045	0.02	66.75	88.83
After	8.22	3.1	7.34	1.96	9.47	4.30	74.94	90.62

*wt% and at% represent weight percentage and atom percentage, respectively.

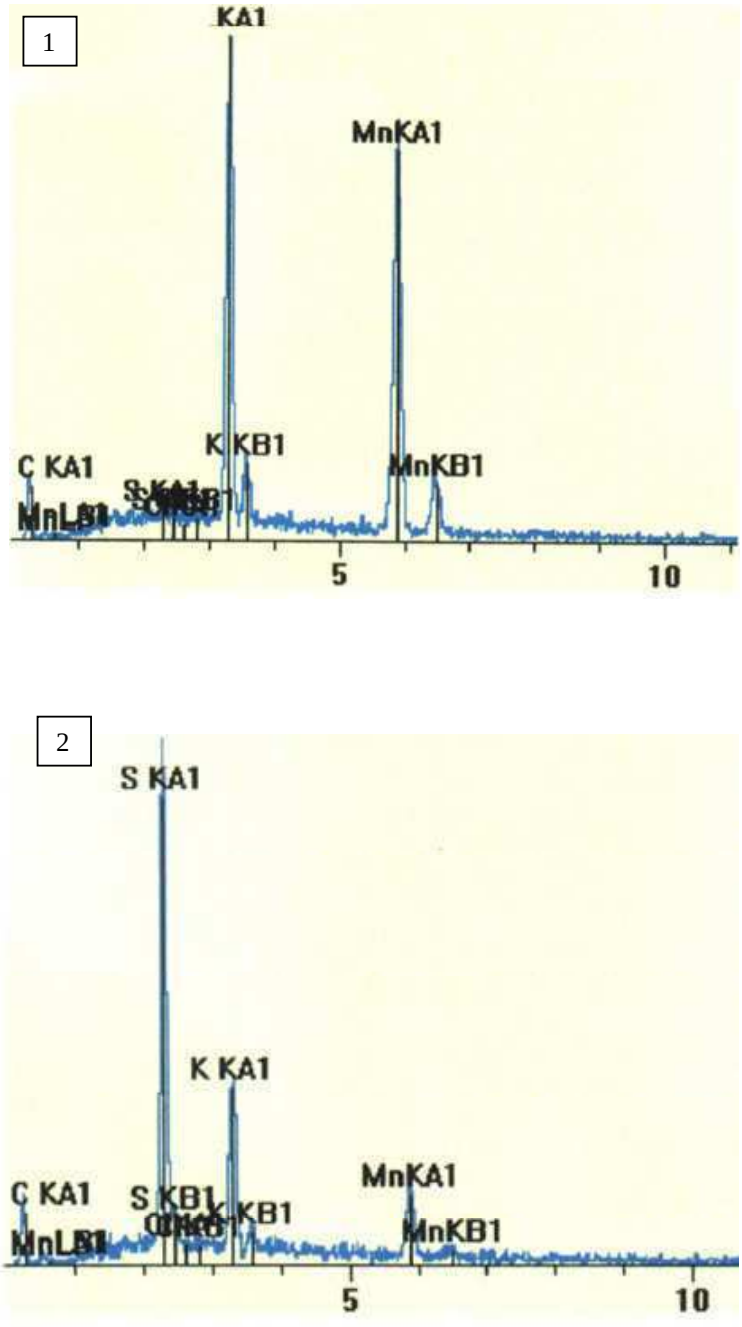

Figure 3.31 EDS element signals (1) before and (2) after adsorption in the challenging gas of SO_2+H_2O+air

References

1. Hayes, J., Activated carbon fiber textiles for filtration and separation, Brochure of American Kynol, Inc.
2. Das, D., Gaur, V. and Verma, N., Removal of volatile organic compound by activated carbon fiber, *Carbon*, 42 (14), 2949-2962, (2004).
3. Tseng, H. H. and Wey, M. Y., Study of SO_2 adsorption and thermal regeneration over activated carbon-supported copper oxide catalysts, *Carbon*, 42 (11), 2269-2278, (2004).
4. Davini, P., The effect of certain metallic derivatives on the adsorption of sulphur dioxide on active carbon, *Carbon*, 39 (3), 419-424, (2001).
5. Tseng, H. H., Wey, M. Y. and Fu, C. H., Carbon materials as catalyst supports for SO_2 oxidation: catalytic activity of CuO-AC, *Carbon*, 41 (1), 139-149, (2003).
6. Ma, J. R., Liu, Z. Y., Liu, S. J. and Zhu, Z. P., A regenerable Fe/AC desulfurizer for SO_2 adsorption at low temperatures, *Applied Catalysis B-Environmental*, 45 (4), 301-309, (2003).
7. Wang, J. Y., Zhao, F. Y., Hu, Y. Q., Zhao, R. H. and Liu, R. J., Modification of activated carbon fiber by loading metals and their performance on SO_2 removal, *Chin. J. Chem. Eng.*, 14 (4), 478-485, (2006).
8. Gaur, V., Sharma, A. and Verma, N., Removal of SO_2 by activated carbon fibre impregnated with transition metals, *The Canadian Journal of Chemical Engineering*, 85, 188-198, (2007).

9. Burevski, D., The application of the Dubinin-Astakhov equation to the characterization of microporous carbons, *Colloid and Polymer Science*, 260 (6), 623-627, (1982).

10. Marsh, H. and Rand, B., The characterization of microporous carbon by means of the dubinin-radushkevich equation, *Journal of Colloid and Interface Science*, 33, 101, (1970).

11. Autosorb-1 AS1 Win Version 1.51 operating manual, Boynton Beach, Florida USA, (2005).

12. Daley, M. A., Mangun, C. L., Debarr, J. A., Riha, S., Lizzio, A. A., Donnals, G. L. and Economy, J., Adsorption of SO_2 onto oxidized and heat-treated activated carbon fibers (ACFS), *Carbon*, 35 (3), 411-417, (1997).

13. Mochida, I., Korai, Y., Shirahama, M., Kawano, S., Hada, T., Seo, Y., Yoshikawa, M. and Yasutake, A., Removal of SO_x and NO_x over activated carbon fibers, *Carbon*, 38 (2), 227-239, (2000).

14. http://en.wikipedia.org/wiki/Potassium_chlorate, Jan 2010 accessed.

Chapter 4 Mechanism Analysis of Sulfur Dioxide Removal by ACFs and Model Development

4.1 Introduction

In 1946, Klotz proposed the concept of adsorption wave to understand the variation in concentration of a gas effluent from a bed of adsorbent and equations were derived to predict canister life [1]. Amundson supplied a complete mathematical solution of one particular problem according to the material balance over an elemental thickness of bed with the assumption of the local rate of removal made by Bohart and Adams and gave an equation to estimate the dependence of effluent concentration on time and location [2, 3]. Amundson's equation has been applied to practical adsorption over porous adsorbents to describe the breakthrough characteristics [4]; however, only the diffusion of adsorbates in the packed bed was considered. Later, Yang included the adsorption isotherm, mass and heat balance in the interpellet gas phase and mass and heat balance inside each pellet in models for an adsorption bed [5]. His concept was widely used in prediction of adsorption over activated carbon fibers. For example, Cheng et al., predicted the breakthrough curves of adsorption of volatile organic

compound (VOC) on ACFs in fixed beds [6]. Some researchers combined the diffusion of adsorbates in the adsorbent bed, the diffusion of adsorbates within single pore and adsorption isotherm or reaction on the pore walls. For example, Gupta et al., analyzed the breakthrough characteristics of sulfur dioxide over zeolites considering mass balances and adsorption isotherm [7]. Das et al., predicted the adsorption procedure of volatile organic compounds over activated carbon fibers with the same concept of Gupta et al. [8]. The removal of sulfur dioxide by ACFs in the presence of oxygen and water was modeled with this concept including the mass balance in the packed bed reactor, the mass balance within pores and reactions occurred on fiber surfaces [9]. Adapa et al., employed the same concept with that of sulfur dioxide removal on the catalytic oxidation of nitrogen monoxide by ACFs [10]. Only the reaction over fiber surface converting sulfur dioxide to sulfuric acid was considered by Mochida et al., in analyzing the kinetics of continuous removal of sulfur oxide using polyacrylonitrile-based ACFs; diffusions of adsorbates were ignored [11]. Yoon and his colleagues proposed a theoretical model for respirator cartridge service life by addressing the adsorption and breakthrough of contaminant vapors with the assumption that the rate of change in the breakthrough concentration is proportional to breakthrough concentration and to the number of reactive sites at a specific moment and that the rate of decrease in the probability of adsorption is directly proportional to the contaminant concentration and flow rate and inversely proportional to the weight of activated carbon charcoal. The model was applied to toluene and methyl acetate and predicted breakthrough curves agreed with the experimental data well [12].

In the present work, Yoon's model was applied to ACF20 and $KMnO_4$/ACF15, and the results were compared with the experimental results as shown in Figures 4.1 and 4.2. The predicted data deviate from the experimental data and deviations are unacceptable. Program code for prediction of breakthrough curves is listed in Appendix 1.

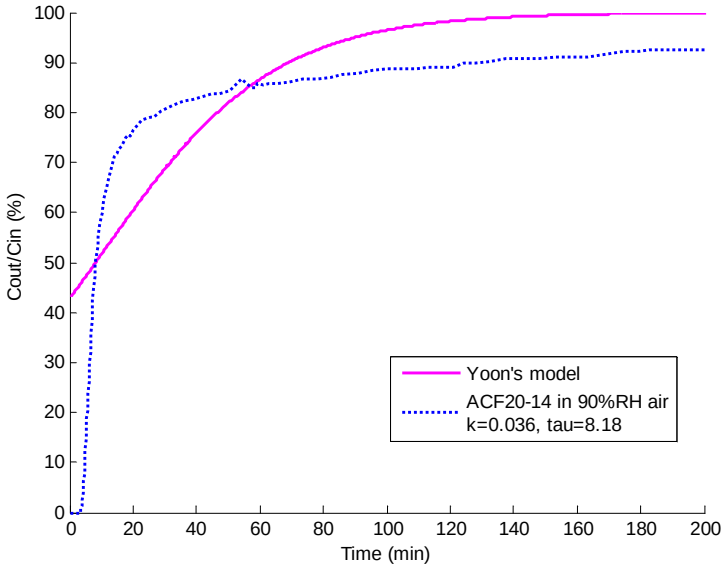

Figure 4.1 Prediction of breakthrough curve of ACF20 according to Yoon's model

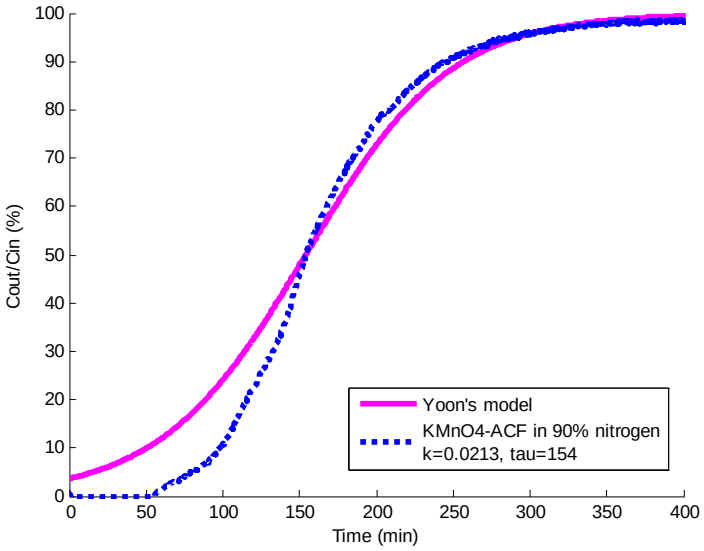

Figure 4.2 Prediction of breakthrough curve of $KMnO_4$/ACF15 according to Yoon's model

Most models available in the literature are for adsorption over bare adsorbents. In this research, mechanisms of removal of sulfur dioxide over potassium permanganate modified ACF15 ($KMnO_4$/ACF15) are studied. As discussed in Chapter 3, the removal efficiencies in different conditions are different and thus their mechanisms were regarded to be different. Four challenging gases are considered, SO_2+N_2, SO_2+Air+N_2, SO_2+H_2O and SO_2+H_2O+air. It should be noted that $KMnO_4$/ACF15 in this Chapter refers to the sample which was obtained after 43wt% $KMnO_4$ on ACF15 was subjected to water, since it had the highest adsorption capacity.

4.2 Mechanism one

In the case of combination of SO_2 and N_2 as the challenging gas, the adsorption test of $KMnO_4$/ACF15 was performed without the presence of either oxygen or water vapor.

4.2.1 Mechanism study

In order to understand the mechanism of SO_2 adsorption over $KMnO_4$/ACF15 without presence of oxygen and water in the carrier gas, the products of adsorption need to be identified. TGA and XRD techniques were used for this purpose (equipment and experimental conditions were included in Chapter 3). Using TGA, the decomposition of products on fiber surfaces was determined as shown in Figure 4.3. The TGA curve of $KMnO_4$/ACF15 after the adsorption test with the challenging gas of sulfur dioxide carried by nitrogen exhibits a similar shape with the one before the test. The $KMnO_4$/ACF15 after the adsorption test lost a small amount of weight at about 550^{o}C

and 770° C. The weight loss at 550° C may be attributed to the decomposition of MnO_2 whose decomposition temperature is 535° C. The fresh sample has a similar weight loss at 770° C with the spent sample. Therefore, MnO_2 is postulated to be the only product of the reaction between sulfur dioxide and $KMnO_4$. This result agrees with the theory that in the neutral and basic condition, sulfur dioxide is oxidized to MnO_2 or K_2MnO_4. Since K_2MnO_4 is not stable, the product must be MnO_2.

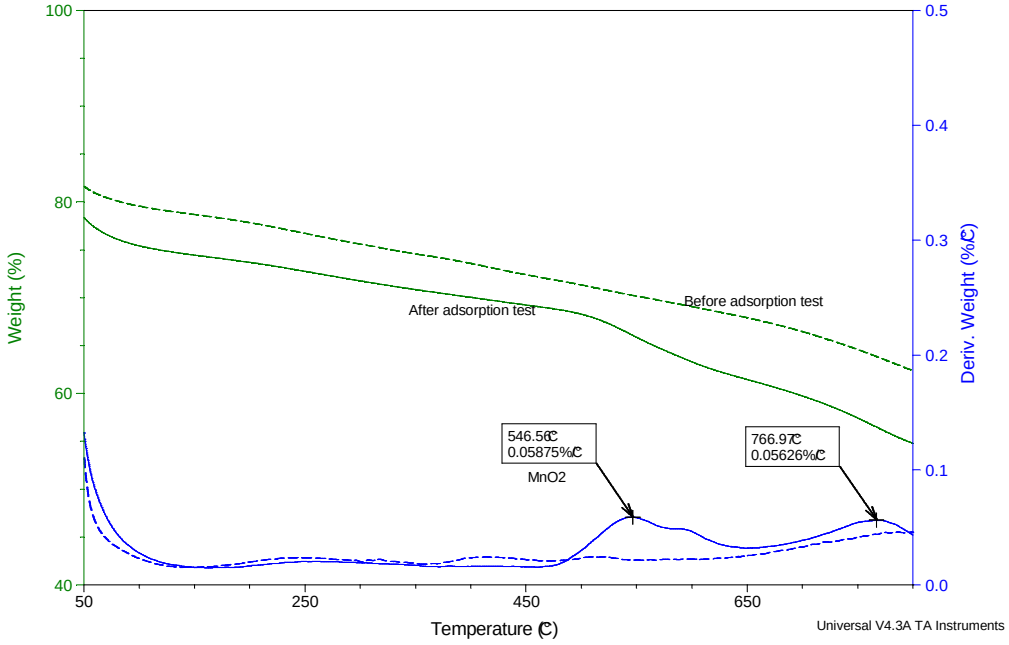

Figure 4.3 TGA curves of $KMnO_4$/ACF15 before and after adsorption tests in 50ppm SO_2 carried by nitrogen

In order to analyze the mechanism of adsorption of sulfur dioxide over $KMnO_4$/ACF15, the breakthrough curves of pure ACF15, $KMnO_4$/ACF15 without washing, $KMnO_4$/ACF15 and pure potassium permanganate are compared in Figure 4.4. Sulfur dioxide penetrated into the packed potassium permanganate (1gram) in the reactor immediately after starting the adsorption test without showing any adsorption

capacity. In comparison with $KMnO_4$, the removal of SO_2 over ACF15 is more efficient, which is indicated by the higher saturation capacity (90%) of ACF15 as shown in Table 4.1 and breakthrough curves in Figure 4.4. It can be included that the physical adsorption caused by pure activated carbon fibers is more than the chemical adsorption caused by pure potassium permanganate under this condition.

After $KMnO_4$ was distributed on activated carbon fiber surfaces, $KMnO_4$/ACF15 before washing shows a relatively higher SO_2 saturation capacity with less sharp breakthrough curve, which may be attributed to the increase of contact surface between sulfur dioxide and $KMnO_4$.

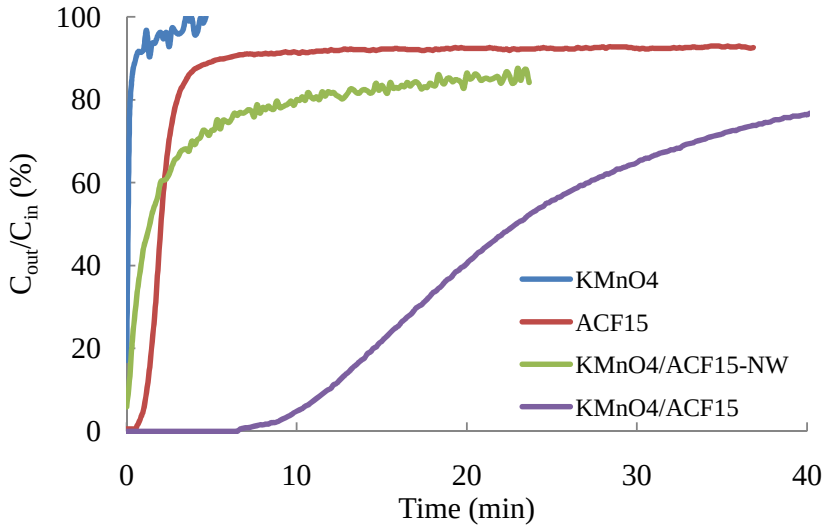

Figure 4.4 Breakthrough curves of ACF15, $KMnO_4$/ACF15 before exposed to water, $KMnO_4$/ACF15 and $KMnO_4$ in the challenging gas of SO_2+N_2 ($KMnO_4$ weight was 1 g and other samples were about 0.5 g.)

Table 4.1 90% Saturation capacities

Sample	ACF15	$KMnO_4$*	$KMnO_4$/ACF15 -NW	$KMnO_4$/ACF15
90% Saturation capacity (mg SO_2/g sample)	2.927	0.086	6.832	37.15

*Sample weight was 1 g for $KMnO_4$ while other samples were about 0.5 g, initial sulfur dioxide concentration was 50 ppm and face velocity of the gas stream was 33 cm/s. NW refers to not washing.

Although $KMnO_4$ does not show any SO_2 capacity on its own, its capacity was greatly improved when it was distributed over ACFs, which probably was due to the increased contact area between $KMnO_4$ and SO_2. 90% saturation capacity of ACF15 is lower than that of $KMnO_4$/ACF15 that was not exposed to water even though breakthrough period of ACF15 is longer. Compared to the other three samples in Figure 4.4, $KMnO_4$/ACF15 gave the longest breakthrough time and the highest saturation capacity. The great increase in SO_2 capacity was probably either caused by the increased available adsorption sites on ACF15 regenerated by exposure to water, or by further increase of contact surface between $KMnO_4$ and SO_2, providing more chances for reaction. It is postulated that some of SO_2 was physically adsorbed onto free adsorption sites on fibers and some others were transferred to other compounds by reactions. $KMnO_4$ may react with either gas phase sulfur dioxide or adsorbed sulfur dioxide. We assumed that adsorbed sulfur dioxide was dominant in reacting with potassium permanganate. Thus, the mechanism of SO_2 removal over $KMnO_4$/ACF15 can be described by equations (4.1)~(4.3).

$$SO_2 + F_v \Leftrightarrow SO_2 \cdot F_v \qquad (4.1)$$

$$2KMnO_4 \cdot F_v + 3SO_2 \cdot F_v \rightarrow 2MnO_2 \cdot F_v + K_2SO_4 \cdot F_v + 2SO_3 \cdot F_v \quad (4.2)$$

$$SO_3 \cdot F_v \Leftrightarrow SO_3 + F_v \quad (4.3)$$

F_v denotes free adsorption sites. $X \cdot F_v$ represents the substance that is attached or adsorbed on fibers. The resulting SO_3 may desorb from fiber surfaces offering more vacant sites for incoming sulfur dioxide.

As shown in Table 4.1, by loading 43% $KMnO_4$ on ACF15, the 90% saturation capacity of ACF15 is increased by 133%; after exposure to water, the 90% saturation capacity was increased by 444%. In other words, the improvement of SO_2 adsorption capacity caused by $KMnO_4$ distribution on ACF15 surfaces is less than that caused by increased vacant sites. Therefore, equation (4.1) is assumed to be the rate-determining step.

Sulfur dioxide adsorption rate can be expressed as follows.

$$\frac{dC_{[SO2 \cdot F_v]}}{dt} = k_a * C_{[SO2]} * C_{Fv} * (1-\theta) - k_d * C_{Fv} * \theta - k_2 * \theta * C_{Fv} \quad (4.4)$$

where, k_a is the adsorption rate constant and k_d is the desorption rate constant for equation (4.1), θ is the fraction of surface sites that are occupied by adsorbed molecules, k_2 is the reaction rate constant of equation (4.2), and C_{Fv} is the total active sites on fiber sample.

At the equilibrium, $\frac{d_{[SO2 \cdot F_v]}}{dt} = 0$

$$\theta = \frac{k_a * C_{SO2}}{k_a * C_{SO2} + k_d * + k_2} \quad (4.5)$$

Therefore,

$$\frac{dC_{SO2}}{dt} = -k_a * C_{SO2} * C_{Fv} * (1-\theta) + k_d * \theta * C_{Fv}$$
$$= k_a * C_{SO2} * C_{Fv} * (\frac{k_a * C_{SO2}}{k_a * C_{SO2} + k_d + k_2} + \frac{k_d}{k_a * C_{SO2} + k_d + k_2} - 1) \quad (4.6)$$

4.2.2 Model development

Some assumptions are made for model developments as follows.

1) The pressure drop of the fixed bed is very small; therefore isobaric conditions are assumed throughout the tests.
2) The system is isothermal throughout the fixed bed during the whole adsorption process.
3) The fluid velocity throughout the bed is constant.
4) The main gas stream and sulfur dioxide are considered as ideal gases.
5) Pore diffusion and surface diffusion occurs simultaneously.
6) The fixed bed is subjected to axial (longitudinal) dispersion, external mass transfer and intra-fiber diffusion of adsorbing species.

The model development is based on three governing equations:

1) mass balance of the adsorbing components in the bed.
2) mass balance of the component inside a single activated carbon fiber.
3) adsorption and reaction on the pore-walls of the fibers.

4.2.2.1 The mass balance of the adsorbing components in the packed bed

The mass balance of the adsorbing components in the packed bed is described as follows.

$$-D_Z \frac{\partial^2 C}{\partial z^2} + u\frac{\partial C}{\partial z} + \frac{\partial C}{\partial t} = -\frac{1}{f}\frac{\partial C_s}{\partial t} \tag{4.7}$$

where, D_z is the axial diffusivity, C the sulfur dioxide concentration in the main gas stream, z is the distance from the beginning of the packed ACFs, u is the face velocity of the main gas stream, $f = \frac{\varepsilon}{1-\varepsilon}$, ε is the porosity of the packed ACFs bed and C_s is the average SO_2 concentration within pores including gas phase and solid phase which is adsorbed onto fiber surfaces. $\frac{\partial C_s}{\partial t}$ is determined on the basis of the steady boundary film theory as follows [13].

$$\pi r_f^{\,2} L\frac{\partial C_s}{\partial t} = 2\pi r_f L k_g (C - C_S^F) \tag{4.8}$$

where, C_s^F is the solid phase SO_2 concentration on the fiber surface.

Therefore, $\frac{\partial C_s}{\partial t} = \frac{2}{r_f} k_g (C - C_s^F)$ (4.9)

Combining (4.7) and (4.9), the following equation for expression of the mass balance of adsorbates in packed ACFs is obtained:

$$-D_Z \frac{\partial^2 C}{\partial z^2} + u\frac{\partial C}{\partial z} + \frac{\partial C}{\partial t} = -\frac{1}{f}\frac{2}{r_f} k_g (C - C_s^F) \tag{4.10}$$

4.2.2.2 The mass balance within a single porous ACF In an individual ACF, the flux flowing into an infinitesimal unit volume with the thickness of dr is $-2\pi r L D_e \frac{\partial C_r}{\partial r}$, where r is the radius of the infinitesimal unit from the central line of the fiber. The flux flowing out of the unit is $-2\pi r L D_e \frac{\partial C_r}{\partial r} + \frac{\partial(-2\pi r L D_e \frac{\partial C_r}{\partial r})}{\partial r} dr$.

Therefore, the mass balance within a fiber is described as :

$$-2\pi rLD_e\frac{\partial C_r}{\partial r}-(-2\pi rLD_e\frac{\partial C_r}{\partial r}+\frac{\partial(-2\pi rLD_e\frac{\partial C_r}{\partial r})}{\partial r}dr)=\alpha 2\pi rLdr\frac{\partial C_r}{\partial t}+(1-\alpha)2\pi rLdr\frac{\partial C_{rs}}{\partial t} \quad (4.11)$$

The right side of equation (4.11) represents the sulfur dioxide accumulated in the unit both gas phase and solid phase on the fiber surface.

Equation (4.11) can be rearranged as:

$$D_e\frac{\partial}{\partial r}(r\frac{\partial C_r}{\partial r})=\alpha r\frac{\partial C_r}{\partial t}+(1-\alpha)r\frac{\partial C_{rs}}{\partial t} \quad (4.12)$$

where, D_e is the effective diffusivity, α is the intrafiber porosity, C_r is the gas phase sulfur dioxide concentration within the fiber, and C_{rs} is the solid phase sulfur dioxide concentration adsorbed on the fiber surface. To simplify the calculation process, C_r and C_{rs} are averaged within a single fiber, which reduces the second order partial differential equation (PDE) to first order PDE with only t direction. This approach has been used for adsorption on porous sorbents, such as Ca-sorbent, zeolites and activated carbon fibers, by other research groups as well [7, 9]. The average gas phase sulfur dioxide concentration within a fiber ($\overline{C}_r$) and the average of the solid phase adsorbed sulfur dioxide concentration on the fiber surface ($\overline{C}_{rs}$) are derived as follows.

Integrating the both side of equation (4.12) with respect to r at the rage of (0, r_f) where r_f is the fiber radius,

$$\int_0^{r_f} D_e\frac{\partial}{\partial r}(r\frac{\partial C_r}{\partial r})dr=\int_0^{r_f}\alpha\frac{\partial(rC_r)}{\partial t}dr+\int_0^{r_f}(1-\alpha)\frac{\partial(rC_{rs})}{\partial t}dr \quad (4.13)$$

Rearranging equation (4.13),

$$\frac{2}{r_f^{\,2}} D_e \left(r \frac{\partial C_r}{\partial r}\right)_{r=r_f} = \alpha \frac{\partial}{\partial t}\left(\int_0^{r_f} \frac{2}{r_f^{\,2}} r C_r dr\right) + (1-\alpha)\frac{\partial}{\partial t}\left(\int_0^{r_f} \frac{2}{r_f^{\,2}} r C_{rs} dr\right) \tag{4.14}$$

$\overline{C}_r$ and $\overline{C}_{rs}$ are expressed as:

$$\overline{C}_r = \frac{\int_0^{r_f} 2\pi r L C_r dr}{\pi r_f^{\,2} L} = \frac{2\int_0^{r_f} r C_r dr}{r_f^{\,2}} \tag{4.15}$$

$$\overline{C}_{rs} = \frac{\int_0^{r_f} 2\pi r L C_{rs} dr}{\pi r_f^{\,2} L} = \frac{2\int_0^{r_f} r C_{rs} dr}{r^{\,2}} \tag{4.16}$$

Substituting (4.15) and (4.16) into equation (4.14), the mass balance within a fiber is obtained:

$$\frac{2}{r_f} D_e \left(\frac{\partial C_r}{\partial r}\right)_{r=r_f} = \alpha \frac{\partial}{\partial t}(\overline{C}_r) + (1-\alpha)\frac{\partial}{\partial t}(\overline{C}_{rs}) \tag{4.17}$$

Equations (4.10) and (4.17) are coupled by continuity at the fiber surface [14]:

$$De\left(\frac{\partial C_r}{\partial r}\right)_{r_f} = k_g\left(C - C_s^F\right) \tag{4.18}$$

C_S^F is determined by equating mass flow across the external gas film to that on fiber surfaces and is dependent on variables $\overline{C}_r$ and C [15].

$$C_S^F = \frac{k_g C + 5\overline{C_r}\, D_e / d_f}{b} \tag{4.19}$$

where $b = k_g + \frac{5D_e}{d_f}$ and k_g is the mass transfer coefficient and d_f is the fiber diameter.

Similar to Equation (4.6),

$$\frac{\partial \overline{C}_{rs}}{\partial t} = \frac{\partial C_{SO2}}{\partial t} = k_a * \overline{C_r} * C_{Fv} * \left(\frac{k_a * \overline{C_r}}{k_a * \overline{C_r} + k_d + k_2} + \frac{k_d}{k_a * \overline{C_r} + k_d + k_2} - 1\right) \tag{4.20}$$

The governing equations (4.10), (4.17) and (4.20) describe the mass balance of adsorbates in the packed bed, the mass balance within and adsorption and reaction on fiber surface, respectively. They are the basis of the model development

for predicting the ACFs performance in the reactor under dynamic conditions. These equations are coupled partial differential equations with time (t), location of adsorbents (z) and radial direction (r) as independent variables. Initial and boundary conditions are

$t = 0; C = 0, \overline{C_r}=0$

$t > 0,\ z = 0, C = C_{in}$

$z = l; \frac{\partial \overline{C_r}}{\partial z} = 0$

By solving them, the time is related to the sulfur dioxide concentration on the main stream and breakthrough profile can be predicted. The dependency of sulfur dioxide removal efficiency on time and location can be estimated as well.

4.2.2.3 Derivation of equations for the modeling code with the finite difference methods The equations in the model are non-linear partial differential equations which usually require some numerical methods. A finite-difference method was used and the explicit central difference and backward difference themes were employed.

The mass balance between the main gas stream and the ACFs in the packed bed is given by Equation (4.10)

By substituting equation (4.20) into (4.10), the mass transfer in the packed bed is obtained:

$$\frac{\partial C}{\partial t} = D_Z \frac{\partial^2 C}{\partial z^2} - u\frac{\partial C}{\partial z} - \frac{1}{f}\frac{2}{r_f}k_g\left(C - \frac{k_g C}{b} - \frac{5\overline{C_r}D_e / d_f}{b}\right) \qquad (4.21)$$

For the prediction of the breakthrough curves, the fixed bed is divided into M equal sections along the reactor axial direction. The time direction is divided into N

segments. The corresponding step sizes for each direction are denoted as k and h, respectively.

According to the explicit finite difference themes [16],

$$\frac{\partial^2 C}{\partial z^2} = \frac{C(n-1,m+1) - 2C(n-1,m) + C(n-1,m-1)}{h^2} \tag{4.22}$$

$$\frac{\partial C}{\partial z} = \frac{C(n-1,m) - C(n-1,m-1)}{h} \tag{4.23}$$

$$\frac{\partial C}{\partial t} = \frac{C(n,m) - C(n-1,m)}{k} \tag{4.24}$$

where the indices m and n refer to the spatial location and time in the sample bed, respectively. Assuming that the sample bed is divided into m intervals with M+1 grip points with m=1 at Z=0 and m=M+1 at the exit of the gas which is equal to the bed depth.

Substituting equations (4.22), (4.23) and (4.24) into equation (4.12), the following discretised equations for diffusion within the sample bed can be obtained:

$$C(n,m) = p1 * C(n-1,m) + p2 * C(n-1,m+1) + p3 * C(n-1,m-1) + p4 * F(n-1,m)$$

$$2 \le m \le M \tag{4.25}$$

C(n,M+1)=C(n,M)

where, $p1 = 1 - 2 * \frac{D_z * k}{h^2} - \frac{u * k}{h} - \frac{2 * k_g * k}{f * r_f}(1 - \frac{k_g}{b})$

$$p2 = \frac{D_z * k}{h^2}$$

$$p3 = \frac{D_z * k}{h^2} + \frac{u * k}{h}$$

$$p4 = \frac{10 * k_g * D_e * k}{f * r_f * b * d_f}$$

The intrafiber mass balance is expressed by combining equations (4.17), (4.18) and (4.20).

$$\frac{\partial \overline{C_r}}{\partial t} = \frac{2 * k_g * C}{r_f * \alpha}(1 - \frac{k_g}{b}) - \frac{10 * k_g * D_e * \overline{C_r}}{\alpha * r_f * d_f * b} + \frac{\alpha - 1}{\alpha} * \frac{k_2 * k_a * \overline{C_r} * C_{Fv}}{k_a * \overline{C_r} + k_d + k_2}$$

$$\frac{\partial \overline{C}_r}{\partial t} = \frac{2 * k_g}{\alpha * r_f} * (1 - \frac{k_g}{b}) * C - \frac{10 * D_e * k_g}{\alpha * b * r_f * d_f} * \overline{C}_r + \frac{(1-\alpha) * k_a * k_d * \overline{C}_r}{\alpha * (k_d + k_a * \overline{C}_r)} + \frac{1-\alpha}{\alpha} * \frac{k_a{}^2}{k_a + k_d} * \overline{C}_r$$

$$- \frac{1-\alpha}{\alpha} * k_a * \overline{C}_r$$

(4.26)

$$\frac{\partial \overline{C_r}}{\partial t} = \frac{F(n,m) - F(n-1,m)}{k} \tag{4.27}$$

Therefore, the following discretized equations for the intrafiber diffusion can be obtained.

$$F(n,m) = F(n-1,m) - \frac{10 * k_g * D_e * k * F(n-1,m)}{\alpha * r_f * d_f * b} + \frac{\alpha - 1}{\alpha} * \frac{k_2 * k_a * k * F(n-1,m) * C_{Fv}}{k_a * F(n-1,m) + k_d + k_2}$$
$$+ \frac{2 * k_g * k * C(n-1,m)}{r_f * \alpha}(1 - \frac{k_g}{b})$$

(4.28)

$$F(n,m) = F(n-1,m) + p5 * C(n-1,m) - p6 * F(n-1,m) + p7 * \frac{F(n-1,m)}{k_a * F(n-1,m) + k_d + k_2}$$

where, $p5 = \frac{2 * k_g * k}{r_f * \alpha}(1 - \frac{k_g}{b})$

$$p6 = \frac{10 * kg * De * k}{\alpha * r_f * d_f * b}$$

$$p7 = \frac{\alpha - 1}{\alpha} * k_2 * k_a * C_{Fv} * k$$

Equations (4.25) and (4.28) are the two main equations for the modeling code.

4.2.2.4 Parameter evaluations

(1) Effective diffusivity (D_e)

The actual diffusion path of the adsorbate within a porous activated carbon fiber is not equal to the distance in the radial direction, but will be a quite tortuous path, which depends on the pore structure. Taking into account that the volume occupied by the solid is not available for diffusion, the value of diffusivity (D) is usually converted to the effective diffusivity (D_e) for the fact that diffusion only occurs in the pore space [14].

$$D_e = \frac{\alpha D}{\tau} \tag{4.29}$$

where, τ is the tortuosity factor of pores in porous fibers. Tortuosity is essentially a geometric factor which is independent of either temperature or the nature of the diffusion species. A tortuosity factor is defined as the ratio between the actual diffusion path length and the net distance in the direction of flux or the radial distance.

Diffusion in gas phase is determined by pore diameter and the mean free path of molecules. Knudsen diffusion is assumed if the mass free path is greater than ten pore diameters and collisions between pore walls and molecules are important. On the contrary, if pore diameter is ten times greater than the mean free path, then collisions between molecules dominate, which is called molecular diffusion. The two mechanisms for diffusion are both important when the mean free path and pore diameter are of the same order of magnitude. The diffusivity is calculated as follows:

$$D = \frac{1}{1/D_m + 1/D_k} \tag{4.30}$$

where D_m is molecular diffusivity and D_k is Kudsen diffusivity.

The mean free path $\lambda = \frac{1}{\sqrt{2} n \pi \sigma^2}$, where, n is the gas number density in molecules per volume, and σ is collision diameter in the experiments. Since over 95% air is present in the main gas stream, the mean free path is estimated to be 0.2 μm which is the mean free path for air at 1 atm and 300 K. Pore diameter of ACFs included in this research is in the range of 2.4~2.7 nm, which is 80 times smaller than the mean free path (0.2 μm). Therefore, Knudsen diffusion dominates.

$$D = D_k = 9.7 * 10^3 * r_f * (\frac{T}{M})^{0.5} \tag{4.31}$$

where, r_p (cm) is the pore radius, T is temperature (K), M is molecular weight of gas (g/mol), and D_k is Knudsen diffusivity (cm^2/s).

The molecular weight of gas depends on the experimental conditions, such as the relative humidity, carrier gas (N_2 or air) and sulfur dioxide concentration. At 20℃, the water vapor volume fraction in the air is 2.0851% at 90% relative humidity and 1.62% at 70% relative humidity.

The tortuosity factor of activated carbon fibers was reported to be smaller than that of granular activated carbon. Leyva-Romos et al., found the tortuosity factor of activated carbon fibers to be less than 2.7 [17]. τ is estimated to be 2.6 in his study.

The intrafiber porosity is calculated using the following relationship:

$$\alpha = 1 - \frac{V_{carbon} + V_{\mathrm{mod}\,ifier}}{V_{tpore} + V_{fiber} + V_{\mathrm{mod}\,ifier}} \tag{4.32}$$

where, V_{carbon} is the volume occupied by the solid ACF, $V_{modifier}$ is the volume of the modification agents (such as potassium hydroxide and potassium permanganate) and V_{tpore} is the total pore volume within the fiber. If the modifier load is β with respect to the total sample weight, the intrafiber porosity can be obtained as follows:

$$\alpha = 1 - \frac{\frac{1-\beta}{\rho_{carbon}} + \frac{\beta}{\rho_{modifier}}}{V_{tpore} + \frac{1-\beta}{\rho_{carbon}} + \frac{\beta}{\rho_{modifier}}} \tag{4.33}$$

where, ρ_{carbon} is the solid density of ACF, and $\rho_{moidifier}$ is the density of the modification agents. The solid density of ACF is reported to be 2.16 g/cm^3 which was determined by the helium displacement method using a Helium pycnometer [17]. Densities of potassium hydroxide and potassium permanganate are 2.044 and 2.703 g/cm^3, respectively.

A simple approximate estimation of tortuosity is given by Lua et al. [18] as follows.

$$\tau = \frac{(2-\alpha)^2}{\alpha}$$

For $KMnO_4$/ACF15, the calculated tortuosity is 2.6873 with the intrafiber porosity of 0.6641, which agrees with Leyva-Ramos' report [17].

(2) Axial diffusivity (D_z)

The axial diffusivity is given by [14]:

$$D_Z = D_m(20 + 0.5 S_c R_e)/\varepsilon \tag{4.34}$$

where, S_c is the Schmidt number and R_e is the Reynolds number, which are determined by the following equations:

$$S_c = \frac{\mu}{\rho_g D} \tag{4.35}$$

$$R_e = \frac{\rho_g \cdot u \cdot d_{re}}{\mu} \tag{4.36}$$

where, μ is the viscosity of the fluid, ρ_g is the density of the fluid and d_{re} is the diameter of the reactor. The viscosity of air at 18°C (291 K) is $18.27\times10^{-6}\ Pa\cdot s$. The fluid density can be obtained by $\frac{PM_f}{TR}$, where P is pressure (Pa), M_f is the average molecular weight of the fluid, T is the temperature and R is the ideal gas constant.

The molecular diffusivity for a binary gas mixture can be evaluated by the Chapman-Enskog equation [14]:

$$D_m = 0.0018583\times\frac{T^{3/2}(1/M_A + 1/M_B)^{1/2}}{P\sigma_{AB}\omega_{AB}} \tag{4.37}$$

where, M_A and M_B are molecular weights of A (sulfur dioxide) and B (air or nitrogen), respectively, D_m is molecular diffusivity (cm^2/s), P is pressure (atm), σ_{AB} and ε_{AB} are constants in the Lennard-Jones potential energy function for the pair AB. σ_{AB} is the collision diameter in angstrom and ε_{AB} is the maximum attractive energy between two molecules. ω_{AB} is the collision integral, a function of k_BT/ε_{AB}, where k_B is Boltzmann's constant.

If the carrier gas is air [19],

$$\sigma_{AB} = \frac{1}{2}(\sigma_A + \sigma_B) = \frac{1}{2}(\sigma_{SO2} + \sigma_{air}) = \frac{1}{2}(4.026 + 3.617) = 3.8215\ \text{Å}$$

where, σ_{SO2} is sulfur dioxide molecular diameter and σ_{air} is the average molecular diameter of air.

$$\frac{\varepsilon_{AB}}{k_B} = \sqrt{\frac{\varepsilon_A}{k_B}\cdot\frac{\varepsilon_B}{k_B}} = \sqrt{\frac{\varepsilon_{SO2}}{k_B}\cdot\frac{\varepsilon_{air}}{k_B}} = \sqrt{363\times97} = 187.65K$$

$\frac{k_B T}{\varepsilon_{AB}} = \frac{T}{\varepsilon_{AB}/k_B} = \frac{293}{187.65} = 1.56$ if the temperature is 20℃.

ω_{AB} is 1.183 if the carrier gas is air and temperature is 20℃.

The porosity of the packed ACF bed is calculated with the equation:

$$\varepsilon = 1 - \frac{V_{fiber}}{V_{bed}} = 1 - \frac{m_{fiber} / \rho_{fiber}}{\pi r_r^{\,2} L} \tag{4.38}$$

where m_{fiber} is the fiber mass used in the adsorption test, ρ_{fiber} is the fiber apparent density, r_r is the radius of the reactor and L is the packed bed depth.

(3) The mass transfer coefficient, k_g

For $3<R_e<10^4$, $S_h = 2 + 1.1 S_c^{\,1/3} R_e^{\,0.6} = \frac{k_g d_f}{D}$, where d_f is the fiber diameter [20].

Therefore, the mass transfer coefficient is determined by

$$k_g = \frac{S_h \cdot D}{d_f} = \frac{2 + 1.1 \times S_c^{\,1/3} R_e^{\,0.6}}{d_f} \cdot D \tag{4.39}$$

4.2.3 Prediction of breakthrough curve with the developed model

As discussed earlier, the adsorption of sulfur dioxide carried by nitrogen over $KMnO_4$/ACF15 consists of physical adsorption and chemical adsorption. The breakthrough curve is predicted using the model developed above and the resulting predicted curve is shown in Figure 4.5. The predicted breakthrough curve agrees with the experimental result reasonably well. The Matlab® code for model prediction is listed in Appendix 2.

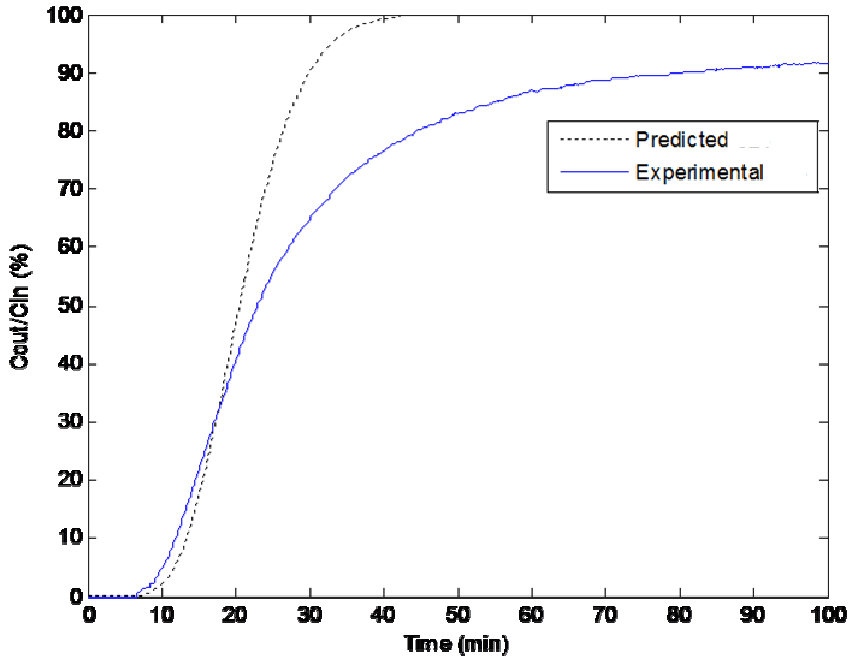

Figure 4.5 Breakthrough curve of $KMnO_4$/ACF15 exposed to 50ppm sulfur dioxide carried by nitrogen

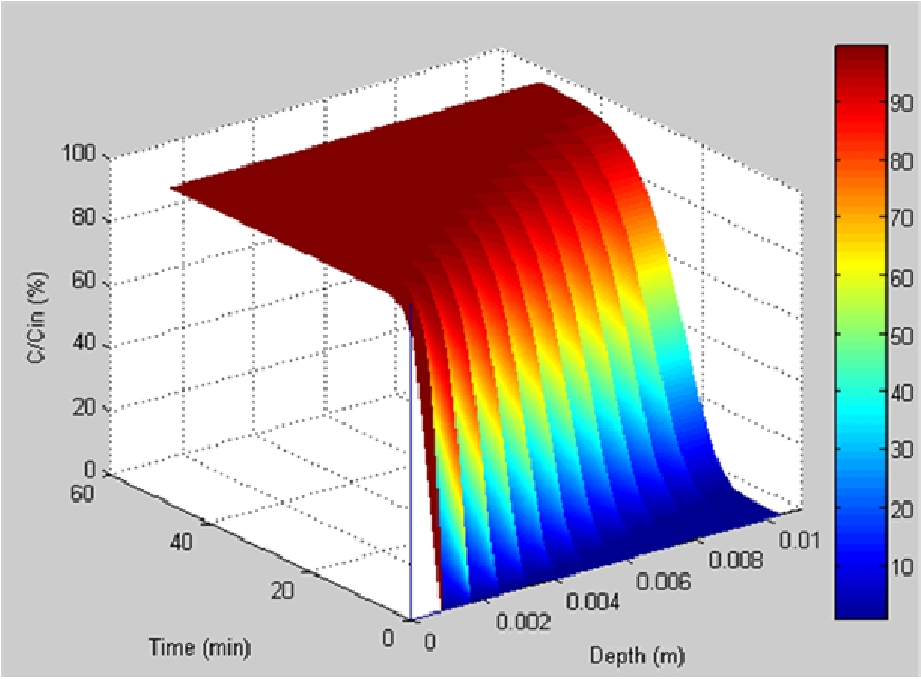

Figure 4.6 Prediction of sulfur dioxide removal efficiency with the variation of location and time

With the developed method, SO_2 removal efficiency profile within the reactor during the adsorption can be predicted as well, which is shown in Figure 4.6. In the packed fiber depth direction, fibers close to gas entrance got saturated faster than those closer to gas exit. The fibers in the reactor were saturated at the end of the test after a certain period of reaction time.

4.3 Mechanism Two

During the sulfur dioxide adsorption tests, if oxygen is included in the main gas stream to feed the reactor, sulfur dioxide removal mechanism is expected to be different from the first mechanism, in which oxygen was not included.

The breakthrough profiles of $KMnO_4$/ACF15 with and without the presence of oxygen under very low relative humidity (4~5%) are shown in Figure 4.7. For both air and nitrogen as the carrier gas, the breakthrough curves are consistent. It can be concluded that the presence of oxygen in the main gas stream does not affect sulfur dioxide breakthrough profiles and therefore does not contribute to improve the sulfur dioxide removal.

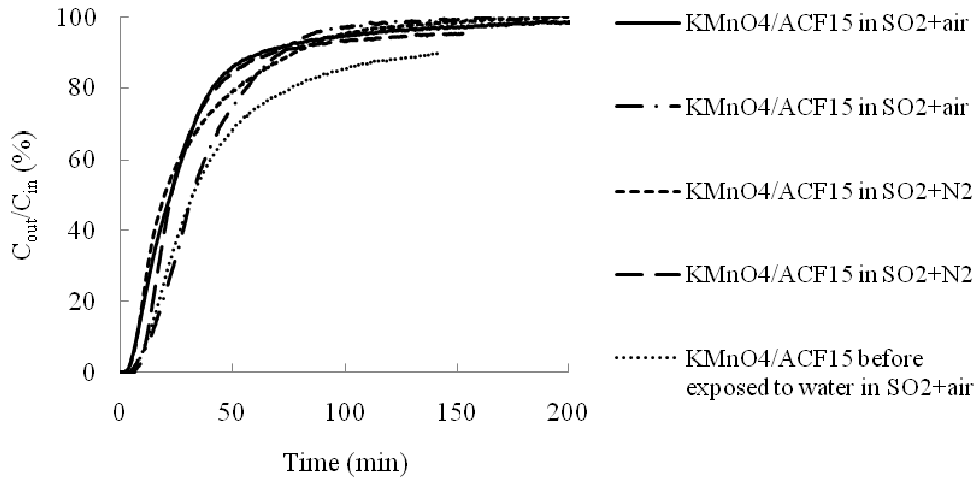

Figure 4.7 Breakthrough profiles of $KMnO_4$/ACF15 with exposure to sulfur dioxide challenge gas carried by air and nitrogen

$KMnO_4$/ACF15 samples before and after adsorption tests were subjected to TGA to observe the reaction products of sulfur dioxide removal. The dependence of sample weight on temperature in nitrogen atmosphere is shown in Figure 4.8. Before the adsorption test, potassium permanganate was distributed on fiber surfaces uniformly. Potassium permanganate may work as the activating agent and reactivate the activated carbon fibers, which causes continuous loss of weight with increased temperatures. When the adsorption test was completed, a part of potassium permanganate has been consumed to oxidize sulfur dioxide; the reaction products and unconsumed potassium permanganate would be present on fiber surfaces simultaneously.

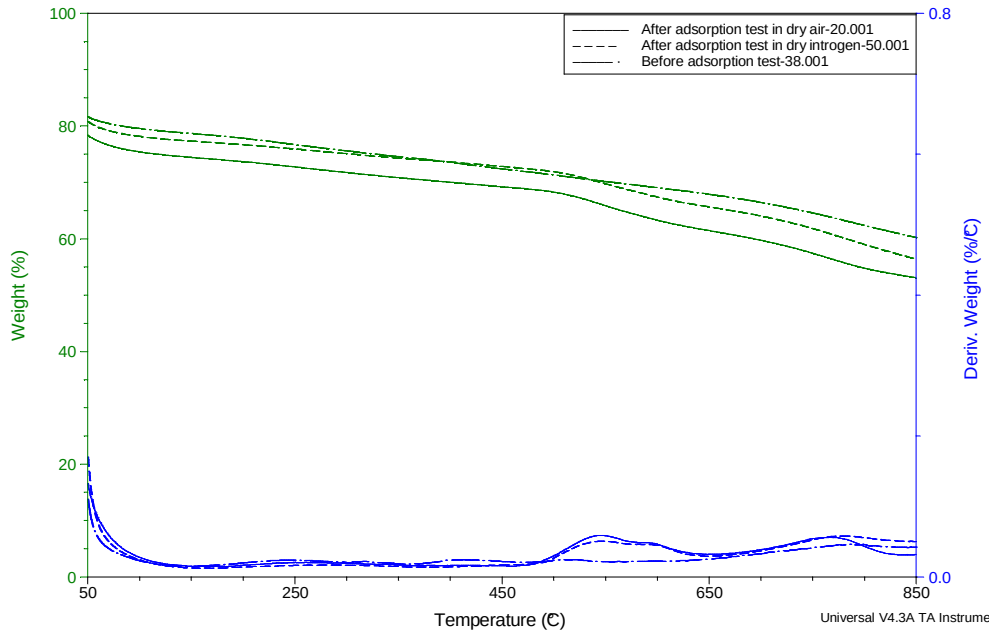

Figure 4.8 Weight change of $KMnO_4$/ACF15 before and after adsorption tests in the challenging gas of SO_2 carried by air with increasing temperatures

As shown in TGA curves, $KMnO_4$/ACF15s gave similar trend before and after SO_2 adsorption tests, which demonstrates that potassium permanganate is present after adsorption. However, after adsorbing SO_2, $KMnO_4$/ACF15 is showing one quick weight loss between 500 and 600^{o} C, indicating the presence of manganese dioxide. It is worthy to note that the TGA pattern of spent $KMnO_4$/ACF15 in dry air is similar to the one when dry nitrogen was the carrier gas in the main gas stream which was explained in Mechanism One. Theoretically, the oxygen in air will oxidize sulfur dioxide to sulfur trioxide (SO_3) especially with the help of a catalyst (activated carbon), and both of them will be adsorbed onto the catalyst. However, desorption of adsorbed sulfur trioxide is not detected by TGA probably due to low amount of SO_3 or gradual rather than sudden weight loss with the change of temperature.

The SO_2 adsorption over $KMnO_4$/ACF15 in dry air may include the diffusion of air to the fiber surfaces, diffusion of the gas into pores within fibers, physical adsorption of SO_2 onto vacant sites of fibers, oxidation of SO_2 by oxygen and formation of SO_3 which stays on the fiber surfaces and oxidation of SO_2 by the oxidant, potassium permanganate. This proposed process is expressed with the following equations:

$$SO_2 + F_v \Leftrightarrow SO_2 \cdot F_v \quad (4.1)$$

$$SO_2 \cdot F_v + \frac{1}{2}O_2 \rightarrow SO_3 \cdot F_v \quad (4.40)$$

$$2KMnO_4 \cdot F_v + 3SO_2 \cdot F_v \rightarrow 2MnO_2 \cdot F_v + K_2SO_4 \cdot F_v + 2SO_3 \cdot F_v \quad (4.2)$$

$$SO_3 \cdot F_v \Leftrightarrow SO_3 + F_v \quad (4.3)$$

$KMnO_4$ is excessive for the reaction (4.2), therefore its reaction rate constant is determined by the concentration of solid SO_2 on fiber surfaces.

Compared to the Mechanism One, one more reaction may occur involving oxygen in air. However, both TGA results and breakthrough curves did not show much change from the first mechanism. Oxygen was assumed not contributing too much in sulfur dioxide removal. Therefore, the model developed for the first mechanism can be used for this mechanism to predict the breakthrough properties of $KMnO_4$/ACF15 in the challenging gas of sulfur dioxide carried by air. The predicted breakthrough profile agrees with the experimental results reasonably well as shown in Figure 4.9.

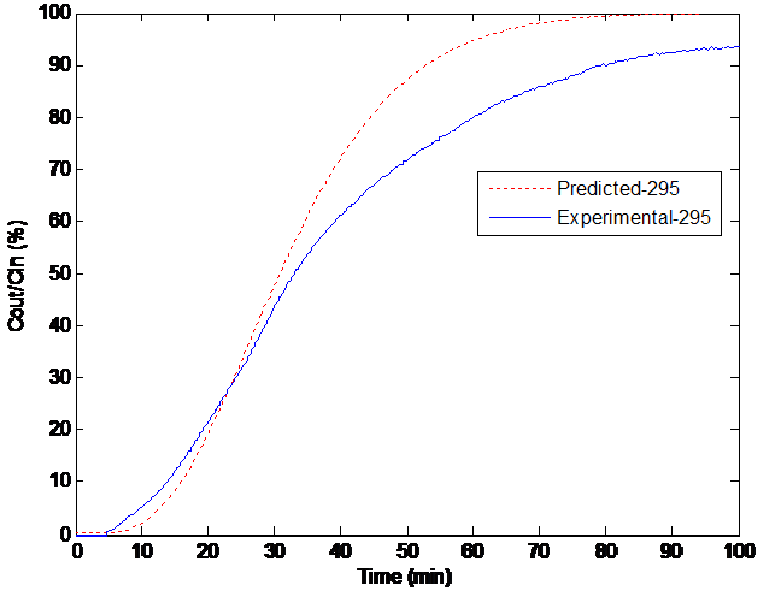

Figure 4.9 Prediction of breakthrough curve of $KMnO_4$/ACF15 with the challenging gas of SO_2+ air

The sulfur dioxide removal efficiency in the reactor dependens on both time and distance as discussed in Mechanism One. The developed model can predict the sulfur dioxide removal efficiency at different locations and reaction times as shown in Figure 4.10.

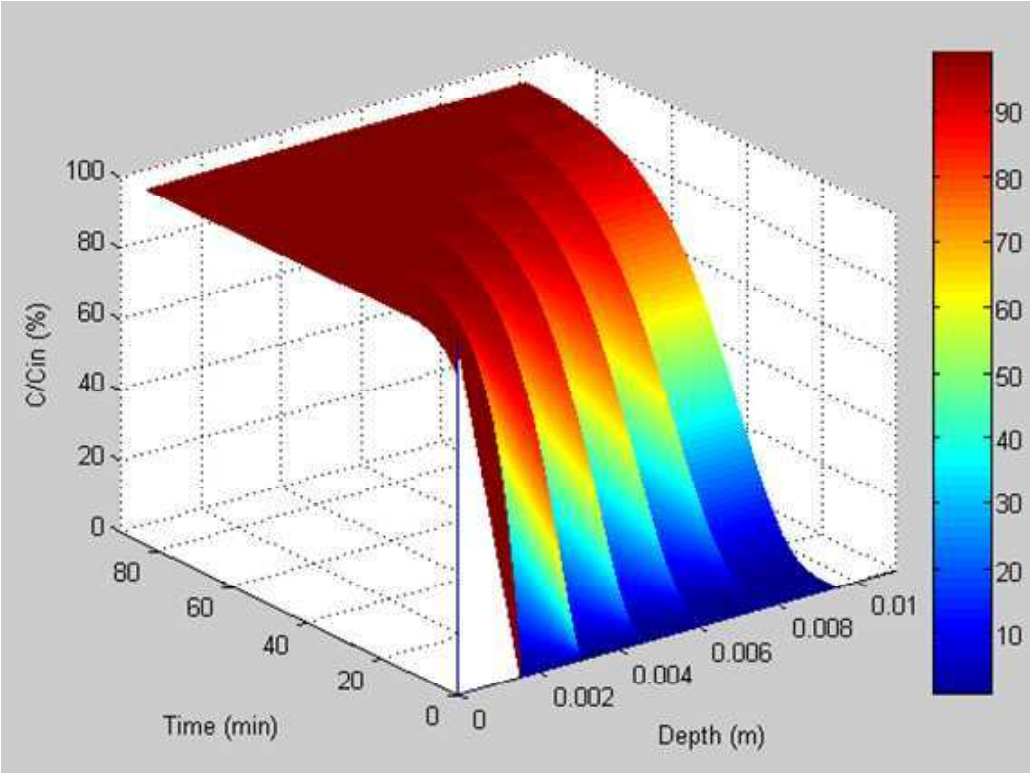

Figure 4.10 Prediction of sulfur dioxide removal efficiency at different locations and times with the challenging gas of SO_2+ air

4.4 Mechanism Three

4.4.1 Mechanism analysis

In Mechanism Three, the sulfur dioxide removal capability of $KMnO_4$/ACF15 was analyzed with the presence of water vapor and absence of oxygen in the main gas stream. There are two aspects of sulfur dioxide removal by $KMnO_4$/ACF15 in this case: direct adsorption of sulfur dioxide onto the vacant active sites on fiber surfaces and oxidation of sulfur dioxide by potassium permanganate. However, the presence of water will further convert the sulfur dioxide to sulfuric acid which is similar to the adsorption of sulfur dioxide with bare ACFs as discussed in Chapter 3. Like

Mechanisms One and Two, $KMnO_4$/ACF15 before and after adsorption tests were subjected to increasing temperatures and weight changes are illustrated in Figure 4.11. Before the SO_2 adsorption test, $KMnO_4$/ACF15 lost its weight gradually with increasing temperatures. However, after exposure to SO_2 carried by humidified nitrogen until the sample got saturated, $KMnO_4$/ACF15 showed a sudden weight loss at about 550ºC, corresponding to decomposition of MnO_2, which is similar to the previous two mechanisms. XRD results confirmed the product of MnO_2 which was discussed in Chapter 3.

The gradual weight loss of $KMnO_4$/ACF15 under increased temperatures probably is attributed to reactivation of activated carbon fibers, which may generate more pores or expand current pores to a bigger size. In order to confirm this proposal, $KMnO_4$/ACF15 and bare ACF15 were heated to 800°C and held at 800°C for 1 hour. The weight changes were recorded as shown in Figure 4.12. As the temperature was increased to 800°C from room temperature, both ACF15 and $KMnO_4$/ACF15 lost weight continuously while the latter exhibited quicker weight loss. At 800°C, the weight of ACFs remained constant but the weight of $KMnO_4$/ACF15 continued dropping which was due to the activation caused by the activating agent, potassium permanganate. Therefore, it is possible that more pores were formed or the existing pores were expanded.

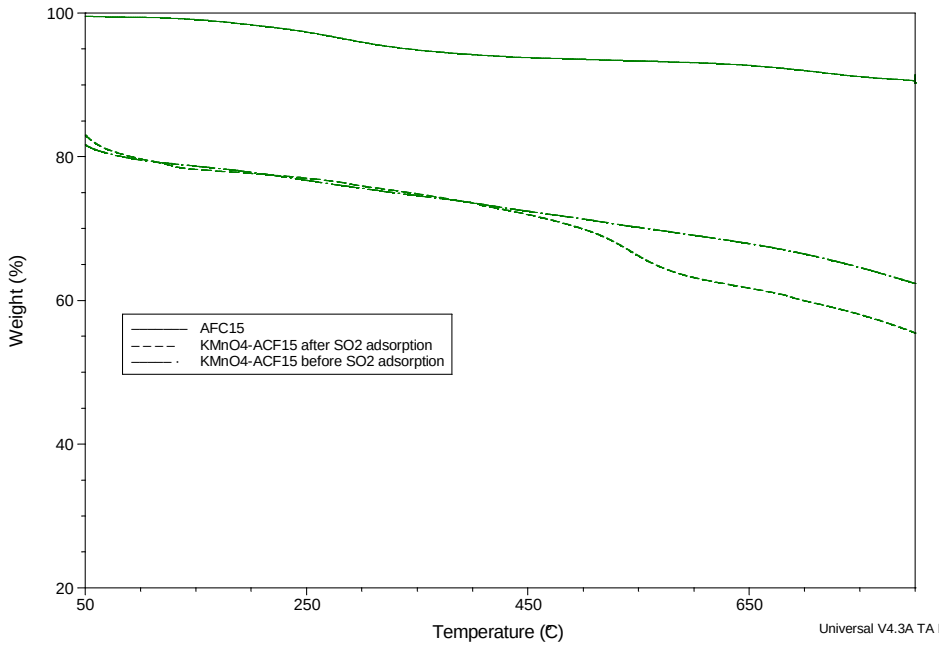

Figure 4.11 Weight changes of ACF15, $KMnO_4$/ACF15 before and after SO_2 adsorption test with the presence of water in the carrier gas with increasing temperatures.

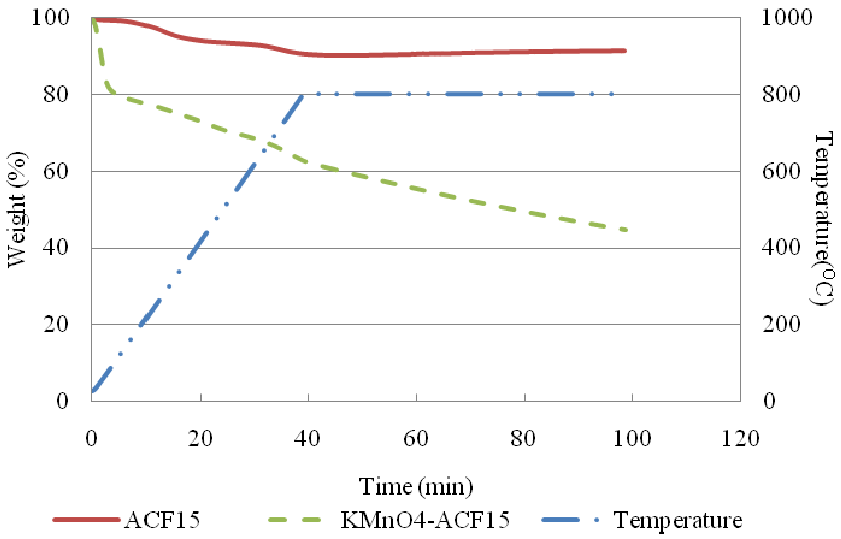

Figure 4.12 Effect of temperature on weight of ACF15 and $KMnO_4$/ACF15

Potassium permanganate may react with either gas phase or adsorbed SO_2. In order to determine the dominant process, pure solid potassium permanganate was packed in the reactor for sulfur dioxide removal under different conditions: dry air, humidified nitrogen and humidified air. In this case, there were no adsorption sites for sulfur dioxide to be adsorbed and only gas phase sulfur dioxide was available. 1g $KMnO_4$ rather than 0.5g was used because 0.5g $KMnO_4$ could not cover the cross section of the reactor and thus sulfur dioxide would escape from the reactor skipping $KMnO_4$ samples. The resulting breakthrough profiles are shown in Figure 4.13 Without the presence of water vapor, sulfur dioxide penetrated the potassium permanganate packed bed immediately as discussed in Mechanism One and thus it barely reacted with gas phase sulfur dioxide. When the water was included, sulfur dioxide removal efficiency of $KMnO_4$ was promoted greatly. Oxygen also contributed to the reaction as indicated by less steep breakthrough curve for $KMnO_4$ in the humidified air. It can be concluded that gas phase sulfur dioxide can react with potassium permanganate with the presence of water in the main gas stream. In order to investigate the contribution the activated carbon fibers, the breakthrough profile of $KMnO_4$/ACF15 is compared with that of the pure $KMnO_4$ with the same challenging gas: SO_2+H_2O+N_2, as shown in Figure 4.14. In spite of more $KMnO_4$ (1g) in the reactor, sulfur dioxide breakthrough occurs much quicker than that of $KMnO_4$/ACF15 (0.5g). The sulfur dioxide 4% breakthrough capacities in humidified nitrogen were calculated and are shown in Table 4.2. Breakthrough capacity of $KMnO_4$ was increased from 19.23 to 80.89 mgSO_2/g sample after distributing on fiber surfaces. Activated carbon fibers

greatly improved the sulfur dioxide removal ability due to the increase of contact surface between $KMnO_4$ and SO_2. Therefore, sulfur dioxide had more chance to be oxidized and reaction was accelerated, resulting in a longer breakthrough time as shown in Figure 4.15. Therefore, the dominant reaction can be assumed to happen between gas phase SO_2 and $KMnO_4$ on fiber surfaces.

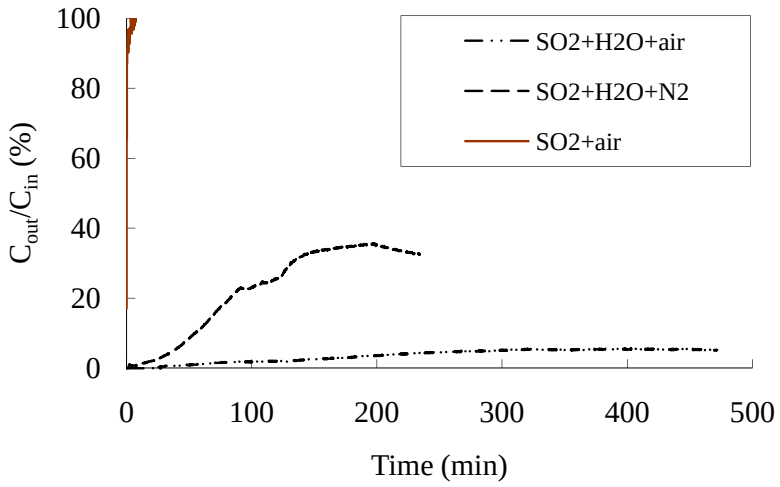

Figure 4.13 Breakthrough profiles of $KMnO_4$ with different challenging gases

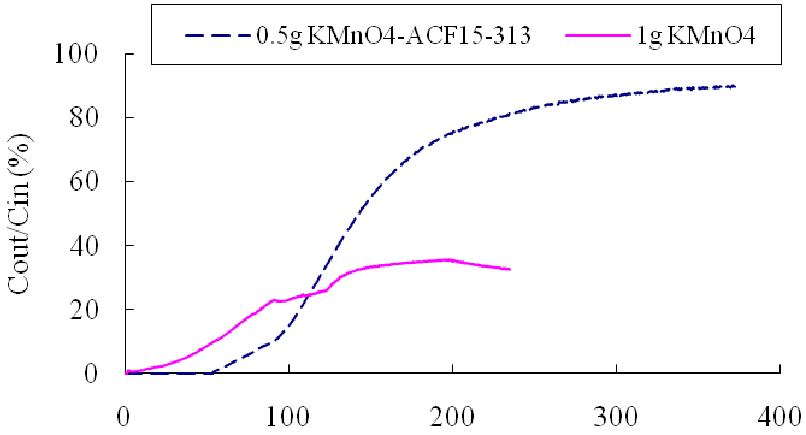

Figure 4.14 Breakthrough profiles of $KMnO_4$/ACF15 in comparison with $KMnO_4$ in the gas stream of sulfur dioxide and humidified nitrogen

Table 4.2 4% breakthrough capacities

Samples	4% breakthrough capacity (SO_2 mg/g sample)	4% breakthrough capacity (SO_2 mg/g $KMnO_4$)
$KMnO_4$/ACF15 in humidified nitrogen	80.8992	109
$KMnO_4$ in humidified nitrogen	19.23	-
$KMnO_4$ in humidified air	130.1975	-

Based on the analysis above, the sulfur dioxide removal process is described as follows.

$$SO_2 + F_v \Leftrightarrow SO_2 \cdot F_v \quad (4.1)$$

$$2KMnO_4 \cdot F_v + 3SO_2 \cdot F_v + 2H_2O \rightarrow 2MnO_2 \cdot F_v + K_2SO_4 \cdot F_v + 2H_2SO_4 \cdot F_v \quad (4.41)$$

$$2KMnO_4 \cdot F_v + 3SO_2 + 2H_2O \rightarrow 2MnO_2 \cdot F_v + K_2SO_4 \cdot F_v + 2H_2SO_4 \cdot F_v \quad (4.42)$$

$$H_2SO_4 \cdot F_v + H_2O \Leftrightarrow H_2SO_4 + F_v \quad (4.43)$$

4.4.2 Model development

Mochida et al., applied power law to describe the reaction and adsorption of sulfur dioxide over polyacrilonitrile-based ACFs and reasonable agreement between prediction and experiments was obtained [11]. The power-law model is used in this study to fit one apparent rate constant rather than using separate rate constants for each step. Equation (4.44) demonstrates this model:

$$-\frac{d_{SO2}}{dt} = k * C_{[KMnO4 \cdot Fv]}{}^{a} * C_{[SO2]}{}^{b} * C_{[H2O]}{}^{c} \quad (4.44)$$

If only 90% relative humidity is considered, water concentration is constant and

thus Equation (4.44) can be rewritten as:

$$-\frac{d_{SO2}}{dt} = k'*C_{[KMnO4\cdot Fv]}{}^{a} * C_{[SO2]}{}^{b} \tag{4.45}$$

where $k' = k * C_{[H2O]}{}^{c}$

Since the consumed $KMnO_4$ is $\frac{2}{3} * C_{[SO2]} * V$ and the unreacted $KMnO_4$ is ($totalamount - \frac{2}{3} * C_{[SO2]} * V$), which is rewritten as follows:

$$sampleweight * 0.4337/158 - \frac{2}{3} * C_{[SO2]} * V = 2.72 * 10^{-3} * sampleweight - 6.7 * 10^{-4} * C_{[SO2]} * FR * t$$

where, FR is the flow rate of gas stream (mL/min) and t is elapsed time in minute .

Therefore,

$$-\frac{dC_{[SO2]}}{dt} = k' C_{[KMnO4-Fv]}{}^{a} C_{[SO2]}{}^{b}$$
$$= k''*C_{[SO2]}{}^{b} * (2.72 * 10^{-3} * sampleweight - 6.7 * 10^{-4} * C_{[SO2]} * FR * t)^{a}$$

(4.46)

The mass balance of adsorbate diffusion within the packed bed and the mass balance of intrafiber diffusion within a fiber are expressed by equation (4.10) and (4.17), respectively. They are coupled by continuity at the fiber surface through equation (4.18) [14]:

Equations (4.10), (4.17) and (4.46) are combined to develop model for this mechanism. The gas phase sulfur dioxide concentration in the packed bed is related to time and location of the samples with the equation:

$$\frac{\partial C}{\partial t} = D_Z \frac{\partial^2 C}{\partial z^2} - u\frac{\partial C}{\partial z} - \frac{1}{f}\frac{2}{r_f} k_g (C - \frac{k_g C}{b} - \frac{5\overline{C_r} D_e / d_f}{b}) \tag{4.47}$$

The average sulfur dioxide concentration within fibers is related to time as follows.

$$\frac{\partial \overline{C_r}}{\partial t} = \frac{2 * k_g}{\alpha * r_f} * (1 - \frac{k_g}{b}) * C - \frac{10 * k_g * D_e}{\alpha * r_f * d_f * b} * \overline{C_r}$$
$$+ \frac{\alpha - 1}{\alpha} * k'' * \overline{C_r}^b * (2.72 * 10^{-3} * mass - 6.7 * 10^{-4} * \overline{C}_r * FR * t)^a$$

(4.48)

The same analysis process with Mechanism One is used to obtain the expressions for iteration in the computer program. Gas phase sulfur dioxide concentration in the main gas stream in the packed bed is:

$$C(n,m) = p1 * C(n-1,m) + p2 * C(n-1,m+1) + p3 * C(n-1,m-1) + p4 * F(n-1,m)$$

(4.49)

where, $p1 = 1 - 2 * \frac{D_z * k}{h^2} - \frac{u * k}{h} - \frac{2 * k_g * k}{f * r_f} (1 - \frac{k_g}{b})$

$$p2 = \frac{D_z * k}{h^2}$$

$$p3 = \frac{D_z * k}{h^2} + \frac{u * k}{h}$$

$$p4 = \frac{10 * k_g * D_e * k}{f * r_f * b * d_f}$$

The average sulfur dioxide concentration within fibers is:

$$F(n,m) = p5 * C(n-1,m) + p6 * F(n-1,m)$$
$$+ p7 * F(n-1,m)^b * (2.72 * 10^{-3} * mass - 6.7 * 10^{-4} * F(n-1,m) * FR * t)^a$$

(4.50)

where, $F(n,m)$ denotes $\overline{C_r}$ in equation (4.48)

$$p5 = \frac{k * 2 * k_g}{\alpha * r_f} * (1 - \frac{k_g}{b})$$

$$p6 = 1 - \frac{k * 10 * k_g * D_e}{\alpha * r_f * d_f * b}$$

$$p7 = \frac{\alpha - 1}{\alpha} * k * k''$$

The iterations of $C(n,m)$ and $F(n,m)$ are programmed with Matlab®; the code is attached in Appendix 3.

The breakthrough profile of $KMnO_4$/ACF15 in humidified nitrogen is predicted with this model, which agrees with the experimental results reasonably as shown in Figure 4.15. Furthermore, the dependence of sulfur dioxide removal efficiency in the packed bed on time and location is estimated based on the developed model as shown in Figure 4.15. At different depths of the bed, the time when the material got saturated was different. It took longer time for fibers which were close to the end of the bed to get saturated with sulfur dioxide. Eventually, the whole bed was saturated which is denoted with the color of dark red.

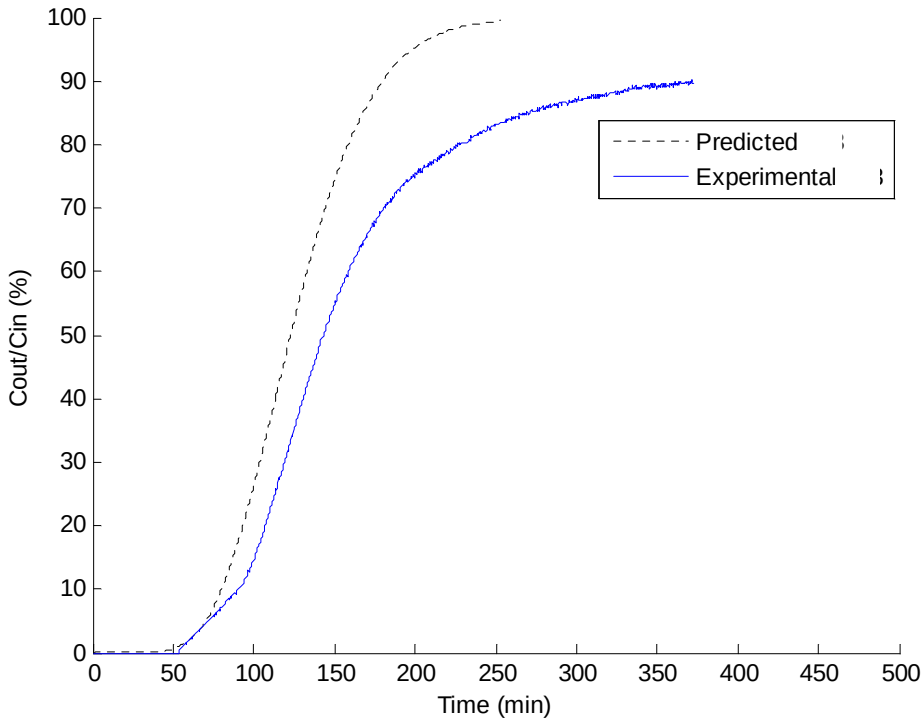

Figure 4.15 Prediction of breakthrough profile of $KMnO_4$/ACF15 in humidified nitrogen

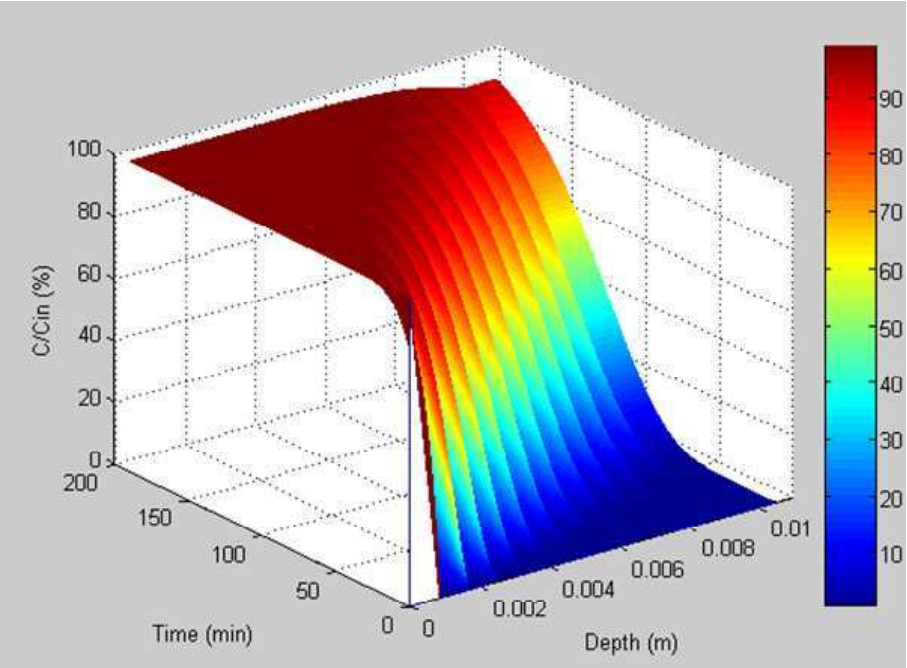

Figure 4.16 Dependence of sulfur dioxide removal efficiency on time and location in the packed bed with the carrier gas of humidified nitrogen

4.5 Mechanism Four

In this mechanism, the challenging gas for adsorption tests consists of sulfur dioxide, water and air. To investigate the influence of water on adsorption properties of $KMnO_4$/ACF15, breakthrough curves with the humidified nitrogen and humidified air as the carrier gases are shown in Figure 4.17. It took longer time to breakthrough if humidified air is the carrier gas although the period to get saturated was close for both carrier gases. The saturation capacity for the air carried challenging gas is higher than that carried by humidified nitrogen. In other words, oxygen in air promoted the sulfur dioxide removal when the water was present. In the co-presence of both water and oxygen, the sulfur dioxide removal mechanism can be divided into two components.

One is the oxidation of sulfur dioxide by potassium permanganate and the other one is the conversion of sulfur dioxide to sulfur trioxide by oxygen in air. These two oxidations occur simultaneously in the reactor.

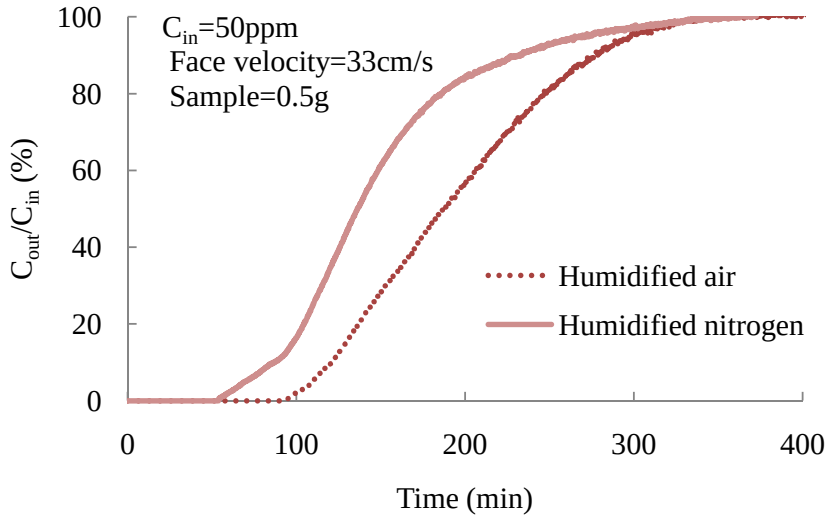

Figure 4.17 Breakthrough profiles of $KMnO_4$/ACF15 with exposure to sulfur dioxide carried by humidified nitrogen and humidified air

The oxidative removal of sulfur dioxide over $KMnO_4$/ACF15 was discussed in Chapter 3. The water hydrated the sulfur trioxide to sulfuric acid. The high relative humidity, 90%, provided additional water to elute the aqueous sulfuric acid from fiber surfaces and thus more vacant active sites were released for further reaction. This oxidation process was described with equations (4.1), (4.40), (4.49) and (4.13). Reaction products were identified using TGA and XRD. $KMnO_4$/ACF15 before and after adsorption tests were subjected to increasing temperatures on TGA and X-ray scanning, as explained in Chapter 3. The TGA analysis results are shown in Figure 4.18. After sulfur dioxide adsorption tests in both presence and absence of oxygen,

their TGA curves gave similar patterns and thus the oxidation products of sulfur dioxide by $KMnO_4$ are assumed to be the same. As analyzed in the section above, $KMnO_4$ might be reduced to MnO_2 and $MnSO_4$. Weight losses of spent $KMnO_4$/ACF15 at around 550ºC and 850ºC correspond to decomposition of MnO_2 and $MnSO_4$, respectively. The XRD analysis in Chapter 3 confirmed the existence of MnO_2 on the spent $KMnO_4$/ACF15 but $MnSO_4$ was not detected by XRD probably due to the small amount. Both adsorbed SO_2 and gas phase SO_2 can react with potassium permanganate as discussed in Mechanism Three. Sulfuric acid produced during the oxidation reactions caused by oxygen and potassium permanganate oxidation occupies vacant sites of activated carbon fibers. The additional water accelerates the elution of aqueous sulfuric acid from fibers and release active sites for further oxidation of coming sulfur dioxide. Therefore, the mechanism of SO_2 removal over $KMnO_4$/ACF15 with the presence of oxygen and water is described with following equations.

$$SO_2 + F_v \Leftrightarrow SO_2 \cdot F_v \quad (4.1)$$

$$SO_2 \cdot F_v + O_2 \Leftrightarrow SO_3 \cdot F_v \quad (4.40)$$

$$SO_3 \cdot F_v + H_2O \Leftrightarrow H_2SO_4 \cdot F_v \quad (4.49)$$

$$2KMnO_4 \cdot F_v + 5SO_2 \cdot F_v + 2H_2O \rightarrow 2MnSO_4 \cdot F_v + K_2SO_4 \cdot F_v + 2H_2SO_4 \cdot F_v \quad (4.41)$$

$$2KMnO_4 \cdot F_v + 5SO_2 + 2H_2O \rightarrow 2MnSO_4 \cdot F_v + K_2SO_4 \cdot F_v + 2H_2SO_4 \cdot F_v \quad (4.42)$$

$$2KMnO_4 \cdot F_v + 3SO_2 \cdot F_v + 2H_2O \rightarrow 2MnO_2 \cdot F_v + K_2SO_4 \cdot F_v + 2H_2SO_4 \cdot F_v \quad (4.50)$$

$$2KMnO_4 \cdot F_v + 3SO_2 + 2H_2O \rightarrow 2MnO_2 \cdot F_v + K_2SO_4 \cdot F_v + 2H_2SO_4 \cdot F_v \quad (4.51)$$

$$H_2SO_4 \cdot F_v + H_2O \Leftrightarrow H_2SO_4 + F_v \quad (4.43)$$

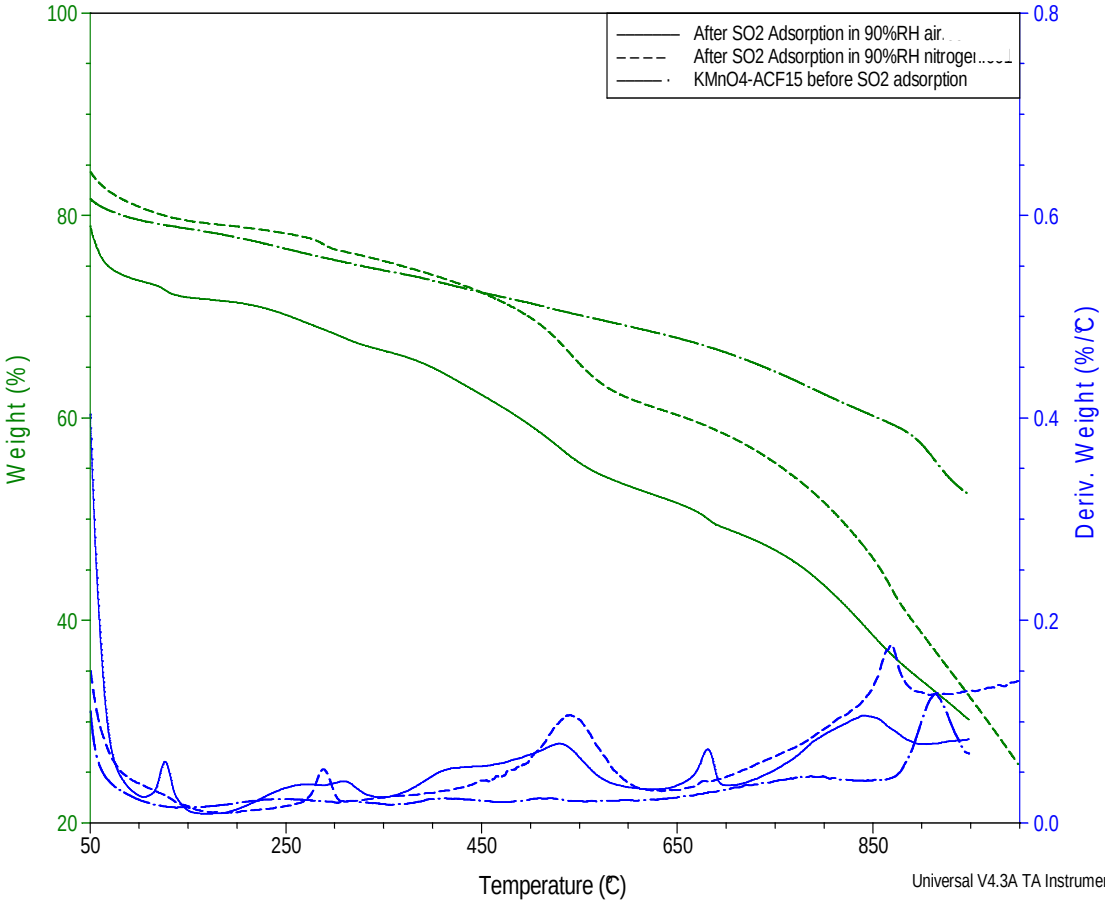

Figure 4.18 TGA curves of $KMnO_4$/ACF15 before and after exposure to the challenge gas of SO_2 +H_2O+air and SO_2 +H_2O+ N_2

Compared to the third mechanism, the presence of oxygen in this mechanism complicates the reaction involving oxidation by both oxygen and potassium permanganate. It is hard to determine the rate-determining step and dominant reaction. Therefore, power law is employed to describe the reaction kinetics as follows

$$-\frac{d_{SO2}}{dt} = k * m_{[KMnO4 \cdot Fv]}{}^{a} * C_{[SO2]}{}^{b} * C_{[H2O]}{}^{c} C_{[O2]}{}^{d} \qquad (4.52)$$

In the experiments, oxygen was carried in air and the variation of its concentration is small and thus neglected. Therefore, the oxygen concentration is assumed to be

constant. Moreover, the relative humidity remained at 90%. Thus, water and oxygen concentrations can be combined with the apparent rate constant, k. The following equation is obtained:

$$-\frac{d_{SO2}}{dt} = k'*m_{[KMnO4\cdot Fv]}{}^{a} * C_{[SO2]}{}^{b} \tag{4.53}$$

This reaction kinetic expression is the same with Mechanism Three. Therefore, the model developed for Mechanism Three is applicable for this mechanism. The predicted breakthrough profile using the developed model is shown in Figure 4.18 in comparison with the experimental results. The predicted sulfur dioxide removal efficiency agrees with the experimental results very well. Since the gas stream is flowing through the reactor continuously, the sulfur dioxide removal is in unsteady state. The dependence of sulfur dioxide removal efficiency on time is different at different locations of the packed bed in the reactor and is expressed with the curve shown in Figure 4.19.

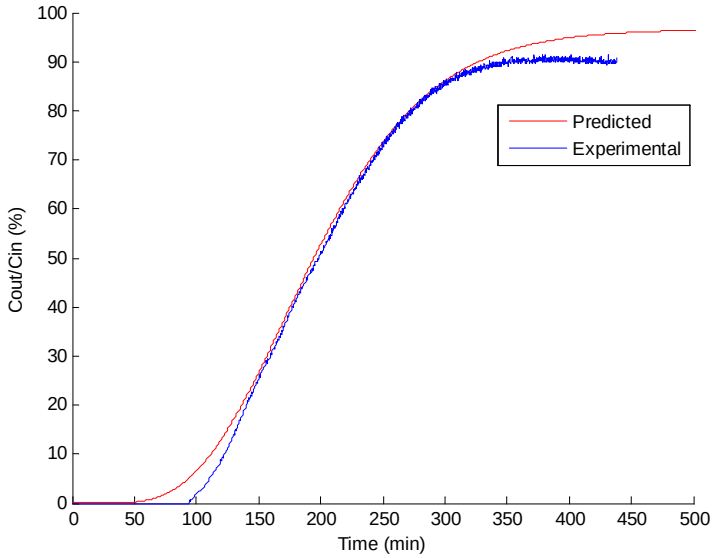

Figure 4.19 Prediction of breakthrough profile of $KMnO_4$/ACF15 exposed to SO_2 +H_2O+air

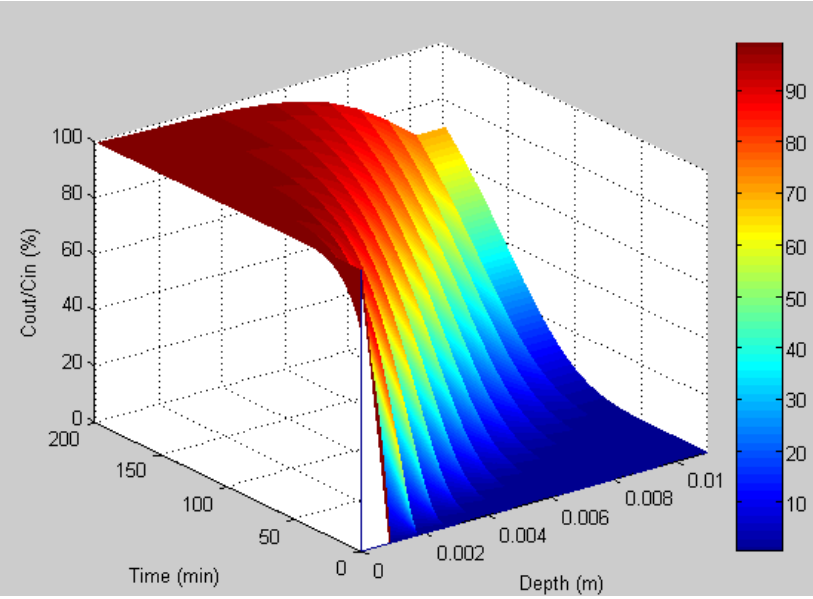

Figure 4.20 SO_2 removal efficiency of $KMnO_4$/ACF15 at various times and locations with the challenging gas of SO_2 +H_2O+air

4.6 Model system

Mechanisms One and Two can be predicted with the power law as well and therefore all four mechanisms are eligible for the power law model. The corresponding conpoents (a and b) and the apparent reaction rate constant (k') can be located in different ranges for each mechanism. These ranges and the best parameter set are listed in Table 4.3. The predicted breakthrough profiles of Mechanisms One and Two using the power-law model are compared with the experimental data and the models agree with the experimental data reasonably well as shown in Figuers 4.21 and 4.22.

Table 4.3 Parameters in the model system for mechanisms 1~4

	a	b	k’
Mechanism One	1.5~1.6	-0.4~-0.55	10~30
Best	1.55	-0.5	20
Mechanism Two	1.75~1.9	-0.55~-0.7	25~50
Best	1.8	-0.6	35
Mechanism Three	1.2~1.9	-0.01~-0.7	70~120
Best	1.5	-0.3	90
Mechanism Four	1.46~1.65	-0.1~-0.26	150~300
Best	1.55	-0.2	200

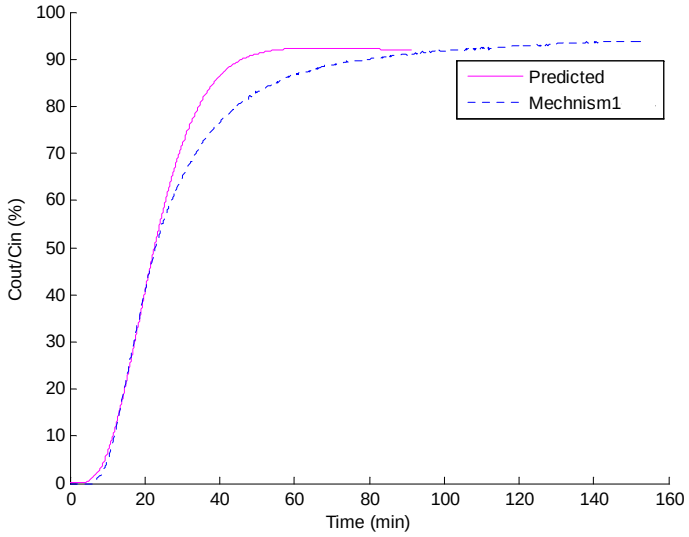

Figure 4.21 Prediction of breakthrough curve following Mechanism One with the power-law model system

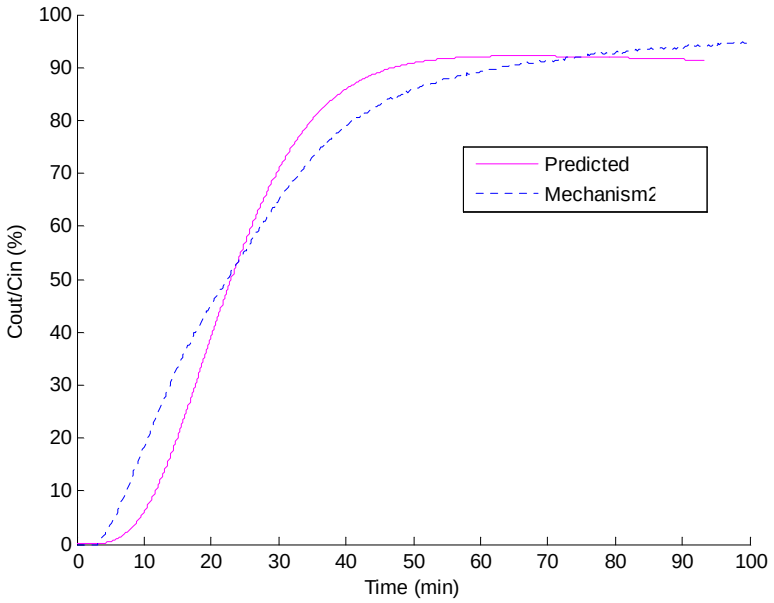

Figure 4.22 Prediction of breakthrough curve following Mechanism Two with the power-law model

References

1. Klotz, I. M., The adsorption wave, *Chemical Reviews*, 39 (2), 241-268, (1946).

2. Bohart, G. S. and Adams, E. Q., Some aspects of the behavior of charcoal with respect to chlorine, *Journal of American Chemical Society*, 42, 523-544, (1920).

3. Amundson, N. R., A note on the mathematics of adsorption in beds, *Journal of Physical and Colloid Chemistry*, 52 (7), 1153-1157, (1948).

4. Kennedy, D., Fuel cell cathode air filters: methodologies, Master Thesis. Auburn, Auburn University, (2007).

5. Yang, R. T., Gas separtion by adsorption processes, Imperial College Press, London, (1997).

6. Cheng, T. B., Jiang, Y., Zhang, Y. P. and Liu, S. Q., Prediction of breakthrough curves for adsorption on activated carbon fibers in a fixed bed, *Carbon*, 42 (15), 3081-3085, (2004).

7. Gupta, A., Gaur, V. and Verma, N., Breakthrough analysis for adsorption of sulfur-dioxide over zeolites, *Chemical Engineering and Processing*, 43 (1), 9-22, (2004).

8. Das, D., Gaur, V. and Verma, N., Removal of volatile organic compound by activated carbon fiber, *Carbon*, 42 (14), 2949-2962, (2004).

9. Gaur, V., Asthana, R. and Verma, N., Removal of SO_2 by activated carbon fibers in the presence of O_2 and H_2O, *Carbon*, 44 (1), 46-60, (2006).

10. Adapa, S., Gaur, V. and Verma, N., Catalytic oxidation of NO by activated carbon fiber (ACF), *Chemical Engineering Journal*, 116 (1), 25-37, (2006).

11. Mochida, I., Kuroda, K., Kawano, S., Matsumura, Y., Yoshikawa, M., Grulke, E. and Andrews, R., Kinetic study of the continuous removal of SOx using polyacrylonitrile-based activated carbon fibres 2: Kinetic model, *Fuel*, 76 (6), 537-541, (1997).

12. Yoon, Y. H. and Nelson, J. H., Application of Gas-Adsorption Kinetics 1. A Theoretical-Model for Respirator Cartridge Service Life, *American Industrial Hygiene Association Journal*, 45 (8), 509-516, (1984).

13. Coulson, J. M. and Richardson, J. F., Chemical Engineering, Pergamon Press,

(1990).

14. Yang, R. T., Gas Separation by Adsorption Processes, Imperial College Press, London, (1997).

15. Gupta, V. K. and Verma, N., Removal of volatile organic compounds by cryogenic condensation followed by adsorption, *Chemical Engineering Science*, 57 (14), 2679-2696, (2002).

16. Smith, G. D., Numerical Solution of Partial Differential Equations: Finite Difference Methods, Oxford University Press, New York, (1985).

17. Leyva-Ramos, R., Diaz-Flores, P. E., Leyva-Ramos, J. and Femat-Flores, R. A., Kinetic modeling of pentachlorophenol adsorption from aqueous solution on activated carbon fibers, *Carbon*, 45 (11), 2280-2289, (2007).

18. Lua, A. C. and Yang, T., Theoretical Analysis and Experimental Study on SO2 Adsorption onto Pistachio-nut-shell Activated Carbon, *Aiche Journal*, 55 (2), 423-433, (2009).

19. Bird, R. B., Stewart, W. E. and Lightfoot, E. N., Transport Phenomena, John Wiley & Sons, Inc., New York, (2002).

20. Coulson, J. M. and Richardson, J. F., Chemical Engineering, Butterworth Heinemann, Oxford, (2002).

Chapter 5 Conclusions and Recommendations

5.1 Conclusions

Proton exchange membrane fuel cell, one of the promising alternative energy sources, is prone to sulfur dioxide poisoning which decreased the cell performance of PEMFC and it cannot be recovered after purging fresh air. Therefore, there is a need to develop a filter media for sulfur dioxide removal, which is compatible with fuel cell systems. Since activated carbon fibers have been reported to have advantages in adsorption rate in comparison with granular activated carbons, they are chosen for sulfur dioxide removal in this research.

In order to manufacture activated carbon fibers, polyacrilontirile (PAN) was electrospun to nanofibers followed by chemical activation with potassium hydroxide. The resulting PAN-based activated carbon nanofibers have small micropore volume with an average pore diameter of 3 nm. However, the low productivity and fragility limit its application in filtration.

Commercialized rayon-based and novoloid-based ACFs were studied for sulfur dioxide removal. Micropores are dominant in ACFs with an average pore diameter of about 2.5 nm. The surface area was found to be related to the pore volume of ACFs but was not correlated with sulfur dioxide capacity. However, sulfur dioxide adsorption capacity was affected by the micropore percentages: the higher the ratio of micropores in

fibers, the higher the adsorption capacity. Different promoters were treated onto ACFs to enhance sulfur dioxide capacity, such as metal, alkali and oxidants. KOH, K_2CO_3 and $KClO_3$ can enhance the capability of fibers to purify sulfur dioxide in the gas stream. However, they are not suitable for the wet laying process through which modified ACF paper is manufactured due to the loss of sulfur dioxide capacity. On the other hand, $KMnO_4$ modified ACFs showed high sulfur dioxide breakthrough capacity and can withstand the wet-laying process without loss of sulfur dioxide capacity. The optimum weight ratio of potassium permanganate over ACFs is in the range of 43~45 wt% with the highest sulfur dioxide capacity. The co-presence of oxygen and water in the carrier gas is preferred for effective desulfurization.

Activated carbon fiber paper (K-ACFP) was manufactured from $KMnO_4$ modified ACF15 and the binder fiber, copolyester (CoPET). The strongest K-ACFP was obtained when the ratio of $KMnO_4$/ACF15 to CoPET is 7:3. Sulfur dioxide breakthrough capacity of the resulting K-ACFP was found to be similar to $KMnO_4$/ACF15 fiber before the wet laying process. Produced K-ACFP can be used as the filter media for fuel cell protection from sulfur dioxide.

Although the removal mechanisms of sulfur dioxide over bare activated carbon or activated carbon fibers have been studied to some extent, desulfurization mechanisms of modified ACFs were barely studied. Mechanisms of removal of SO_2 with $KMnO_4$/ACF under different conditions, namely SO_2+N_2, SO_2+air, $SO_2+H_2O+N_2$ and SO_2+H_2O+air, were analyzed in this research. It is found that $KMnO_4$ was reduced to MnO_2 while the sulfur dioxide was oxidized to SO_4^{2-}. Considering diffusions of adsorbates in the packed bed and within a single fiber and adsorption and reactions on fibers surface, models were

developed for the prediction of their breakthrough properties. The predicted breakthrough curves agree with experimental results reasonably well. With the developed models, the dependency of sulfur dioxide removal efficiency on the location in the packed bed and the elapsed time are estimated as well.

5.2 Recommendations

The $KMnO_4$/ACF filter media developed in the current research can be used to manufacture a filter device which can be installed in a fuel cell system. They can be packed in a tube, wrapped over a tube or packed in a cartridge to structure the filter devices. Different designs of filter devices may result in distinct efficiency to remove sulfur dioxide [1], which may need to be further studied to maximize their efficiency.

Since nitrogen oxide also degrades fuel cell systems, simultaneous removal of nitrogen oxide and sulfur dioxide would work more efficiently in protection of fuel cells. Effectively developed filter media on nitrogen oxide removal needs to be studied.

The ability to be regenerated is an important feature for adsorbents which will decrease the investment cost. $KMnO_4$/ACFs need to be studied in this respect.

The ratio of $KMnO_4$/ACF to CoPET in activated carbon fibers paper was set at 7:3 in term of the tensile strength. However, this ratio may not be the optimal for sulfur dioxide removal since both the dilution caused by binder fibers [2, 3] and the number of joint points, which would influence the available adsorption sites, may influence their sulfur dioxide capacity. Therefore, further research is needed to find out the optimal ratio of $KMnO_4$/ACF to CoPET for both strength and sulfur dioxide adsorption capacity.

References

1. Shmidt, J. L., Pimenov, A. V., Lieberman, A. I. and Cheh, H. Y., Kinetics of adsorption with granular, powdered, and fibrous activated carbon, *Separation Science and Technology*, 32 (13), 2105-2114, (1997).
2. Kalluri, R., Microfibrous entrapped catalysts and sorbents: microstructured heterogeneous contacting systmes with enhanced efficiency, Dissertation. Auburn, Auburn Unviersity, (2008).
3. Kalluri, R. R., Cahela, D. R. and Tatarchuk, B. J., Microfibrous entrapped small particle adsorbents for high efficiency heterogeneous contacting, *Separation and Purification Technology*, 62 (2), 304-316, (2008).

Appendix 1 Matlab® code for Yoon's model

```
Function modelyoon  % Code for Yoon's model
%For #14
k=0.036;  t=[0:0.1667:477.93];
a=length(t);  A=ones(1,a);  tau=8.18*ones(1,a);
c=A+exp(k*(tau-t));
P=(1./c)*100;  b=length(c);
hold on
plot(t,P,'m')

%For #293
k=0.0213;  t=[0:0.1667:477.93];
a=length(t);  tau=154*ones(1,a);
c=A+exp(k*(tau-t));
 P=(1./c)*100;
 b=length(c)
 hold on
plot(t,P,'m')
```

Appendix 2 Matlab® code for prediction of breakthrough curves for Mechanisms One and Two

```
Function model(s,dep,r,theta,ka,kd,k2,beta,mass,Q,RT)
h=dep/s;   %dep is the bed depth
k=r*h^2;
C=ones(theta*s,s+1);
F=ones(theta*s,s+1);
C(1,1:end)=0;
F(1,1:end)=0;
C(2:end,1)=2.079*10^(-3);
rf=5*10^(-6);
df=rf*2;
rre=0.7937*10^-2;   %the reactor radius (m)
u=0.04*Q/(60*pi*1.5875^2); %m/s, only for the reactor with diameter of 5/8".
rhoc=1.99;
rhom=2.703;
  Vtp=0.88;
alpha=1-((1-beta)/rhoc+beta/rhom)/(Vtp+(1-beta)/rhoc+beta/rhom);
rhof=alpha*1.23+(1-alpha)*(beta*rhom-(1-beta)*rhoc);
epsi=1-mass/(rhof*10^6)/(pi*rre^2*dep);
% To calculate Dz,
%To calculate D (cm^2/s)
rp=1.3*10^-9;  %pore radius (m)
```

```
T=293;
Mw=28.97;
D=9.7*10^3*rp*10^2*(T/Mw)^0.5;
%To calculate Re and Sc
R=8.314;
mu=18.27*10^-6; %the viscosity of fluid (air+SO2)(Pa.s).
rhoa=101325*Mw/(T*R);
Sc=mu/(rhoa*D*10^-4);   %D is in cm^2/s
 Re=rhoa*u*df/mu;

%To calculate Dm(molecular diffusivity, cm^2/s),
Ma=64;    Mb=Mw;  P=1;
delta=1/2*(4.026+3.617);
omega=(363*97)^0.5;
Dm=0.0018583*T^1.5*(1/Ma+1/Mb)^0.5/(P*delta*omega);

%To calculate Dz
Dz=Dm*10^-4*(20+0.5*Sc*Re)/epsi; %m^2/s

%kg (mass transfer coefficient)
Sh=2+1.1*Sc^(1/3)*Re^0.6; %For 3<Re<10^4
kg=Sh*D*10^-4/df;

%De
tau=2.6;  %tortuosity factor of ACFs
```

```
De=alpha*D*10^-4/tau;
f=epsi/(1-epsi);
b=kg+5*De/df;
p1=1-2*Dz*k/h^2-u*k/h-2*kg*k*(1-kg/b)/(f*rf);
p2=Dz*k/h^2;
p3=(Dz*k/h^2)+(u*k/h);
p4=10*kg*De*k/(f*rf*b*df);
p5=2*kg*k*(1-kg/b)/(alpha*rf);
p6=10*kg*De*k/(alpha*rf*df*b);
p7=((1-alpha)/alpha)*k2*ka*k;

for n=2:theta*s
   for m=2:s
   C(n,m)=p1*C(n-1,m)+p2*C(n-1,m+1)+p3*C(n-1,m-1)+p4*F(n-1,m);
  F(n,m)=F(n-1,m)-p6*F(n-1,m)+p7*F(n-1,m)/(ka*F(n-1,m)+kd+k2)+p5*C(n-1,m);
   end
   F(n,s+1)=F(n,s);
   C(n,s+1)=C(n,s);
end

B=C(1:end,s)/0.002079*100;
for n=1:theta*s
      if B(n)>0.5
         ST=n;
         B(n)
```

```
          break;
        else
          ST=-1;  % controller
       end
end

if ST==-1
   msgbox('No 0.5% breakthrough time is found.');
else

TS=RT/ST;
BT=TS*ST;
t=[0:TS:(theta*s-1)*TS];
d=[0:h:s*h];
plot(t,(C(1:end,s)/0.002079)*100,'k:')
axis([0,100,0,100])
xlabel('Time (min)');
ylabel('Cout/Cin (%)');
end
```

Appendix 3 Matlab® code for prediction of breakthrough curves for Mechanisms Three and Four

```
Function model(s,dep,r,theta,x,y,k1,beta,mass,Q,RT)

h=dep/s; % the z direction is divided into s parts and h is stepsize, L is the bed depth

k=r*h^2; % k is the stepsize in the time direction

C=ones(theta*s,s+1);

F=ones(theta*s,s+1);

C(1,1:end)=0;

F(1,1:end)=0;

C(2:end,1)=2.079*10^(-3); %50ppm initial sulfur dioxide

rf=5*10^(-6);

df=rf*2;

rre=0.7937*10^-2; %reactor radius (m)

u=0.04*Q/(60*pi*1.5875^2); %m/s, only for the reactor with diameter of 5/8".

rhoc=1.99;

rhom=2.703;

Vtp=0.88;

alpha=1-((1-beta)/rhoc+beta/rhom)/(Vtp+(1-beta)/rhoc+beta/rhom);

 rhof=alpha*1.23+(1-alpha)*(beta*rhom-(1-beta)*rhoc);

epsi=1-mass/(rhof*10^6)/(pi*rre^2*dep);


%To calculate D (cm^2/s)

    rp=1.3*10^-9; %pore radius (m)
```

```
 T=293;
    Mw=28.97;
D=9.7*10^3*rp*10^2*(T/Mw)^0.5;

%To calculate Re and Sc
R=8.314;
mu=18.27*10^-6;
rhoa=101325*Mw/(T*R);
    Sc=mu/(rhoa*D*10^-4);
    Re=rhoa*u*df/mu;
Ma=64;
Mb=Mw;
P=1;
delta=1/2*(4.026+3.617); %(SO2+air) angstrom
omega=(363*97)^0.5;  %First note P4
Dm=0.0018583*T^1.5*(1/Ma+1/Mb)^0.5/(P*delta*omega); %cm^2/s
%To calculate Dz
Dz=Dm*10^-4*(20+0.5*Sc*Re)/epsi; %m^2/s
 tau=2.6;
De=alpha*D*10^-4/tau;
f=epsi/(1-epsi);
b=kg+5*De/df;
p1=1-2*Dz*k/h^2-u*k/h-2*kg*k*(1-kg/b)/(f*rf);
p2=Dz*k/h^2;
p3=(Dz*k/h^2)+(u*k/h);
```

```
p4=10*kg*De*k/(f*rf*b*df);

p5=2*k*kg*(1-kg/b)/(alpha*rf);

p6=1-k*10*kg*De/(alpha*rf*df*b);

p7=(alpha-1)*k*k1/alpha; %k1 is the k'' in the equation

for n=2:theta*s

  for m=2:s

   C(n,m)=p1*C(n-1,m)+p2*C(n-1,m+1)+p3*C(n-1,m-1)+p4*F(n-1,m);

   F(n,m)=p5*C(n-1,m)+p6*F(n-1,m)+p7*F(n-1,m)^x*(2.73*10^(-3)*mass-6.7*10^(-
4)*F(n-1,m)*Q*k*n)^y;

   end

   F(n,s+1)=F(n,s);

   C(n,s+1)=C(n,s);

end

B=C(1:end,s)/0.002079*100;

for n=1:theta*s

      if B(n)>5

         ST=n

         B(n);

         break;

      else

         ST=-1;

      end

end

if ST==-1

   msgbox('no 5% breakthrough time is found.');
```

```
else
TS=RT/ST;
BT=TS*ST;
t=[0:TS:(theta*s-1)*TS];
d=[0:h:s*h];
figure,mesh(d,t,(C./0.002079*100))
axis([0,0.011,0,200,0,100])
xlabel('Depth (m)');
ylabel('Time (min)');
zlabel('Cout/Cin (%)');
colorbar;
end
```